Technical University of Munich
TUM School of Engineering and Design

Development of European manufacturing process for bare uranium-molybdenum monolithic foils

Kevin Georges BUDUCAN

Complete reprint of the dissertation approved by the TUM School of Engineering and Design of the Technical University of Munich for the award of the

Doktor der Ingenieurwissenschaften (Dr.-Ing.).

Chair: Prof. Dr. rer. nat. Sonja Berensmeier

Examiners:

1. Prof. Rafael Macián-Juan, Ph.D.
2. Prof. Dr. rer. nat. Winfried Petry

The dissertation was submitted to the Technical University of Munich on 10 August 2023 and accepted by the TUM School of Engineering and Design on 23 November 2023.

Technical University of Munich

Development of European manufacturing process for bare uranium-molybdenum monolithic foils

Dissertation

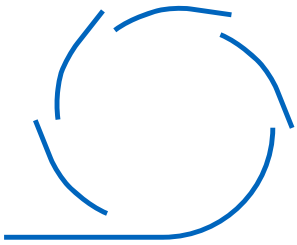

Department of
Mechanical Engineering

Forschungs-Neutronenquelle
Heinz Maier-Leibnitz (FRM II)

BUDUCAN Kevin
Prof. Dr. Rafael Macián-Juan
August 2023

With my signature below, I assert that the work in this thesis has been composed by myself independently and no source materials or aids other than those mentioned in the thesis have been used.

München, December 30, 2023 _____

Place, Date Signature

München, December 30, 2023 _____

Place, Date Signature

Abstract

Nuclear energy is one of the best controllable and safe electricity sources to reduce carbon emissions and maintain increased demand in a world in perpetual development. At the same time, the fission reaction induced is seen by scientists as a specific tool for many research domains, from medicine to material science. Thanks to its particular properties, the neutron represents a valuable tool for many scientific experiments, from material non-destructive tests to detailed sample analysis.

The Forschungs-Neutronenquelle Heinz Maier-Leibnitz (FRM II), a nuclear research reactor located in Garching, Germany, works closely with the international scientific community to use neutrons for fundamental research and scientific experiments. The actual uranium fuel used is an assembly of fuel plates composed of U_3Si_2 powder with enrichment in ^{235}U of 93 %. It is dispersed into an aluminium matrix and cladded with an aluminium alloy.

This enriched uranium, called HEU for Highly Enriched Uranium, is needed to perform a good neutron production rate to satisfy the demand of both scientists and industrial partners. Nevertheless, since 1970, a worldwide effort to reduce using of HEU has been performed by international partners by using uranium with an enrichment lower than 20 %, called LEU for Low Enriched Uranium. Since 2003 and the signature of an agreement for fuel conversion between the Federal Republic of Germany and the Bavarian State, the FRM II aims to convert its fuel from HEU to LEU by developing a new compact core. For this reason, a new nuclear fuel with an increased uranium density must be produced. The most promising candidate is a metallic monolithic uranium-molybdenum alloy fuel (U-Mo) with zirconium (Zr) coating and aluminium-based cladding.

Here we show the first European pilot line for depleted uranium-molybdenum bare foil manufacturing (DU-Mo), implemented in strong collaboration with fuel manufacturer Framatome-CERCA^{TM} in France, Romans-sur-Isère. This line involves various innovative manufacturing processes, including casting, laser welding, rolling, and laser cutting. The foil development is studied with the U-Mo ingot design for casting, choice of material for rolling, and different parameter optimization of manufacturing processes to control the foil production and to improve the global quality for future irradiation tests to convert the FRM II. Foil investigation with mechanical experiments, microstructure, and chemical composition studies, and then analysis of experimental results for each manufacturing step according to parameters used are performed to extract the best characteristics of this line for future industrialization.

This European manufacturing process gives an alternative solution to the US development and manufacturing of U-Mo bare foils, with a different approach in the manufacturing process and with different nuclear regulations. In addition, a European development of LEU fuel could push other European research reactors to use U-Mo as a candidate for their conversion. Finally, the work presented represents a first step for the industrial manufacturing of fuel plates based on monolithic U-Mo for converting the FRM II.

Kurzfassung

Die Kernenergie stellt heute eine der am besten kontrollierbaren und sicheren Stromquellen dar, um die Kohlenstoffemissionen zu reduzieren und die erhöhte Nachfrage in einer Welt in ständiger Entwicklung aufrechtzuerhalten. Gleichzeitig wird die Kernspaltung von Wissenschaftlern als gezieltes Werkzeug für viele Forschungsbereiche von der Medizin bis zur Materialwissenschaft angesehen. Durch seine speziellen Eigenschaften stellt das Neutron ein bedeutsames Element dar, für viele wissenschaftliche Experimente, wie materialzerstörungsfreie Tests bis hin zu detaillierten Probenanalysen.

Die Forschungs-Neutronenquelle Heinz Maier-Leibnitz (FRM II) arbeitet eng mit verschiedenen Wissenschaftlern zusammen, um Neutronen für Grundlagenforschung und wissenschaftliche Experimente zu nutzen. Der tatsächlich verwendete Uranbrennstoff ist eine Anordnung von Brennstoffplatten, in welchen U_3Si_2-Pulver mit einer ^{235}U-Anreicherung von 93 % in einer Aluminiummatrix dispergiert und mit einer Aluminiumlegierung ummantelt ist.

Dieses angereicherte Uran, genannt HEU für „High Enriched Uranium“, wird benötigt, um eine hohe Neutronenproduktionsrate zu generieren, die Nachfrage von Wissenschaftlern und industriellen Partnern bedient. Dennoch wird seit 1970, sowohl im militärischen als auch im zivilen Bereich, eine weltweite Anstrengung zur Reduzierung des Einsatzes von HEU von internationalen Partnern durchgeführt, indem Uran mit einer Anreicherung von weniger als 20 %, genannt LEU für „Low Enriched Uranium“, verwendet wird. Mit der Unterzeichnung einer Vereinbarung zur Umrüstung zwischen der Bundesrepublik Deutschland und dem Bayerischen Staat zielt der FRM II seit 2003 darauf ab, seinen Brennstoff von HEU auf LEU umzustellen, indem er einen neuen Reaktorkern entwickelt. Dies beinhaltet die Entwicklung eines neuen Kernbrennstoffs mit erhöhter Urandichte. Der vielversprechendste Kandidat für einen solchen Brennstoff ist eine metallische monolithische Uran-Molybdän-Legierung (U-Mo) mit Zirkoniumbeschichtung eingehüllt in einer Aluminiumlegierung.

Hier zeigen wir die erste europäische Pilotlinie zur Herstellung von Bare Foils aus abgereichertem Uran-Molybdän (DU-Mo), ungesetzt in enger Zusammenarbeit mit Framatome-CERCA^{TM} in Frankreich, Romans-sur-Isère. Diese beinhaltet eine Abfolge innovativer Herstellungsprozesse wie Laserschweißen, Walzen und Laserschneiden. Die Folienentwicklung wird hinsichtlich dem Design des Gussbarrens, der Auswahl des Materials für das Walzen und der Optimierung verschiedener Parameter des Herstellungsprozesse zur Optimierung der Folienproduktion und der Verbesserung der globalen Qualität für zukünftige Bestrahlungstests zur Umrüstung des FRM II untersucht. Die Folien werden mit mechanischen Verfahren, sowie mit Gefüge- und chemischen Zusammensetzungstudien untersucht. Anschließend werden die experimentellen Ergebnisse für jeden Fertigungsschritt anhand der verwendeten Parameter analysiert, um die besten Eigenschaften dieses Produktionswegs für eine zukünftige Industrialisierung zu ermitteln.

Dieses europäische Herstellungsverfahren bietet eine alternative Lösung zur US-amerikanischen Entwicklung und Herstellung von U-Mo Folien, welche einen anderen Ansatz in Bezug auf den Herstellungsprozess und unterschiedliche gesetzliche Regulierungen im Nuklearbereich hat. Darüber hinaus könnte eine europäische Entwicklung von LEU-Brennstoff andere europäische Forschungsreaktoren dazu bringen, U-Mo als Kandidaten für ihre Umrüstung zu verwenden.

Abstract

L'énergie nucléaire représente aujourd'hui l'une des sources d'électricité les plus performantes de par son aspect contrôlable et sûre pour réduire les émissions de carbone et maintenir une production constante d'énergie dans un monde en perpétuel développement. La réaction de fission induite est considérée par les scientifiques comme un performant outil d'analyse pour de nombreux domaines de recherche, allant de la médecine aux sciences des matériaux. De par ses caractéristiques, le neutron représente un élément clé pour effectuer de nombreuses expériences scientifiques, comme des essais non destructifs ou l'analyse détaillée d'échantillons.

Le réacteur de recherche Forschungs-Neutronenquelle Heinz Maier-Leibnitz (FRM II), située à Garching (Allemagne) travaille en étroite collaboration avec ses scientifiques pour utiliser ces neutrons à des fins de recherche fondamentale et d'expériences scientifiques. Le combustible actuellement utilisé est un assemblage de plaques composées d'U_3Si_2 enrichi ^{235}U à 93 %, dispersée dans une matrice d'aluminium et recouvert d'un gainage en aluminium.

Cet uranium enrichi, appelé UHE pour Uranium Hautement Enrichi, est nécessaire pour obtenir un flux de neutrons satisfaisant pour répondre à la demande des scientifiques et des groupes industriels. Néanmoins, depuis 1970, un effort mondial pour réduire l'utilisation de l'UHE est demandé, en utilisant l'uranium avec un enrichissement inférieur à 20 % appelé UFE pour Uranium Faiblement Enrichi. Depuis 2003 et la signature d'un accord de conversion avec la République fédérale d'Allemagne et l'état bavarois, le FRM II vise à convertir son réacteur d'UHE en UFE en fabriquant de nouveaux types d'éléments combustibles. Pour cette raison, un nouvel élément combustible avec une densité d'uranium accrue doit être développé. Le candidat le plus prometteur est un alliage métallique monolithique d'uranium et de molybdène (U-Mo) avec un revêtement en zirconium (Zr) et un gainage à base d'aluminium.

Nous présentons ici la première ligne pilote européenne pour la fabrication de feuilles en uranium-molybdène appauvri (DU-Mo), mise en oeuvre en étroite collaboration avec Framatome-CERCA^{TM} à Romans-sur-Isère (France). Cette ligne met en place une succession de processus de fabrication innovants tel que la fusion par arc et induction, le soudage laser, le laminage et la découpe laser. Le développement du processus est étudié avec la conception du lingot pour la coulée, le choix du matériau pour le laminage et différents paramètres d'optimisation des procédés pour optimiser la production de feuilles et améliorer leur qualité pour les futurs essais d'irradiation. L'étude des feuilles avec des essais mécaniques, des études de microstructure et de composition chimique, ainsi que l'analyse des résultats expérimentaux pour chaque étape de fabrication selon les paramètres utilisés sont effectués pour extraire les meilleures caractéristiques de cette ligne pour une future industrialisation.

Ce procédé de fabrication européen offre une solution alternative à la fabrication américaines de feuilles U-Mo, avec une approche différente en termes de procédé de fabrication et différentes réglementations liées au nucléaire. En outre, un développement européen du combustible UFE pourrait pousser d'autres centrales nucléaires de recherche européennes à utiliser l'U-Mo comme alliage pour leur conversion. Enfin, les travaux présentés dans cette thèse représentent une première étape pour la fabrication industrielle de plaques pour le FRM II, en particulier à utiliser et à améliorer pour la fabrication de feuilles UFE et la réalisation de plaques combustibles U-Mo pour la conversion du FRM II.

Contents

Part I

— Review of uranium-molybdenum bare foil manufacturing —

Chapter 1

The FRM II conversion: from HEU to LEU fuel

The FRM II aims to convert its fuel from a highly enriched fuel to a lower enriched by studying different material candidates for irradiation tests and reactor conversion with the help of international partners and consortiums. The FRM II must maintain the neutron rate production required for scientists and, at the same time, match with the required enrichment.

This section describes the background of this thesis work with the following parts:

- **Description of the FRM II**, with experimental devices available, purposes and a few characteristics about the research reactor and the nuclear fission;
- **Purposes of fuel conversion with different alloy candidates**, with fuel geometry used in the FRM II compact core and studies already performed for fuel manufacturing;
- **Overview on uranium-molybdenum fuel** as a promising candidate for the FRM II, with research realised and to do for the conversion and fuel manufacturing.

1.1 Forschungs-Neutronenquelle Heinz Maier-Leibnitz (FRM II)

The Forschungs-Neutronenquelle Heinz Maier-Leibnitz (FRM II), operated by the **T**echnical **U**niversity of **M**unich (TUM) in Garching, Germany, delivers high-intensity neutron beams for research, industry and medicine. The groundbreaking of the reactor dates back to August 1996, with the first neutrons in March 2004 and scientific use since April 2005 [1].

The predecessor of the FRM II, the FRM or "Atomic Egg", due to its shape, operated between 1957 to 2000 for more than 40 years, was at the origin of neutron research in Germany. Initially, the construction of the FRM, conducted by Technische Hochschule München on behalf of the Bavarian State Government and designed by Professor Heinz Maier Leibnitz, was first established to give Germany a performant research centre for neutrons. The FRM has been made possible under the "Atoms for Peace" program of the United Nations, led by the American government after the Second World War [2]. Both reactors are presented in Figure 1.1 in the heart of the TUM Garching campus.

Figure 1.1: *Research neutron source Heinz Maier-Leibnitz (Left: FRM II / Right: FRM)*

Nuclear research reactors are the leading producer of neutrons useful for medicine, material science and fundamental research. The specific properties of neutrons, i.e., their size with a diameter of 1.70×10^{-15} m, their thermal wavelength of 1.80 nm and the absence of an electric charge, allow many applications in industry. These include semiconductor doping or hydrogen detection in metallic alloys, structural analysis of biological molecules, investigations for energy applications, and material science such as crystallographic analysis [3].

As mentioned by Ballagny et al. [4], the main applications of research reactors involve:

- **irradiation technology** as the future Jules Horowitz reactor in France for nuclear energy experiments and isotope production;
- **neutron beams producer**, with **I**nstitut **L**aue-**L**angevin (ILL) in France or **H**igh **F**lux **I**sotope **R**eactor (HFIR) in the USA for fundamental research using neutron diffraction;
- **investigation of criticality aspects** as **B**elgium-**R**eactor **1** (BR-1) in Belgium for neutronic computation;
- **study of transient scenarios** and for **academic purposes**.

The fission reaction provides neutrons for each research reactor. The decomposition of a heavy nucleus from the impact of a neutron breaks it into light fission elements and neutrons, as shown in Figure 1.2.

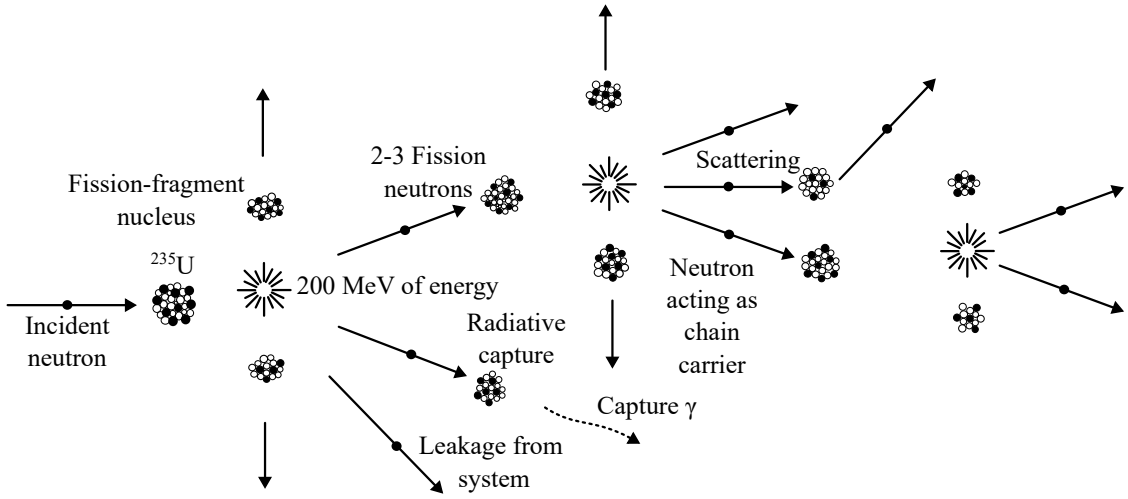

Figure 1.2: *Fission chain reaction of* ^{235}U *by incident neutron adapted from [5]*

This reaction provides enough energy used in controlled ways to obtain electricity. The energy provided by fission is not fully recoverable inside a nuclear plant. It is subdivided into prompt energy available directly after fission and the delayed one after the nucleus falls from an excited state to ground energy level with decay and energy released. Nuclear power plants use this energy for electricity production. On the other hand, research reactors use neutrons for other purposes. They deliver free neutrons thanks to fission reaction, as explained in Figure 1.2 for scientific research and industrial purposes.

Fast neutrons provided by fission reaction must be moderated, i.e., slowed down to maintain the chain reaction. At the same time, it transforms the neutron wavelength in a region of interest for fundamental science from 0.1 to 10 nm. One of the common moderators used is the D_2O deuterium oxide, also called heavy water.

Around the FRM II core, different moderators are set to tailor the neutron wavelength for particular applications, such as liquid D_2 (25 K), thermal D_2O (293 K), hot graphite (2273 K) and future solid D_2 for ultra-cold neutron source (5 K).

These neutrons are then extracted through horizontal beam tubes to feed different guides with appropriate neutrons and according to scientific instruments. Vertical beam tubes are inserted into the thermal D_2O moderator for irradiation. The architecture of neutron beam guides is depicted in Figure 1.3 with their specific experimental devices.

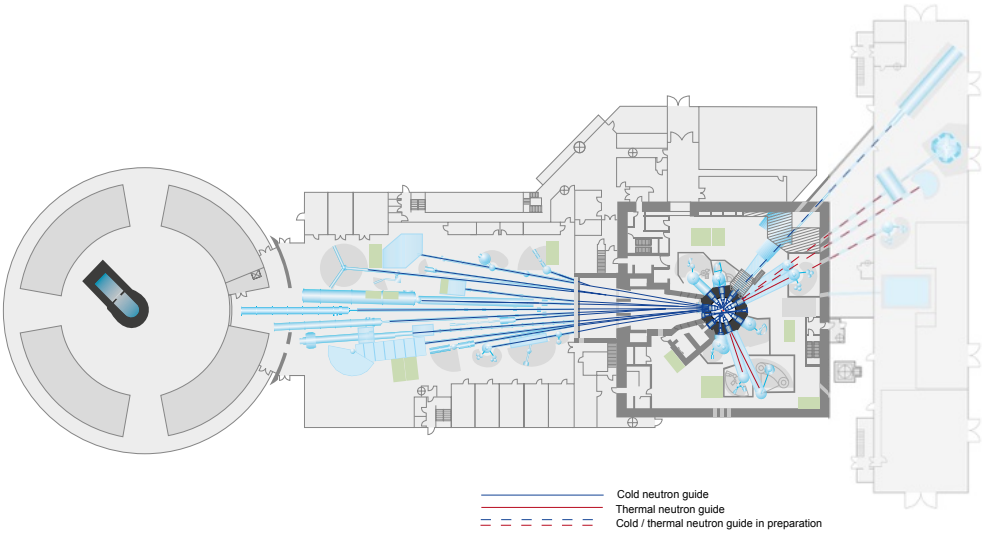

Figure 1.3: *Layout of the FRM II with corresponding experimental devices and neutron guide system (on the right on the grey square)*

For a nominal power of 20 MW, the maximal and undisturbed neutron flux available within the thermal D_2O moderator is 8.00×10^{14} neutrons/cm$^2 \cdot$s^{-1} [2]. Neutrons are provided from different sections of neutron guides to many experimental devices, such as POLI and Heidi for diffraction of hot neutrons, SPODI and StressSpec for diffraction with thermal neutrons and small angle scattering or SANS-1, KWS-1/2/3 with cold neutrons. They also serve high-resolution spectroscopy for instruments such as SPHERES (back-scattering), TOF-TOF (time of flight instrument) or J-NSE (neutron-spin echo).

To convert the FRM II core, i.e., replacing the current operating fuel, a group of researchers dedicated to high energy density fuel was created to design a new fuel element with a reduced enrichment. This group is supported by Bavarian institutions "**B**undes**m**inisterium für **B**ildung und **F**orschung" (BMBF) and "**B**ayerisches **St**aats**m**inisterium für **W**issenschaft und **K**unst" (StMWK).

1.2 The FRM II fuel characteristics for conversion

The compact core used for the FRM II consists of a single tube of 24 cm in diameter with a total length of 1.3 m and a total weight of 53 kg. The tube is filled with 113 involute-shaped fuel plates. Each fuel plate has an active zone of 70 cm in length, with a gap between each one of 2.3 mm, allowing light water to flow for fuel cooling. The light water is also the first moderator for fission neutrons. The current fuel element of the FRM II is a **H**ighly **E**nriched **U**ranium (HEU) fuel which contains in total 8.1 kg uranium in the form of U_3Si_2 powder embedded in an aluminium (Al) matrix. The U_3Si_2 meat has an enrichment of 93 % with a maximum density of 3.0 $gU \cdot cm^{-3}$. One fuel element can operate the neutron source for 60 days at a power of 20 MW. Four cycles of 60 days each are ensured for one year, with maintenance work between each to keep the same performance of neutron beam, safety, and security aspects. Figure 1.4 presents a detailed view of the FRM II compact core.

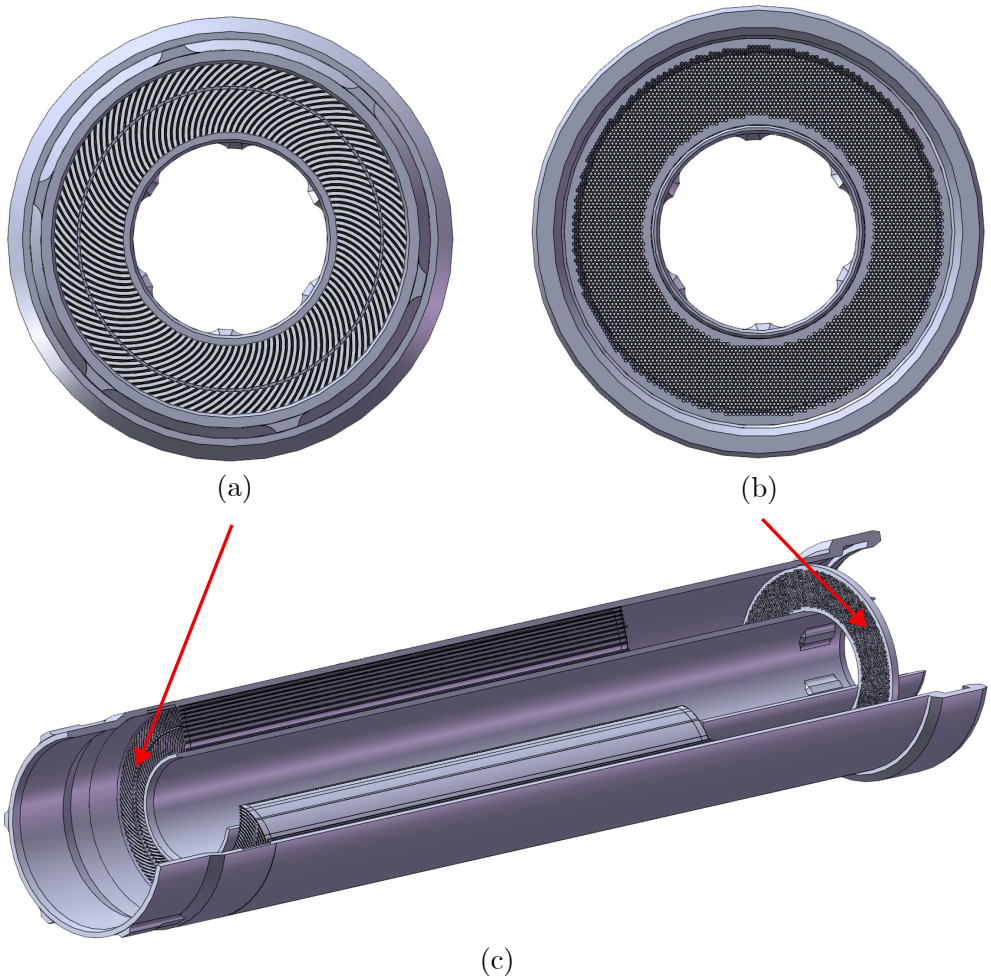

Figure 1.4: *Cutting view of the FRM II compact core (a: below / b: above / c: assembly)*

The typical composition of the future FRM II fuel plate is the following:

- **Fuel meat** - This part contains all elements needed to ensure fission reaction during the fuel cycle. This layer is made of fissile isotopes, usually uranium with isotopes ^{235}U, and alloying elements to guarantee controlled swelling during in-pile irradiation. This part is subject to different manufacturing steps with various shapes and geometry. Mainly two types are available: the monolithic and the dispersed one, as shown in Figure 1.5;
- **Fuel coating** - The coating is a critical part of the fuel. Fuel meat and cladding interact due to the irradiation process. Neutrons and emissions from the fission reaction interact with the cladding material and may lead to uncontrolled swelling and premature cracks during the fuel plate operation. This coating has the property of a reaction barrier between the meat and the cladding, reducing this interaction to extend the life period of the fuel and avoid incidents such as cracks or plate delamination;
- **Fuel cladding** - This layer can also be named framing. It represents the last barrier between fissile meat and the cooling water in the reactor. The material used needs to exhibit good properties for the neutron to let them pass during the fission reaction and have great resistance against oxidation. It also needs good thermal properties to ensure fuel cooling during its use. Usually, the cladding is realised with aluminium alloys thanks to its good properties for neutrons with a low absorption cross-section as optimal mechanical and thermal properties for research reactor operation [6]. The term cross-section refers to an atomistic material property to allow different types of interaction between neutrons and atoms. According to the interaction, it could be considered as the probability for this interaction to happen if the neutron enters a delimited area around the atom, which is the cross-section [7].

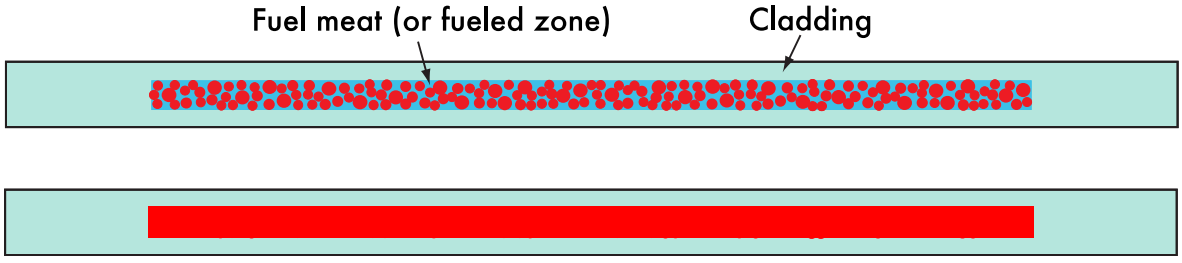

Figure 1.5: *Fuel plate composition with dispersed (top) and monolithic (bottom) meat [6]*

The FRM II fuel plate represents a challenge in manufacturing and uranium enrichment, as the fuel plate geometry is complex to set up for final fuel assembly and to answer neutron demand with another fuel meat, which involves different irradiation results. Different groups and consortiums studied different uranium alloys, and uranium-molybdenum (U-Mo) was selected as the most promising candidate.

1.3 U-Mo monolithic fuel plate: researches and interests

In an international context of non-proliferation for nuclear material and to improve the quality of neutron sources, new fuels are studied to reduce HEU use in research reactors while keeping both fission and power density required. As exposed in previous parts, research reactors mainly use HEU fuel for its high density of ^{235}U, which delivers high neutrons flux. Conversion from HEU to LEU involves reducing enrichment from 93 % to 20 % as the maximal value. The LEU, for **L**ow **E**nriched **U**ranium, is defined as uranium material enriched with less than 20 % of ^{235}U. This lack of enrichment has to be compensated by increasing fissile uranium density in the fuel meat.

In a worldwide movement initiated by the American government with the **R**educed **E**nrichment for **R**esearch and **T**est **R**eactors (RERTR) program in 1978 and close actors as **N**ational **N**uclear **S**ecurity **A**dministration (NNSA), the **US D**epartment **O**f **E**nergy (USDOE) and national laboratories in the USA, as Argonne, Los Alamos, or Idaho, the FRM II works with these partners to qualify and determine fuel candidates to convert its highly enriched fuel to a lower enriched one. They aim to develop new technologies as fuel and nuclear facilities to convert research reactors in the world [8].

Within Europe, the research on high-density LEU fuels is pursued by the HERACLES consortium, a collaboration of the European research reactors and the European fuel manufacturer Framatome-CERCA^{TM}. Additional supports of work on fuel development and production through European projects were initiated in order to determine uranium alloy candidates for fuel conversion, such as CP-HERACLES, LEU-FOREVER or EU-QUALIFY, supported by European HORIZON grants [9].

The FRM II works in direct collaboration with the French fuel manufacturer Framatome-CERCA^{TM}, with their workshop located in Romans-sur-Isère, to accelerate the development and potential industrialisation of a fuel that will match with the non-proliferation scope. The Framatome Romans site fabricates fuel assemblies for nuclear power reactors and fuel elements for research reactors using enriched uranium. It is separated into two sections, one for the fabrication of fuel elements for research reactors (CERCA^{TM}) and the second for the fabrication of fuel assemblies for nuclear power plants. The FRM II works with the R&D section of CERCA^{TM}, the **C**ERCA^{TM} **R**esearch and **I**nnovation **L**aboratory (CRIL) to develop this new fuel. All experimental work for this thesis has been achieved at this R&D workshop.

Regarding the worldwide development of new LEU fuels for research reactors conversion, mainly three uranium alloys candidates were extracted as promising candidates:

- **Intermetallic U_3Si_2** powder mixed with Al powder with an effective uranium density in a range of 4.8 to 5.6 $g \cdot cm^{-3}$;
- **Dispersed U-8Mo** powder mixed with Al powder with an effective uranium density of 8.0 $g \cdot cm^{-3}$;
- **Monolithic U-10Mo** in thin foil with an effective uranium density of 15.5 $g \cdot cm^{-3}$;

The choice of the monolithic U-10Mo as the most promising candidate to replace the current highly enriched U_3Si_2 fuel plate was realised, according to the uranium density needed up to 5 times from the actual uranium fuel density, due to enrichment divided by 5, in addition to promising irradiation tests already performed.

From uranium alloying to fuel plate manufacturing, all steps are described and analysed to have a deep knowledge of U-10Mo alloy and its manufacturing process. Different versions of irradiation tests and fuels were used to test the manufacturing process of monolithic U-Mo foil: from 1997 to 2012, mini-plate size of U-Mo was irradiated (RERTR-X), then from 2008 to 2012 on full size with AFIP-X fuel and finally, the first fuel assembly was irradiated in 2011 with AFIP-6 MKII [10]. Some fuel experiments designed with the global fuel architecture, like one of the FRM II for conversion, are shown in Figure 1.6 and 1.7.

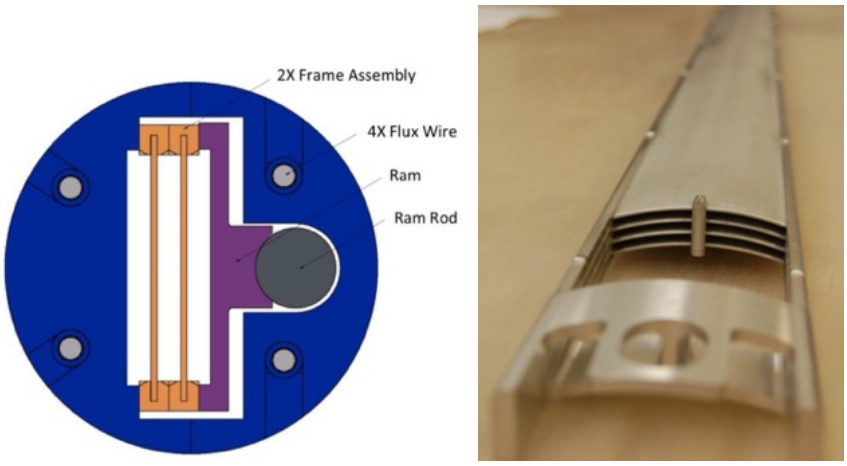

(a) Cross-section [11] (b) LEU assembly [10]

Figure 1.6: *Experimental device AFIP-7 for LEU fuel irradiation tests from RERTR*

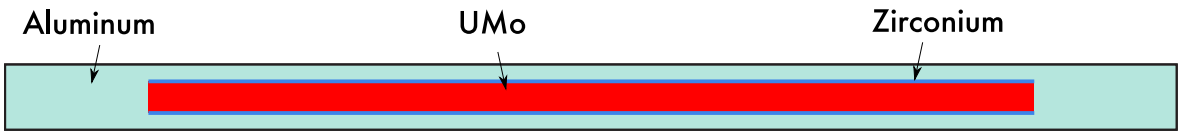

Figure 1.7: *Fuel plate composition for the FRM II conversion adapted from [6]*

TUM pushed the fabrication of monolithic fuel plates in Europe since its research on high-density fuels began. In 2005, a joint program between **C**ommissariat à l'**É**nergie **A**tomique et aux **É**nergies **A**lternatives (CEA), TUM and CERCA^{TM} was initiated to roll monolithic U-Mo foils. Nevertheless, this program was abandoned because of the considerable progress achieved by the US laboratories to produce those foils and the hope of getting the technology from the US partners.

In 2012, TUM and CERCA^{TM} agreed to buy from the US partners U-Mo bare foils to develop a European fabrication process for U-Mo fuel plates. Bare foil coated with Zr by **P**hysical **V**apor **D**eposition (PVD) as a diffusion barrier and aluminium cladding by the **C**ERCA^{TM} **C**EA **T**UM **W**elding **P**rocess (C2TWP) are the results of this effort. These foils were used for mini-fuel plate manufacturing, realised by CERCA^{TM} and used in the first in-pile irradiation tests based on European technology. This test, called EMPIrE for **E**uropean **M**ini-**P**late **I**rradiation **E**xperiment, confirmed the conservative swelling behaviour of U-Mo monolithic test plates produced using European technology.

As the US laboratories would not provide monolithic bare foils, TUM and CERCA^{TM} launched in 2019 a joint program to produce U-10Mo bare foils. This thesis is part of this effort.

Chapter 2

U-Mo for research reactor conversion

The manufacturing process with uranium and its alloys involves a deep knowledge of material properties. These aspects are momentous to understand the particularity of uranium alloys in terms of mechanics, thermic and specifical radiological aspects.

The section below is divided as follows concerning aspects of U-Mo alloys:

- **A brief historical background of uranium material** with its discovery, uses and microstructural aspects to understand the stakes to use this material as a manufacturing element;
- **Physical properties of U-10Mo alloy** used for the fuel manufacturing, with the influence of different parameters as impurities content, the manufacturing process involved and process parameters used;
- **Global thermal properties of U-10Mo alloy**.

2.1 History of uranium and few characteristics

Uranium, known as chemical element number 92, was discovered in 1789 by the German chemist Martin Heinrich Klaproth. Klaproth qualified this element as a "submetallic" or "pseudo-metallic" element, as he failed in obtaining metallic uranium from uranium oxide [12]. Its radioactivity was discovered in 1896 by the French Henri Becquerel, with a complement study of Marie and Pierre Curie using radium, extracted from uranium ores, as a medical treatment for cancer [12, 13]. Uranium was also used as a colourant for ceramic, glass and enamels [14]. A complete study and structure of metallic uranium was performed in 1841 by the French chemist Peligot and completed in 1936 with the X-ray method used to determine the crystalline structure. This complete study allows the use of uranium and its high energy level potential for nuclear purposes as neutron and energy production as well as for military applications with nuclear weapons [13, 15]. These applications concern different isotopes of uranium available in ores extracted. Natural uranium extracted is a mix of three isotopes in different proportions, as shown in Figure 2.1 [16, 17].

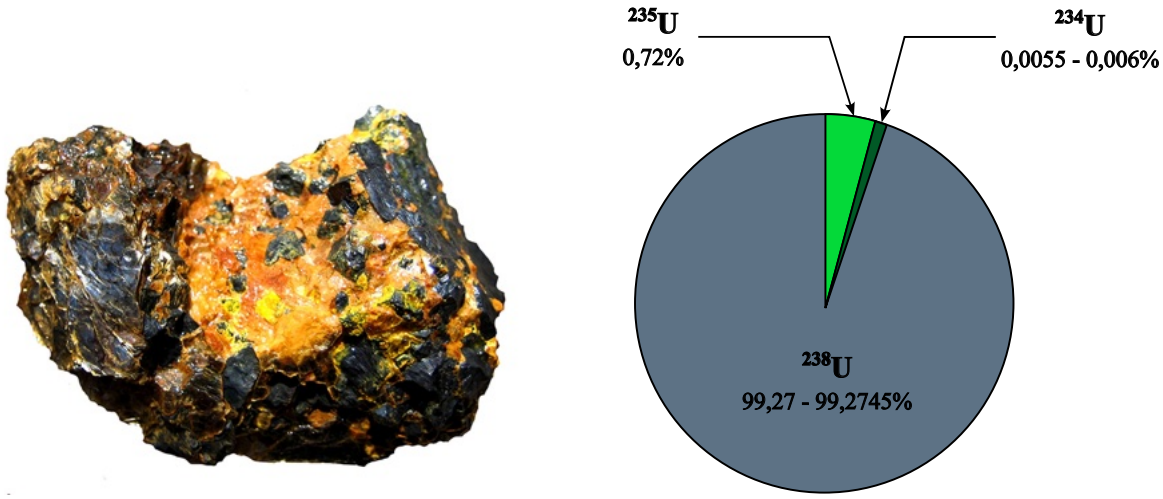

Figure 2.1: *Natural uranium ores extracted (left) with quantity in mass proportion for the three uranium isotopes (right):* ^{234}U, ^{235}U *and* ^{238}U

The most relevant isotope in the context of nuclear fission is ^{235}U thanks to its ability to be easily fissile. Nevertheless, natural uranium extracted is found with a quantity of ^{235}U too low to be used in most nuclear plants. Enrichment is then needed to increase the proportion available in nuclear fuels. Different processes can be used for increasing the relative quantity of ^{235}U in uranium alloy, as using the average speed of other isotopes when isotopes are separated into centrifuge [17] or new methods using laser technology [18]. Different uranium compounds are used for electricity production, with an average enrichment of 5 %, considered LEU fuel. At the same time, research reactors use fuels enriched up to 93 % for their research and neutron production purposes, considered HEU fuel.

Regarding its structure, uranium exists in three phases with different lattice parameters for each allotrope. They are presented in Figure 2.2, with the following characteristics:

- **α-U** - This phase has **an orthorhombic structure** stable below 668 °C. It is the common structure found in natural uranium and highly stable at room temperature with the following lattice parameters: a = 2.852 Å, b = 5.865 Å, c = 4.915 Å [12] / a = 2.854 Å, b = 5.865 Å, c = 4.955 Å [16];
- **β-U** - This phase has **a complex tetragonal structure** which appears between 668 and 775 °C [16] with the following lattice parameters: a = 10.759 Å, b = c = 5.656 Å [12] / a = 5.656 Å, b = c = 10.76 Å [16] / a = 10.52 Å, b = c = 5.57 Å [19];
- **γ-U** - This phase has **a cubic body-centred structure**, stable above 775 °C until melting temperature of uranium, 1135 °C: a = 3.524 Å [12, 16]

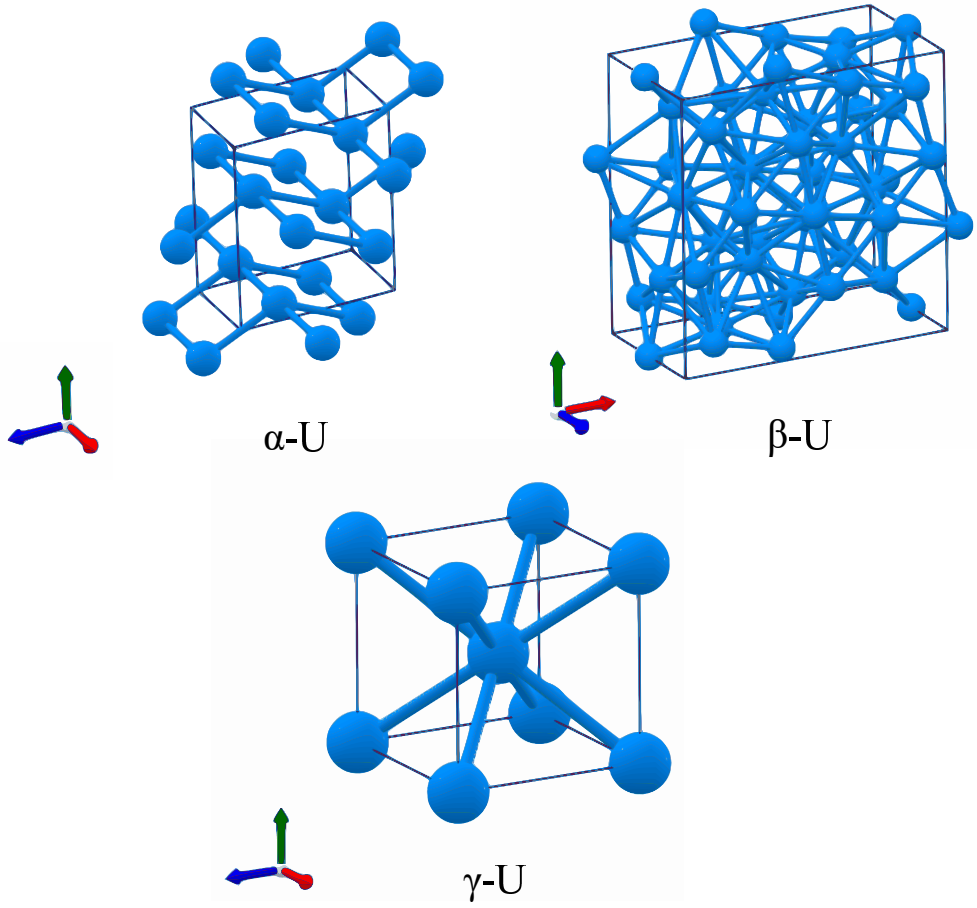

Figure 2.2: *Crystalline structures of different allotropes for pure uranium [20]*

α-U and β-U lead to structural anisotropy due to their unsymmetrical lattice structure. The strong anisotropy of natural uranium, especially with α-U structure, tends to make its use difficult for nuclear purposes, especially fuel manufacturing. It could lead to cladding rupture with dissimilar swelling and fission gas release in the reactor core. The two allotropes α-U and β-U were the subject of different studies to exhibit their electrical, mechanical and thermal properties [19, 21]. In this way, the γ-U structure exhibits the best potential for fuel irradiation and fuel manufacturing, as well as to exhibit a conservative swelling thanks to its centred cubic structure [22]. A complete study of γ-U was performed in 1949 by Wilson et al. to depict the entire lattice parameter of this structure [23].

In order to keep γ-U during both irradiation and fuel manufacturing, adding other elements tends to make it metastable into the alloy at room temperature. Different alloying of uranium exist and have been intensively studied, such as platinum Pt [24], niobium Nb [25], zirconium Zr [26] or molybdenum Mo which is used and fully depicted in this work.

2.2 Physical properties of U-Mo alloys

Uranium is usually combined with alloying elements to exhibit specific properties or to keep the crystalline structure required for the fission reaction and manufacturing processes. Different alloying elements are used, especially molybdenum Mo. Alloy composition, in terms of atomic structure, changes according to Mo content and manufacturing process applied with temperature changes, in addition to potential grain refinement or stress relief inducted by manufacturing processes. The properties of U-Mo alloys also change with this atomic structure changes. The uranium-molybdenum phase diagram shown in Figure 2.3 highlights the impact of Mo content in the different uranium structures or U-Mo alloy forms.

With no addition of Mo and according to temperature changes, the uranium phase diagram exhibits the three atomic structures presented in the previous section, with α-U present at room temperature. Adding 3 wt.-% of Mo prevents β-U appearance in the alloy. Regarding α-U, this structure is in higher proportion until 15 wt.-%. It is apparent from the phase diagram that a fourth structure different from what is presented until now is exhibited: $\gamma\prime$-U_2Mo. This structure is provided by the decomposition of γ-U structure and leads to the formation at the same time of an undesired α-U structure [28]. Under the eutectoid temperature of 560 °C, the cubic centred γ-U is decomposed into the orthorhombic α-U and the body centred tetragonal and intermetallic compound $\gamma\prime$-U_2Mo. Lattice parameters of this fourth phase structure were well described by Clarke et al. as follows: a = b = 3.427 Å, c = 9.834 Å [29].

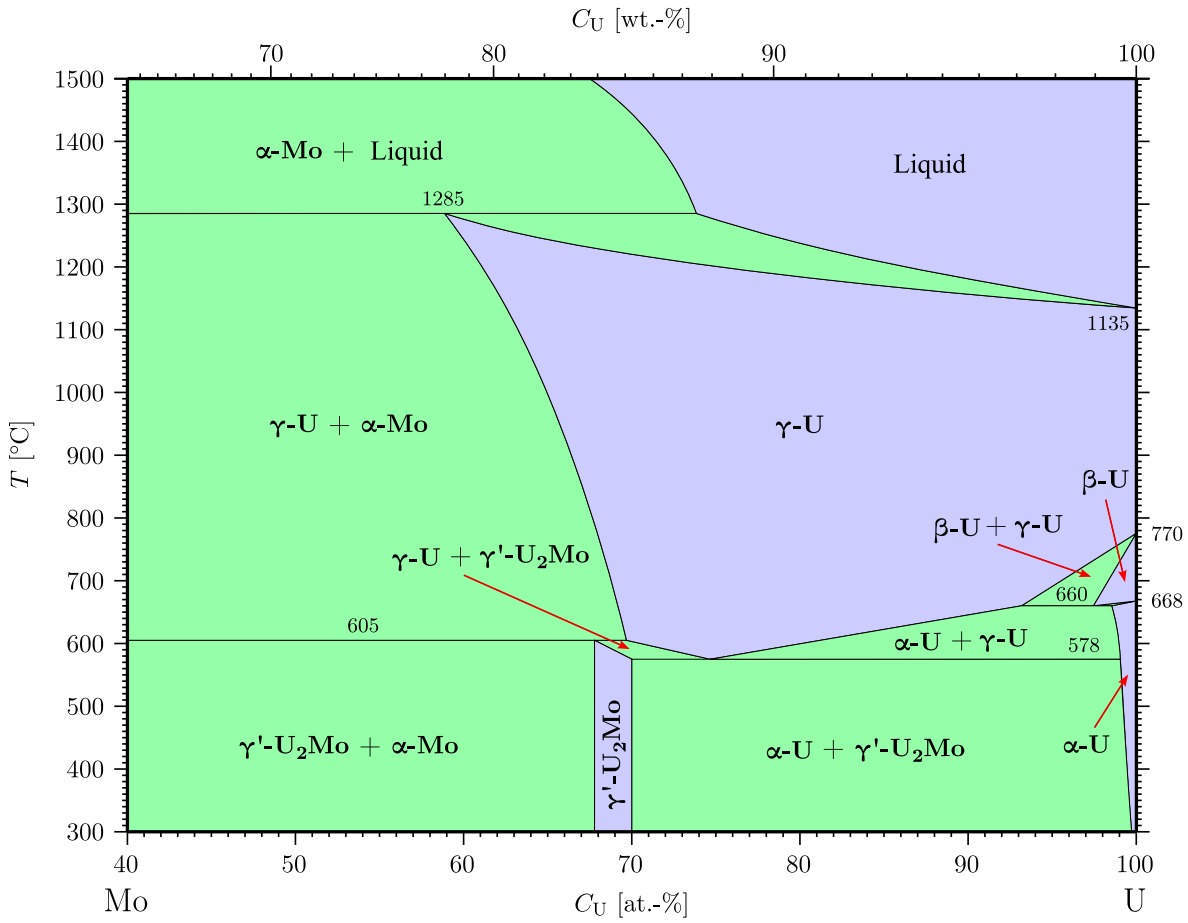

Figure 2.3: *Uranium-molybdenum phase diagram [27]*

Macroscopic anisotropy is led by microscopic structure and local anisotropy of grains. Then, adding alloying content to uranium is momentous for suitable atomic structure for both the manufacturing process and irradiation behaviour. Avoiding anisotropy will tend to make foil manufacturing more accessible, especially for processes which are feasible only in one direction, such as the rolling process.

These structures lead to different behaviour regarding irradiation, mechanical and thermal properties. Knowledge of these structures and their modification during manufacturing is necessary to control the final product and improve the quality and requirements for following manufacturing steps. Table 2.1 highlights mechanical differences between each phase **density** ρ, **Young's modulus** E, **yield stress** $\sigma_{0.2}$ and **tensile stress** σ_{TS}.

	Properties			
Structure	ρ ($g \cdot cm^{-3}$)	E (GPa)	$\sigma_{0.2}$ (MPa)	σ_{TS} (MPa)
α-U	19.12 [12], 19.07 [30]	148.37 - 208.49 [12]	270 [31]	720 [31]
β-U	18.06 [12], 18.37 [30]	148 - 210 [12]	295 [30]	575 [30], 700 [16]
γ-U	18.11 [12], 18.07 [30]	-	-	-

Table 2.1: *Properties of uranium-molybdenum phase structures at room temperature*

In these circumstances, the ideal Mo concentration would be at the eutectoid point, i.e., an average of 12 wt.-% where the only atomic structure transition would be from a combination of α-U and $\gamma\prime - U_2Mo$. However, increasing molybdenum addition will reduce the quantity of fissile material in the alloy. In addition to the choice of uranium structure, the balance between uranium density and the ability of the fuel to contain fission products is essential for irradiation and nuclear reactor performance. Addition of Mo in quantities between **8 and 12 wt.-%** tends to facilitate presence of γ-U into the alloy at room temperature and almost complete disappearance of $\gamma\prime$ structure from uranium alloy [32, 33].

In conclusion, choosing the Mo addition will impact the manufacturing process and the behaviour during irradiation. **the choice of 10 wt.-% in Mo** is defined here to replace the current FRM II fuel as the perfect candidate for a good balance between manufacturing feasibility and neutronic behaviour.

2.3 Mechanical properties of U-10Mo

Mechanical properties of metallic U-Mo alloys were subject to various characterisation experiments. Knowledge of properties is necessary to ensure good fission reactions with isotropic material, swelling and pressure involved during the irradiation, which affects the fuel during its operation, but also for manufacturing fuel foils.

The U-Mo alloy is a non-ferrous material that can be titanium or lead. According to Mo addition, U-Mo alloys exhibit different mechanical properties for different uses and purposes. This alloy was intensively studied by the US Army and nuclear institutions from 1954 to 1968 [34, 35]. Then, the number of papers and reports about U-Mo alloy has decreased until nowadays with new opportunities for this fuel, especially from the American side and since the beginning of the 21st century.

The different phase structure of uranium exhibits different values for main mechanical parameters as shown in Table 2.1. These differences are mainly due to the atomic structure, which highly affects macroscopic behaviour. The same remark can be said for the density of each phase due to atomic density in the atomic mesh. This section will highlight only mechanical behaviour for U-Mo alloys with mainly **γ-U phase structure** and with **nominal** Mo content of 10 wt.-%.

Due to radioprotection rules and the cladding process with Al alloy, the alloy will be combined with other conventional materials for manufacturing U-10Mo fuel foil. Table 2.2 highlights different mechanical characteristics at room temperature in comparison with U-10Mo for **Young's modulus** E, **yield stress** $\sigma_{0.2}$ and **tensile stress** σ_{TS}.

	Properties at room temperature		
Material	E (GPa)	$\sigma_{0.2}$ (MPa)	σ_{TS} (MPa)
Uranium U	177 [30]	200 - 220 [16, 30]	450 - 650 [16, 30]
Molybdenum Mo	325 [30]	345 [30]	435 [30]
Titanium Al6V4	100 - 140 [30, 36]	828 - 1100 [30, 36]	897 - 1205 [30, 37, 36]
AISI 316L	193 [38]	170 - 310 [30]	450 - 620 [30]
Inconel 600	214 [30]	172 - 345 [30]	550 - 690 [30]
U-10Mo	86	940	950

Table 2.2: *Mechanical properties of different metallic materials versus U-10Mo*

Regarding Young's modulus, U-10Mo is slightly less resilient than other conventional materials, even less than titanium Al6V4. Then, according to values of plastic stress, i.e. yield stress and maximum value of stress available, the tensile stress for U-10Mo are similar, which tends to a complex cold plastic deformation without cracks or other defects. Consequently, U-10Mo is more difficult to deform, which involves working with higher temperatures for foil manufacturing to decrease these values. These data do not consider other influent parameters such as sample test manufacturing scheme, impurity quantity or strain rate deformation during experiments.

In order to exhibit reference mechanical properties for U-10Mo with literature review and experimental data from reports and papers, the following assumptions and characteristics are considered:

- U-Mo alloys with Mo content in a range of **9.3 to 10.9 wt.-%** is considered as U-10Mo;
- Only for reference value, **impurity quantities** in samples tests are **not considered**;
- Experimental data summarised for reference data of U-10Mo mechanical properties are selected with a strain rate of experimental data which not overtaken **value of 5 $\mathbf{s^{-1}}$**. This aspect does not concern the strain rate dependency of U-10Mo mechanical properties explained in the next part;
- Only samples with mainly **gamma structure γ-U** are studied in this section. Some papers did not explicitly give the predominant crystal structure of the sample. As the manufacturing process involves casting at a high temperature in which the γ-U appears, and by considering that the addition of Mo at this threshold leads to metastable γ-U at room temperature, the assumption of **mainly gamma structure is justified**.

Different equations govern the plasticity of metallic material according to the material studied, the microscopic structure and the parameters involved, such as the power law or Ludwik-Hollomon equation. To plot fitting curves of yield stress and tensile stress from experimental values for U-10Mo, a power law is used as written in the following equation:

$$\sigma = K(T)\epsilon_p^{n(T)} \tag{2.1}$$

$K(T) = K_1(T_M - T)$: Hardening coefficient temperature dependent
$n(T) = \frac{K_2}{T_M - T}$: Power coefficient temperature dependent
ϵ_p : Plastic strain
T : Working temperature (°C)
T_M : Melting temperature of U-10Mo (°C)

By replacing ϵ_{p} by value of plastic deformation for $\sigma_{0.2}$ stress value in the Equation 2.1:

$$\sigma = K(T)0.002^{n(T)} \tag{2.2}$$

This power law written in Equation 2.1 is structured with the melting temperature $\mathrm{T_M}$ of U-10Mo to have an equation which converges to zero for high temperatures and matches as much as possible with the proper behaviour of molten material, i.e., with mechanical properties which reach values close to zero.

Plot and regression obtained from the previous equation are shown in Figure 2.4. Different experimental methods were performed in order to measure $\sigma_{0.2}$ and σ_{TS} values, such as tensile, compressive, bending and cantilever tests.

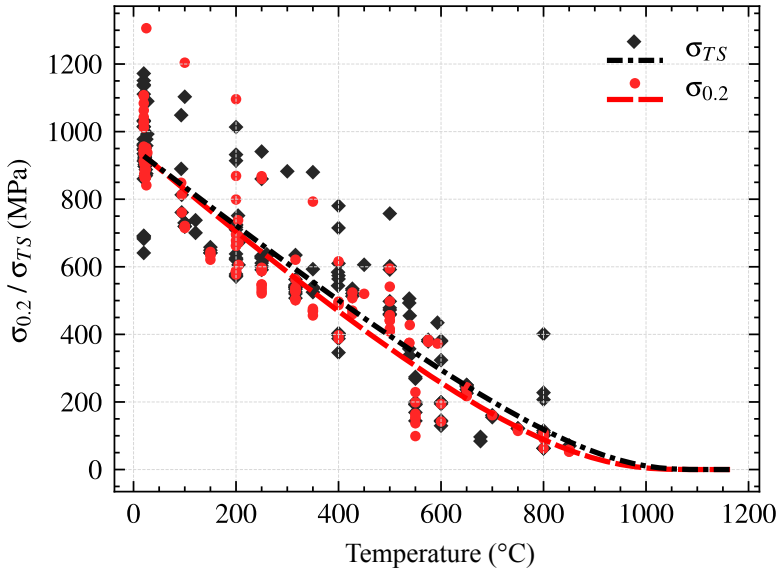

Figure 2.4: *Tensile stress σ_{TS} [39, 34, 40, 41, 42, 43, 44, 45, 46, 47, 48] and yield stress $\sigma_{0.2}$ [39, 34, 49, 42, 43, 46, 47, 48, 50, 51, 52, 53, 54] reference plots of U-10Mo according to temperature*

Both $\sigma_{0.2}$ and σ_{TS} vary according to temperature for U-10Mo, following the general trends of metallic material behaviours, with high values at room temperature and low values close to the melting temperature $\mathrm{T_M}$. $\sigma_{0.2}$ and σ_{TS} values slightly decrease when the temperature increases. They decrease mainly linearly until 0.6 to 0.7 of $\mathrm{T_M}$, before a sharp drop until $\mathrm{T_M}$. What is interesting in Figure 2.4 is the general decreasing pattern of $\sigma_{0.2}$ and σ_{TS}. Experimental values extracted from papers and reports highlight similar values for both mechanical properties. σ_{TS} is a few MPa higher than $\sigma_{0.2}$ due to its specificity to exhibit the highest stress that the material can handle. The two curves show similar trends. In conclusion, to begin the plastic deformation of U-10Mo, the stress applied needs to be as close as possible to σ_{TS}.

Peak values for both quantities are reached at room temperature, respectively, at 1250 MPa for σ_{TS} and just below 1200 MPa for $\sigma_{0.2}$. The variability is high at room temperature, with a wide range of values. The range of σ_{TS} at room temperature varies from 700 MPa to nearly 1200 MPa, and $\sigma_{0.2}$ ranges between 850 and 1300 MPa. The variability of these ranges declines increasingly by reaching $\mathrm{T_M}$. The material becomes more ductile in this range, and values are closest to each other. A lack of values from 650 °C is due to the severe difficulty of experimental setups at high temperatures, such as implementing a tensile test.

Some values are typically high compared to planned trends, with few values below these trends. These differences result from different manufacturing processes and treatments applied to the sample before tests. Indeed, several factors affect the mechanical properties of metallic material and, specifically, U-10Mo alloys. The alloy's mechanical behaviour is modified with impurities, affecting grain structure and grain growth during heat treatments. The following parts highlight these trends by plotting $\sigma_{0.2}$ and σ_{TS} for U-10Mo in different manufacturing states, with different carbon quantities, and then a strain rate dependency of the alloy.

2.3.1 Manufacturing process influence

The manufacturing process involved in fuel manufacturing contributes to being partially responsible for the variability of mechanical properties. As-cast samples contain randomly affected grain orientation due to molten liquid flow, which cools down, solidifies, and then randomly distributes the grains. Unlike as-cast samples, dislocation movements, work hardening and preferential grain orientation are provided by both hot and cold rolling. These could be described as the main phenomena which affect $\sigma_{0.2}$ for rolled samples, similarly to σ_{TS}. Finally, heat treatments are also significant in mechanical properties by grain refinement and manufacturing stress relieves for metallic materials, and here γ-U exhibition into U-10Mo alloys. The mechanical behaviour of U-10Mo is investigated with three manufacturing processes: as-cast, hot-rolled and cold-rolled. Figure 2.5 shows Young's modulus E values for as-cast, hot and cold-rolled samples with reference plot as the average of experimental values.

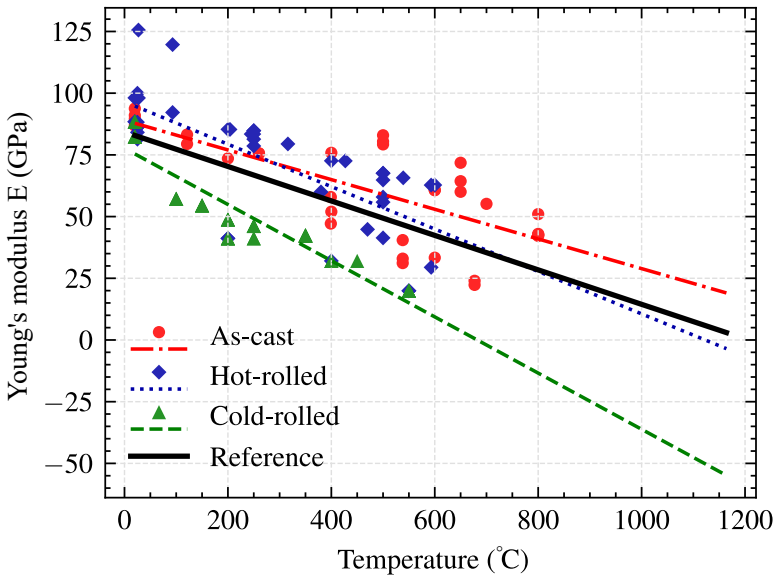

Figure 2.5: *Young's modulus E of U-10Mo according to temperature for as-cast • [48, 52, 54], hot-rolled ◆ [41, 43, 46] and cold-rolled ▲ [43, 44] samples*

The equation for the temperature dependence of Young's modulus E is established as:

$$E(T) = \frac{AT}{T_M} + B \tag{2.3}$$

A, B : Constants (A ≤ 0 & B ≥ 0)
T : Working temperature (℃)
T_M : Melting temperature of U-10Mo (℃)

Equation 2.3 is structured as the ratio between working temperature T and T_M to converge to low Young's modulus values for high temperatures and fit with mechanical behaviour near T_M. With the temperature increasing and similar to $\sigma_{0.2}$ and σ_{TS}, E decreases. The linear law seems to fit with as-cast and hot-rolled foil with a value of E close to zero when the temperature reaches T_M. Indeed, hot-rolled foils follow a similar linear decrease with temperature increase, with high accuracy from room temperature to 600 ℃. After 600 ℃, it appears and tends to make measurements difficult due to the high ductile behaviour of samples. Regarding cold-rolled foils, the plots do not fit the linear law due to negative values after 650 ℃. Schutuless et al. [43] highlight measurement difficulty due to non-linearity at an early stage of the stress-strain curves. Finally, differences in the experimental setup, with bending from Gates et al. [41], compressive tests from Joshi et al. [55], cantilever from Frazer et al. [40] and tensile for the others have minor influence on the results obtained for E. Figure 2.6 and 2.7 show $\sigma_{0.2}$ and σ_{TS} dependency with temperature and sample type.

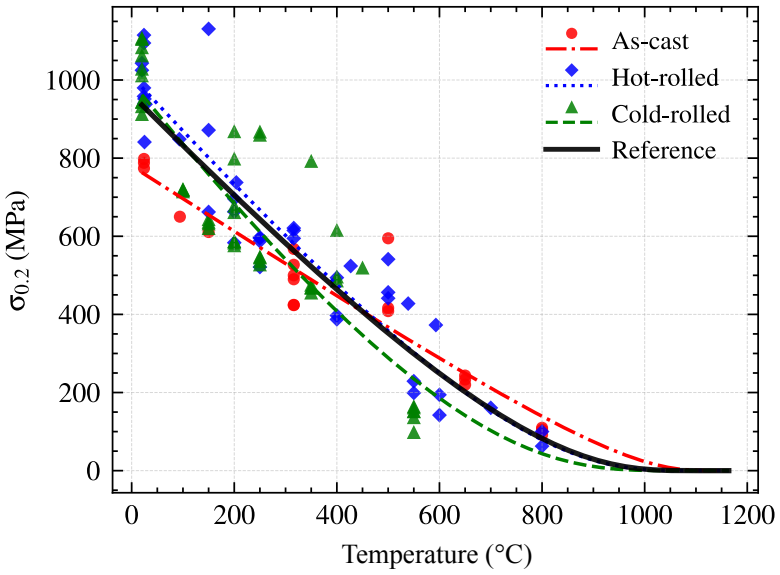

Figure 2.6: *Yield stress $\sigma_{0.2}$ of U-10Mo according to temperature for as-cast • [49, 48], hot-rolled ◆ [41, 49, 42, 45, 46, 43] and cold-rolled ▲ [44, 43] samples*

From room temperature to 400 °C, rolled samples exhibit higher $\sigma_{0.2}$ values than as-cast samples. Work hardening and rolled microstructure lead to this difference compared to the random distribution of as-cast samples. The plots converge to zero for temperatures close to the T_M, confirming the power law tendency of both $\sigma_{0.2}$ and σ_{TS} for U-10Mo. Figure 2.6 shows that grain refinement and previous treatments seem negligible close to T_M. U-10Mo alloys exhibit at high temperatures similar mechanical properties despite their manufacturing process. Similar to Young's modulus, experimental test procedures, as tensile or compressive tests, seem to not have an impact on reported values, with the addition of dynamic tension provided by Hoge et al. to measure yield stress and tensile stress [49]. Then, the same tendency as $\sigma_{0.2}$ is visible for σ_{TS} in Figure 2.7, with a portion from room temperature to 400 °C, with higher stress for rolled samples, and convergence to zero near to T_M.

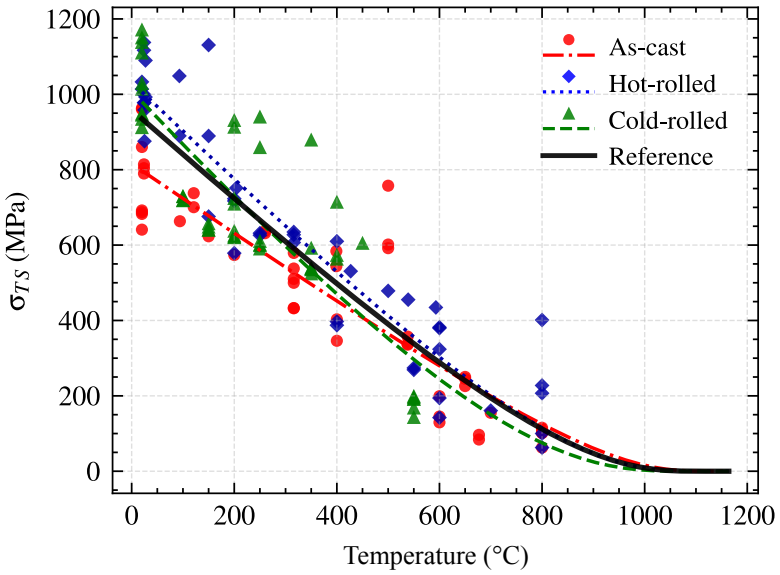

Figure 2.7: *Tensile stress σ_{TS} of U-10Mo according to temperature for as-cast • [49, 48, 52, 53, 54], hot-rolled ◆ [41, 49, 42, 43, 45, 46, 51] and cold-rolled ▲ [43, 44] samples*

2.3.2 Carbon content influence

Impurity content from investigated samples modifies the mechanical properties of U-10Mo alloys, especially for different carbon content. It tends to increase the value of yield stress $\sigma_{0.2}$ and tensile stress σ_{TS}, and leads to the formation of uranium carbides on grain joints, as highlighted by Devaraj et al. [56]. In addition, a high concentration of carbides affects grain size during heat treatment, which Hu et al. consider unfavourable for fuel irradiation [57]. Figure 2.8 shows σ_{TS} experimental values of for U-10Mo alloy for different carbon content.

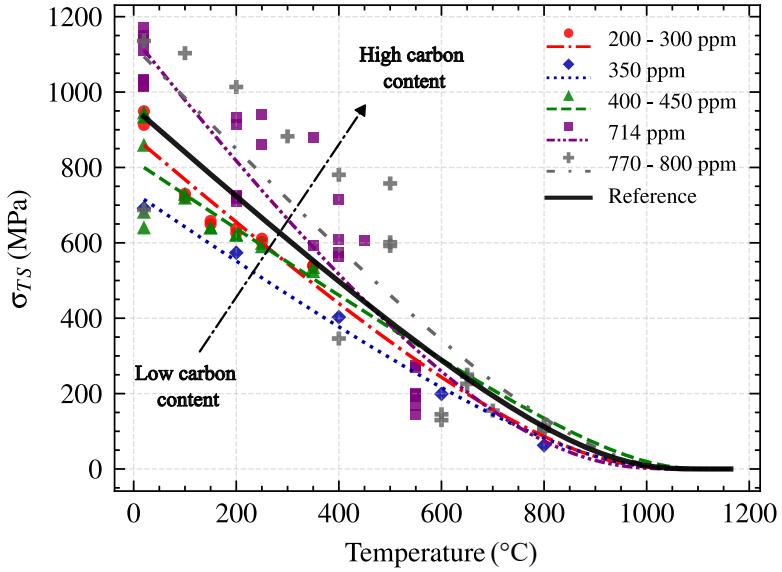

Figure 2.8: *Tensile stress σ_{TS} of U-10Mo according to temperature and carbon content Circle ● : [44] - Diamond ◆ : [52] - Triangle ▲ : [53, 44] - Square ■ : [43] - Plus ✚ : [52, 48]*

This plot reveals a gradual drop in σ_{TS} while carbon content decreases. Two ranges of carbon content from the reference value of σ_{TS} can be described in Figure 2.4. The first range is for a carbon content between 200 and 450 ppm. Peak values are reached at room temperature for 650 MPa to 950 MPa. A lack of data can be highlighted from the plot for samples with carbon content between 200 and 300 ppm at high temperatures. The second area is for values of carbon content higher than 700 ppm. In this section, experimental data of σ_{TS} are mainly between 1000 and 1200 MPa, with one point at 700 MPa.

According to carbon content, U-10Mo alloy seems more ductile with carbon content lower than 500 ppm. For carbon content higher than 500 ppm, as plotted in Figure 2.8, U-10Mo alloy seems to be harder with a higher value of σ_{TS}, which would affect the value of $\sigma_{0.2}$ value and, in consequence, stress needed for plastic deformation. Therefore, low values of impurities are recommended for U-10Mo foil manufacturing.

2.3.3 Strain rate influence

Deformation speed during the manufacturing process modifies the mechanical properties of the material used. Mechanical properties, as σ_{TS} and $\sigma_{0.2}$, are considered strain rate $\dot{\epsilon}$ dependent and considerably increase when the manufacturing process is performed at high temperatures, where microstructure grains become more ductile and more influent on deformation speed. Knowledge of U-10Mo properties under specific strain rate values for high temperatures is crucial for foil manufacturing. Figure 2.9 and 2.10 highlight stress value according to the strain rate and working temperature. The tensile stress σ_{TS} and yield stress $\sigma_{0.2}$ fitting curve uses the same Equation 2.1. The power law trends are the same but not representative of strain rate experiments because the value of plastic deformation is unknown and different from 0.2 %.

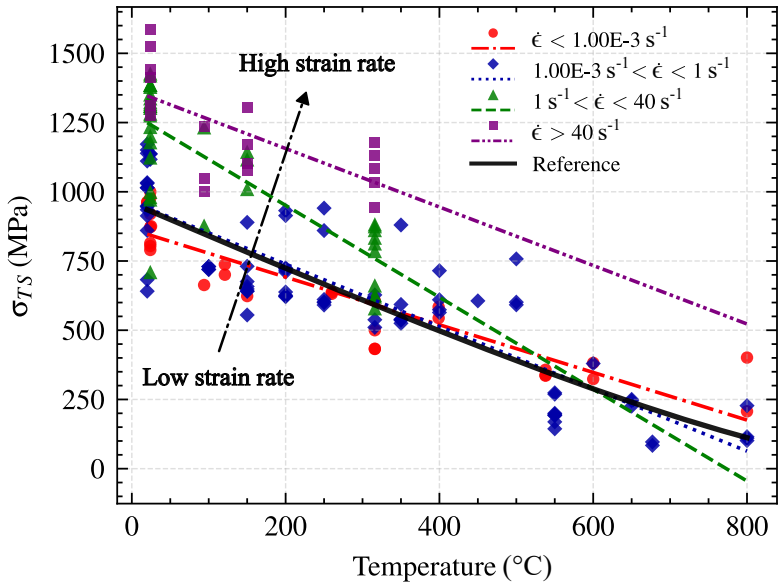

Figure 2.9: *Tensile stress σ_{TS} of U-10Mo according to temperature and strain rates Circle ● : [49, 42, 54] - Diamond ◆ : [42, 43, 44, 53, 48] - Triangle ▲ / Square ■ : [49]*

The mechanical properties of metallic materials are usually strain rate dependent for high temperatures and high strain rate values. When the strain rate is low, the material is more ductile. Conversely, a high strain rate achieves faster work hardening of the material, so $\sigma_{0.2}$ values increase with harder material. Conventional strain rate deformation for tensile tests is usually set between 7.00×10^{-5} to 2.50×10^{-4} s^{-1}, depending on specific mechanical values to measure [58]. Then, strain rate values higher than 1 s^{-1} are considered high for the deformation rate. For low strain rate values, fitting curves and experimental data are located mainly around the reference curves with a low variation of both mechanical values.

For a strain rate value of 1 s^{-1}, σ_{TS} values increase to 1500 MPa at room temperature. According to reports investigated, lower results reach values between 600 and 1200 MPa. The same phenomenon is visible for $\sigma_{0.2}$, with an increased value when the strain rate increases, which affects the formability of U-10Mo alloy. Nevertheless, a lack of data is reported due to the difficulty of setting up experiments about mechanical properties at high temperatures, especially with high strain rates. For U-10Mo alloy, only Hoge et al. reports values of mechanical properties in different conditions of manufacturing and impurities content at high strain rates, between 1 and 40 s^{-1} using dynamic tension loads to highlight the influence of high strain rate values [49].

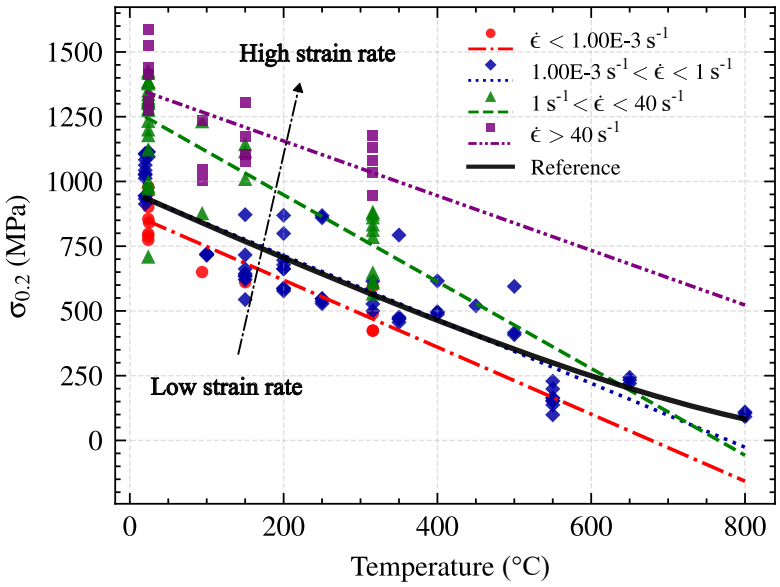

Figure 2.10: *Yield stress $\sigma_{0.2}$ of U-10Mo according to temperature and strain rates Circle ● : [49, 42] - Diamond ◆ : [49, 43, 44] - Triangle ▲ / Square ■ : [49]*

2.4 Thermal properties of U-10Mo

Material thermal properties are essential for manufacturing parameter choice, especially for processes involving complex heat exchanges such as laser cutting or hot rolling processes. Knowledge of U-10Mo thermal behaviour must be compared to conventional materials to understand the main differences between this alloy and conventional materials. Table 2.3 and 2.4 summurize these data, respectively for **density** ρ and **melting temperature** T_M, and then **emissivity** with wavelength of 650 nm ε_{650}, **conductivity** λ and **specific heat** C_p.

	Thermal properties at room temperature	
Material	ρ $(g \cdot cm^{-3})$	T_M (°C)
Uranium U	18.95 [30]	1132 [30], 1135 [59]
Molybdenum Mo	10.22 [30]	2621 [30], 2623 [59, 60]
Titanium Al6V4	4.42 - 4.43 [30, 61]	1649 [30, 37]
AISI 316L	8.00 [30, 62]	1418 [63]
Inconel 600	8.43 [64] - 8.47 [30]	1354 - 1413 [65]
U-10Mo	17.30 [44] / 16.84 [45]	1130 [35]

Table 2.3: *Density and melting temperature of different metallic materials and U-10Mo*

With the high quantity of uranium in the alloy, U-10Mo density is significantly higher than other conventional metallic materials, around twice that of stainless steel or nickel alloy and four times higher than titanium alloy. Even with the high melting temperature T_M of Mo, U-10Mo still has a reasonable melting temperature for the casting process. The alloying process is difficult due to the high T_M value for the raw molybdenum, which needs a specific melting process, usually arc melting, to increase the temperature locally.

	Thermal properties at room temperature		
Material	ε_{650}	λ $(W \cdot m^{-1} \cdot K^{-1})$	C_p $(J \cdot kg^{-1} \cdot K^{-1})$
Uranium U	0.265 [30] - 0.540 [66]	27.6 [30]	116 [30]
Molybdenum Mo	0.370 [66]	137 [30]	305 [60]
Titanium Al6V4	-	6.7 - 7.2 [30, 61]	560 [30]
AISI 316L	0.350 [66]	15.6 [30]	499 [67]
Inconel 600	0.180 - 0.210 [68]	15.9 [30]	444 [30]
U-10Mo	0.940 - 0.960 [69]	12 - 12.1 [46]	134 - 140 [35]

Table 2.4: *Thermal properties of different metallic materials and U-10Mo*

Regarding Table 2.4, the emissivity is high and close to 1 for unoxidised U-10Mo compared to other materials. It means that the alloy absorbs almost all heat provided by thermal radiation. However, as oxidation occurs rapidly on U-10Mo alloy and goes to golden and purple colour according to temperature and time exposure, emissivity decreases towards 0.8 to 0.7. It affects radiation properties from laser heat sources [69].

Next, U-10Mo exhibits a low conductivity value at room temperature compared to other materials and more than double from uranium value and ten from molybdenum. Low thermal conductivity could be explained by the presence of γ-U, which stays in metastable condition for the alloy, where mainly α-U is present in unalloyed uranium at room temperature. The conductivity stays the same in each direction compared to natural uranium, where conductivity would change according to direction, even with the highest value.

Finally, at room temperature, the specific heat of the alloy is also low compared to stainless steel or titanium. U-10Mo alloy is then easier to increase in temperature compared to these materials, but on the other hand, heat is lost faster than the other metallic materials. This property has to be considered for high-temperature processes for heating and manufacturing time to keep the required material properties in a high-temperature range of U-10Mo.

Figure 2.11 shows conductivity and specific heat properties at high temperatures of U-10Mo. Experimental data highlight the linear increase of both with temperature, which means high temperature leads to heating the material rapidly and tends to keep the temperature. U-10Mo alloys with different quantities of impurities and fissile material were tested, i.e., **d**epleted **u**ranium (DU) and LEU, to highlight potential differences in thermal interactions. The experimental data for these two properties [44, 35] do not highlight main variations. This similarity represents interesting data for a first usable manufacturing parameters, for future LEU foil production, with a first batch of experiments with DU-10Mo foil manufacturing.

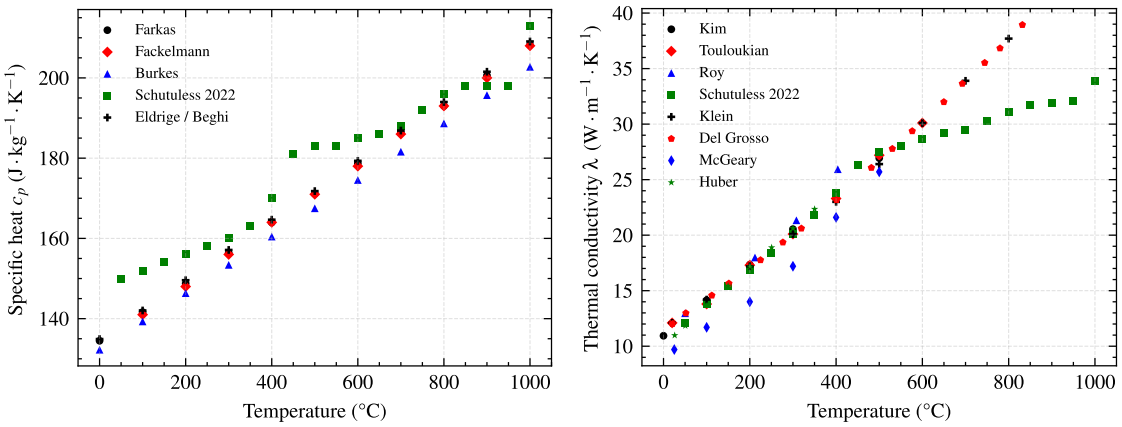

Figure 2.11: *Specific heat c_p [6, 44, 46, 35] and conductivity λ [35, 70, 44, 71] of U-10Mo according to temperature*

2.5 Manufacturing line for U-10Mo bare foil production

The FRM II fuel plate manufacturing follows different steps to obtain the desired design and properties. Raw molybdenum and uranium are first alloyed in a vacuum arc melting furnace. This step ensures the homogenisation of the material, which is difficult to obtain due to the high melting temperature of molybdenum, for further steps. It provides U-10Mo buttons feedstock for further ingot casting before the rolling step. Feedstock production is not mandatory, but it allows better homogeneity in the coupon by remelting chunks as many times as needed to achieve desired homogeneity. Then, U-10Mo feedstock is melted by an induction furnace in a graphite or copper mould with the addition of a lubricant. The shape of the alloy after arc melting and induction casting is shown in Figure 2.12.

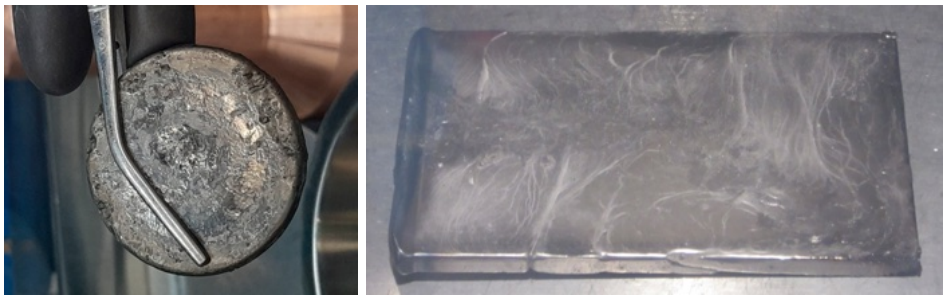

(a) U-10Mo button - Arc furnace (b) U-10Mo ingot - Induction furnace

Figure 2.12: *U-10Mo from different casting process before rolling*

The ingot is then encapsulated into a canister welded by laser beam technology. This assembly is then hot rolled to reduce the ingot thickness until the thickness target is achieved. Finally, the U-10Mo bare foil is removed with a laser cutting process and adjusted according to the required geometric dimensions while removing some defects prior to zirconium coating by PVD and aluminium cladding with Framatome proprietary manufacturing process C2TWP. Laser technology is used twice in the U-10Mo monolithic plate manufacturing pilot line for encapsulating and foil cutting as an innovative manufacturing process. The manufacturing process development from ingot casting to laser cutting, from U-10Mo ingot to bare foil, is presented in Figure 2.13.

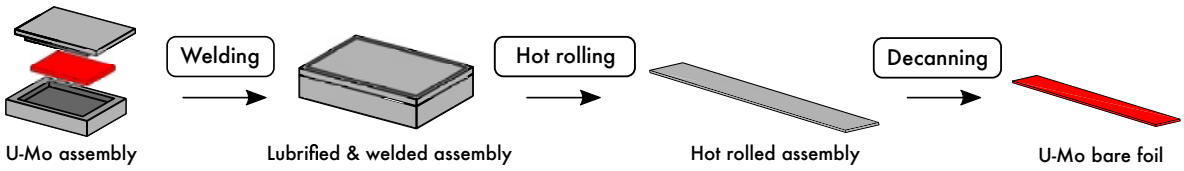

Figure 2.13: *Manufacturing pilot line for U-10Mo bare foil presented in this work*

Part II

— U-10Mo ingot sealing with laser beam welding process —

Manufacturing U-10Mo bare foils for the FRM II involves successive manufacturing steps with critical aspects regarding the irradiation and fuel assembly requirements. The first process is **L**aser **B**eam **W**elding (LBW) to seal the U-10Mo casted ingot into a metallic canister before the hot rolling process. The canister's LBW is investigated to extract the welding parameters required to handle the hot rolling process. Different materials are tested with different parameters to understand their influences on the bare foils produced.

This part is separated as follows:

- **A literature review of the laser technology** performed and shared with **L**aser **B**eam **C**utting (LBC) presented after in this work in part III. In addition, **a review of the application of laser technology for metallic welding** is realised to understand the physical aspect of laser welding and apply the first range of data for the U-10Mo bare foil manufacturing line;
- **Descritpion of material and machines used for LBW for this manufacturing line**, with the range of parameters used and experimental set-up for the experiments performed;
- **LBW results from various experiments** studied to highlight the parameters influence on laser welds produced with variation in weld depth and width.

Chapter 3

State of the art of laser beam welding process

3.1 Theory about laser technology

The LASER, for **L**ight **A**mplification by **S**timulated **E**mission of **R**adiation is used in many sectors such as medical, metrology or industrial to improve production lines and have better quality on manufactured products [72]. It allows a high flexibility level for manufacturing different materials, such as plastic and metallic parts. It is nowadays considered an advanced technologic gap [73] in industry. Its uses increased from 1960 to nowadays, with more than 25% of the worldwide applications only in Europe as shown in Figure 3.1.

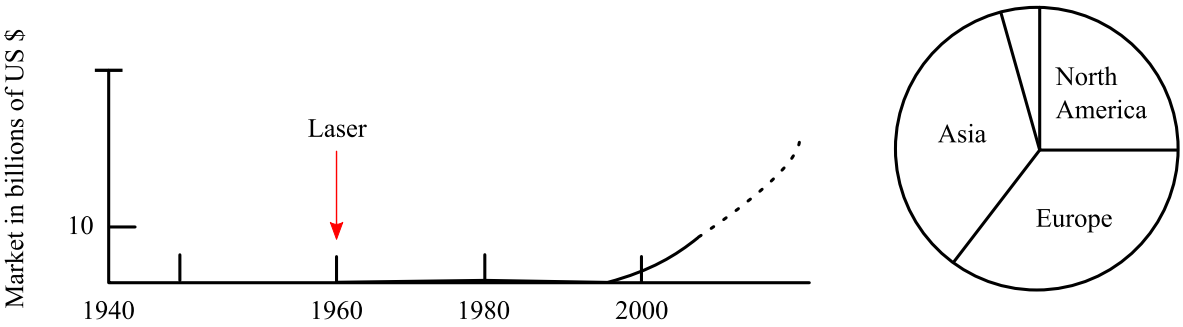

Figure 3.1: *Laser economic markets since 1940. Proportion of laser used in the world* [73]

The laser emission consists of **a focalised source of photons** provided by excited atoms, which pass from a high energy level to a lower one as described in Figure 3.2. A succession of these energy transitions provides numerous photons reflected on mirrors in the laser chamber for laser beam emission.

A laser fibre conveys this laser beam emitted, and then a lens adjusts the spot according to the process involved. These systems allow the production of laser beams with a high energy level located in a small area and with different wavelengths according to parameters such as the gas composition of the laser chamber and the type of laser source used.

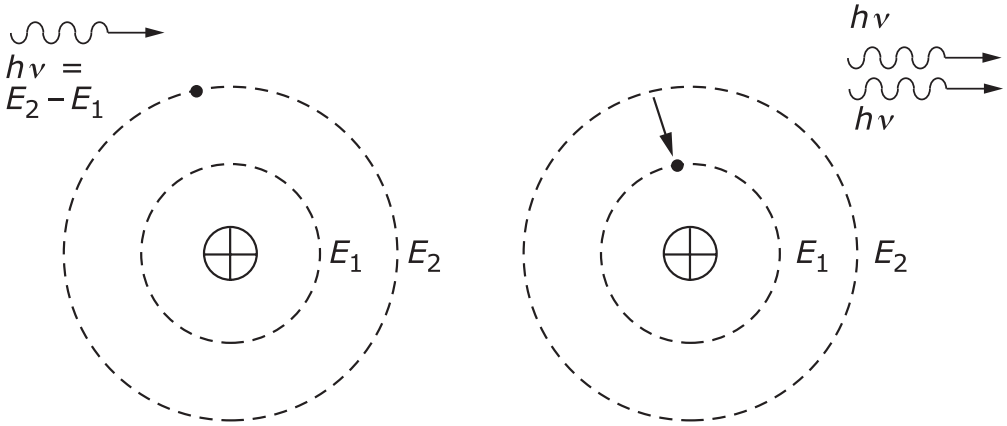

Figure 3.2: *Photons emissions for laser emission [74]. An incident photon will stimulate the transition of an electron from energy level E_2 to E_1. This decay will provide a photon which, by multiple reflections, will repeat this process and provide a laser beam.*

As excited atoms lose their energy through this process, their population will decrease exponentially with time. This decrease will directly impact the power of the laser beam provided. External energy is provided to maintain a higher population of excited atoms in the chamber and to avoid decreased laser power. This phenomenon is called the principle of population inversion by pumping systems. These systems could be optical, electrical or chemical, with an electrical generator or chemical reaction in the laser chamber [72].

Characteristics and sources of laser vary according to the desired application. CO_2 laser, Nd: YAG, diode and fibre laser are used to perform different applications with different wavelengths and laser power, which could go up to thousands of watts according to the application [74]. Other laser sources, such as helium-neon, cadmium or ruby laser sources, exist for other applications. However, their power, usually around ten to 100 W, must be higher to weld metallic materials [75].

The laser beams can be emitted in continuous or pulsed waves and in a microscopic amount of time as Q-switched or femtosecond laser for specific applications [73]. For example, continuous waves are mainly used for welding because of the high energy density level in a small surface area when pulsed would be more used for surface cleaning, where only the surface needs to be affected by the laser. For laser beam cutting and laser beam welding, laser emission is fully characterised **by energy** and **laser spot size**.

Parameters to characterise Gaussian laser beam

The laser beam is considered as **a symmetrical paraxial wave**. Photon flux provided by the laser source is subject to angular spread on its optical path, which affects its shape around the beam axis. The light propagation follows **the Helmholtz wave equation** described below:

$$\nabla^2 U + k^2 U = 0 \tag{3.1}$$

U : Wave function
k : Wavenumber as $k = \frac{2\pi}{\lambda}$

A solution for the Helmholtz equation 3.1 is one including Gaussian law, well described and established in 1773 by Joseph-Louis Lagrange and Carl Friedrich Gauss in 1835. The Helmholtz equation's complete resolution is well described in laser and photonics literature [76]. By solving this equation, and for an ideal laser source, the intensity distribution $I(\rho, z)$ along the laser beam can be defined [76]:

$$I(\rho, z) = I_0 \left[\frac{w_0}{w(z)} \right]^2 \exp\left[-\frac{2\rho^2}{w^2(z)} \right] \tag{3.2}$$

I_0 : $I(0,0)$ corresponding to the highest intensity value of laser beam
$w(z)$: Width radius depending on z position
w_0 : Width radius for $z = 0$ in focal plane
ρ : Radial position as $\rho = \sqrt{x^2 + y^2}$

This equation highlights two essential values, w_0 and z_0, to describe the laser beam represented in Figure 3.3.

First, w_0 is considered as **waist or width radius**. This width value corresponds to the width measured at the focal plane of the beam, i.e., for $z = 0$. Then, z_0 is considered as **Rayleigh length**. It is the position on the laser beam when the spot's width equals $\sqrt{2}w_0$. With these two values, $w(z)$ can be obtained by the relationship between w_0, z position and z_0 [76]:

$$w(z) = w_0 \sqrt{1 - \left(\frac{z}{z_0} \right)^2} \tag{3.3}$$

The Rayleigh distance z_0 is linked to wavelength λ and w_0 by the following equation [76]:

$$z_0 = \frac{\pi w_0^2}{\lambda} \tag{3.4}$$

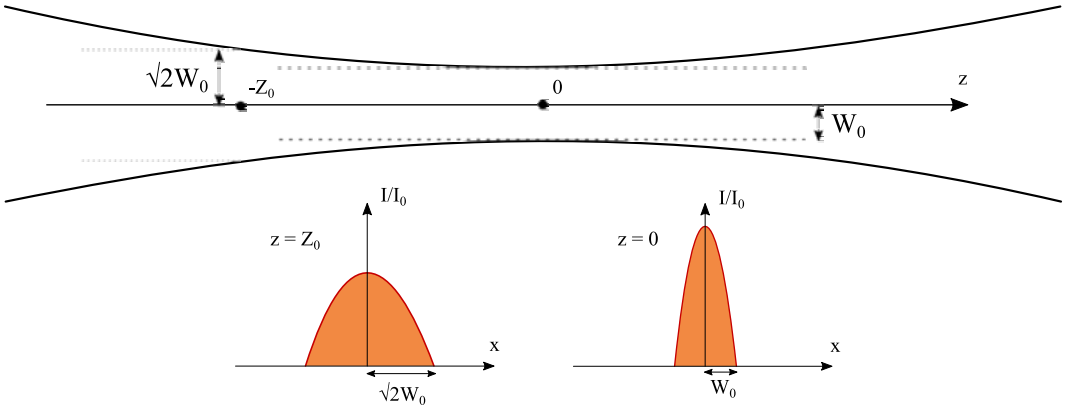

Figure 3.3: *Gaussian beam scheme. Bottom left: normalised beam intensity for $z = z_0$ with a large width profile and low-intensity value / Bottom right, normalised beam intensity for $z = 0$ with a low width profile and the highest intensity*

Finally, the last parameter to characterise a Gaussian profile is the M^2 factor. This factor measures the laser beam quality by **the ratio** between **divergence angle measured from the source** $w_m\theta_m$ and **theoretical divergence angle valueee** $w_0\theta_0$ of the Gaussian law:

$$M^2 = \frac{w_m\theta_m}{w_0\theta_0} \tag{3.5}$$

M^2 values close to 1 characterise a perfect laser quality. The quality of the laser decreases for higher values. Laser sources with high power often have a high M^2 factor due to the complexity of having a powerful laser source and, simultaneously, a laser beam with high quality.

Different parameters are available in order to characterise the Gaussian beam:

- Wavelength λ;
- Peak intensity I_0;
- Both waist radius w_0 and Rayleigh distance z_0;
- M^2 factor for beam quality.

These parameters, added with the intrinsic characteristics of the laser source, are essential to describe a laser beam's trends according to the process performed and parameters to consider.

3.2 Theory of laser beam welding

In metallurgy, welding is the most used manufacturing process to assemble metallic parts. Each welding corresponds to a specific assembly property, such as being tight to liquid for tubes or being resilient under loads for bridges. In addition, weld position, thickness part and material properties are a few of the parameters to take into consideration before performing the welding process, especially for **L**aser **B**eam **W**elding (LBW).

The term LBW refers to **an accurate energy-based process** able to weld with good depth penetration and without external metal supply compared to plasma or arc welding with the lowest energy density as shown in Figure 3.4.

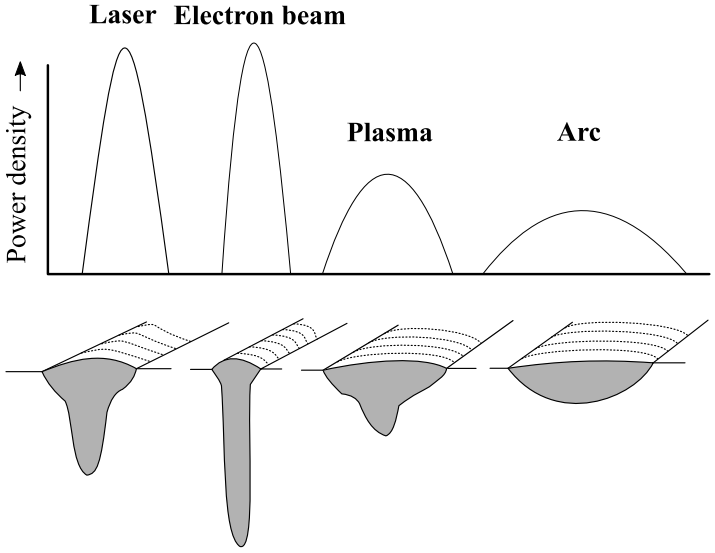

Figure 3.4: *Power density and appearance for a different welding process [77]. Laser and electron beams share the same power density profile, with deeper penetration for electron beam welding. Plasma and arc welding provide less power density than laser and electron beams, explaining a lower penetration.*

Free electrons available at the surface of the metallic sample will transfer laser energy to the plate into heat. As the temperature of the surface is increasing, heat absorption follows the same path by increasing conductivity and specific heat for metallic material, and the temperature increases to reach boiling temperature. This temperature associated with recoil pressure on the top of the liquid allows the formation of a keyhole inside the part to be welded. Then, the absorbed energy locally melts part of the material and bounds them after cooling.

Three areas can be delimited in the sample welded by LBW:

- The **melt pool**, or melted area, corresponding to the metal liquid produced after the keyhole and generated by the laser;
- The **H**eat **A**ffected **Z**one, or **HAZ**, corresponding to the affected area by the heat of the melt pool but without solid-to-liquid phase transition ;
- The **base metal**, or **unaffected area**, corresponds to the area unaffected by the laser or the melt pool heat.

.

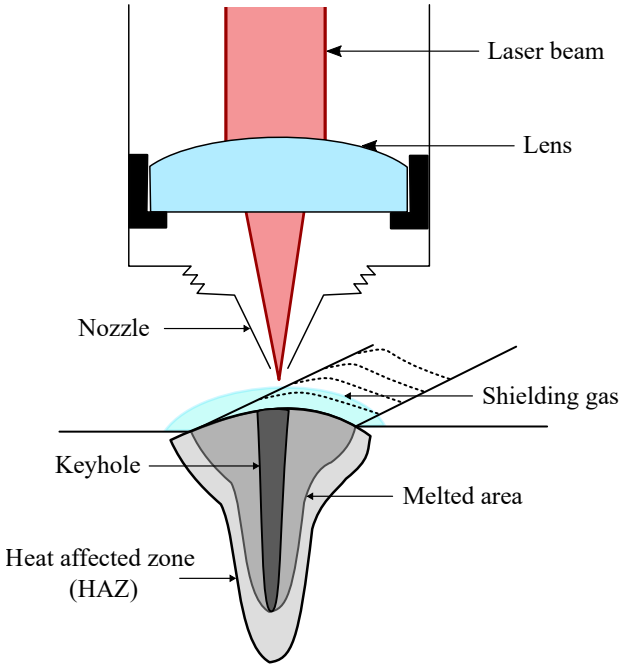

Figure 3.5: *Laser beam welding schematic adapted from [78]. The laser beam is focalised through a lens to melt the metallic part to weld. The welding begins with a keyhole formation where the molten flow is guided. The weld geometry is composed of a melted area and a heat-affected area. The nozzle provides a shielding gas to avoid surface oxidation.*

For pulsed laser, six parameters impact the welding process, from the visual aspect to microstructure: laser power, working distance, welding speed, both pressure and nature of shielding gases, laser frequency and pulse time. Continuous wave does not consider frequency and pulsed time by instantly delivering the total energy amount, which is more often used than pulsed for welding for this aspect. Optimisation of parameters is needed to obtain desired sets for welding and avoiding defects as inclusions, thermomechanical cracks, geometric defects, or fusion lacks [79, 80, 81].

The absorbed energy provided by **the laser spot locally melts part of the material** and then links them after cooling and solidification. The laser beam welding process is realised under an inert local area with shielding gas to first prevent surface oxidation and, in a second time, to evacuate residual particles on the surface that could appear during the welding. It has numerous advantages compared to the conventional welding process: no change in part geometry, high precision, no external metal needed, a small affected area, and weld length and width reduced [82], with a low cost of tools thanks to a non-contact between parts and consumables. Compared to conventional process as plasma or arc melting, **the energy density is locally higher**. In contrast, the energy density is lower for arc and plasma welding, with less deep penetration and a larger affected area.

LBW involves different interactions between the metallic sample and the laser. Indeed, lasers with electrons interact with material by free electrons available on the material surface. These are then excited by different means with material emission and absorbance and with the wavelength of the laser source used. In addition, conductivity, specific heat and density impact heat transfer during LBW and must be known to optimise and improve the process.

Interactions between laser and metallic parts

Processes involving lasers are mainly conducted by thermal equations involving laser heat provided to the surface and heat exchanges occurring to the rest of the part. Knowledge of these equations and thermal material properties is essential to understand the critical parameters of laser and improve the process according to the desired results.

The volumetric enthalpy used for the energy balance equation is described in Equation 3.6:

$$H = \int_0^T \rho(\theta) C_p(\theta) d\theta \tag{3.6}$$

ρ : Material density $(\mathrm{kg \cdot m^{-3}})$
C_p : Specific heat $(\mathrm{J \cdot kg^{-1} \cdot K^{-1}})$

The thermal energy balance equation can be written as Equation 3.7:

$$\frac{\partial H}{\partial t} + \frac{\partial (u_i H)}{\partial x_i} + \frac{\partial (u_i \Delta H)}{\partial x_i} = \frac{\partial}{\partial x_i}\left(\lambda(T, x_i)\frac{\partial H}{\partial x_i}\right) + S_v \tag{3.7}$$

H : Volumetric enthalpy $(\mathrm{J \cdot m^{-3}})$
u_i : Convective flow in i direction $(\mathrm{m \cdot s^{-1}})$
λ : Conductivity $(\mathrm{W \cdot m^{-1} \cdot K^{-1}})$
S_v : Volumetric heat source $(\mathrm{J \cdot m^{-3} \cdot s^{-1}})$

Boundary conditions on the top surface affected by the laser are modelled by convection, conduction and radiation between different environments according to the following equations:

Boundary conductivity

$$Q_{CD} = \sum_i \lambda_i \frac{\partial T}{\partial n} \tag{3.8}$$

Q_{CD} : Heat flux involved by conduction with external environment $(\mathrm{W} \cdot \mathrm{m}^{-2})$
λ_i : Thermal conductivity in i-axis $(\mathrm{W} \cdot \mathrm{m}^{-1} \cdot \mathrm{K}^{-1})$
n : Normal vector to the surface
T : Temperature of the surface (K)

Boundary convectivity

$$Q_{CV} = \sum_i h_i (T - T_i) \tag{3.9}$$

Q_{CV} : Heat flux involved by convection with external environment $(\mathrm{W} \cdot \mathrm{m}^{-2})$
h_i : Heat coefficient transfer in i-axis $(\mathrm{W} \cdot \mathrm{m}^{-2} \cdot \mathrm{K}^{-1})$
T_i : Fluid temperature in i-axis (K)
T : Temperature of the surface (K)

Boundary radiation

$$Q_R = \sigma \varepsilon (T^4 - T_0^4) \tag{3.10}$$

Q_R : Heat flux involved by radiation with external environment $(\mathrm{W} \cdot \mathrm{m}^{-2})$
σ : Boltzmann constant $(\mathrm{W} \cdot \mathrm{m}^{-2} \cdot \mathrm{K}^{-4})$
ε : Emissivity of the solid
T_0 : Temperature of the fluid (K)
T : Temperature of the surface (K)

Boundary equations for conduction, convection and radiation define boundary conditions for thermal equation balance. By considering Q_L the heat flux provided at the top surface by the laser, the boundary condition can be written as :

$$Q_{CD} = Q_L + Q_R + Q_{CV} \tag{3.11}$$

A Gaussian law usually governs laser beam power and volumetric heat generated by the laser, a function of the position of the laser on the plate, laser power or radius beam according to:

$$q(r) = \frac{\alpha P}{\pi r_0^2} \exp\left(-\frac{2r^2}{r_0^2}\right) \tag{3.12}$$

P : Laser power (W)
r_0 : Beam radius (m)
r : Radius at work distance (m)
α : Constant

The interaction between the laser and the material represents the main subject of papers and studies for laser processes to understand how this interaction could impact results and thermal exchanges through the laser. When the laser beam interacts with matter, its energy will be transmitted through three main paths, as explained in Figure 3.6. Some energy is reflected at the surface material, while others are absorbed and transmitted through the part. For opaque and metallic materials, the emission is not transmitted.

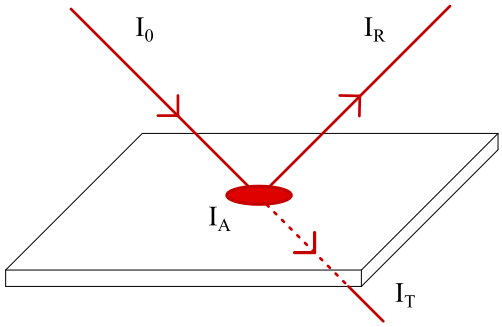

Figure 3.6: *Laser optical path after contact with a part. A fraction of the initial intensity I_0 goes through the part with I_T intensity. A part is reflected and transmitted with respectively I_R and I_T intensity, and, a part is absorbed by the part, I_A.*

This energy absorption is the source of Q_L as the laser provides the heat flux. Furthermore, Q_R, the radiative heat flux loss involved in applying the laser to the material, is also an important parameter. The absorbance affects the heat exchange, particularly with laser use. The part absorbed, I_A, impacts the material's mechanical and thermal properties by heating the material. This change in thermal and mechanical behaviour is critical for numerous processes, such as laser beam welding or cutting.

3.3 Laser technology for metallic canister welding

Canister design is specific to the welding process of U-10Mo bare foil manufacturing. According to the US development, the uranium ingot obtained after induction casting is encapsulated in a stainless steel window frame and then closed with plates on the top and bottom. These parts are welded by **T**ungsten **I**nert **G**as welding (TIG) on both plates with lubrication of the uranium coupon to avoid stickiness [83, 84, 85]. The term assembly will be used solely for a set formed with an ingot encapsulated into a welded canister. Low carbon stainless steels are usually used for their mechanical and thermal properties as well as **S**tress **C**orrosion **C**racking ability (SSC) [86]. Low carbon content is also needed to avoid contamination of uranium ingot with carbon particles and facilitate welding [87]. The canister's design and the encapsulation objective described in the present work differ from the US development. For the US development, the welding realised is not tight and necessary for zirconium coating performed by co-rolling. The canister ensures a constraint between the zirconium foil and the uranium ingot. The main objectives for the FRM II development are to enclose the U-10Mo ingot inside a physical barrier to avoid external contamination and reduce oxidation. The canister shown in Figure 3.7 and adapted for LBW is composed of two parts:

- the bottom part called **housing**, where the ingot is set before the welding process. Backlashes are machined as tight as possible for ingot encapsulating and according to their geometry from the induction casting;
- the upper part called **lid**. Only the outer border of the lid is welded to the canister. Then, this part is thinner than the rest of the lid to allow good laser penetration and ensure mechanical links. A weld depth value higher than this part thickness and sufficient width for mechanical strength is needed to achieve the welding.

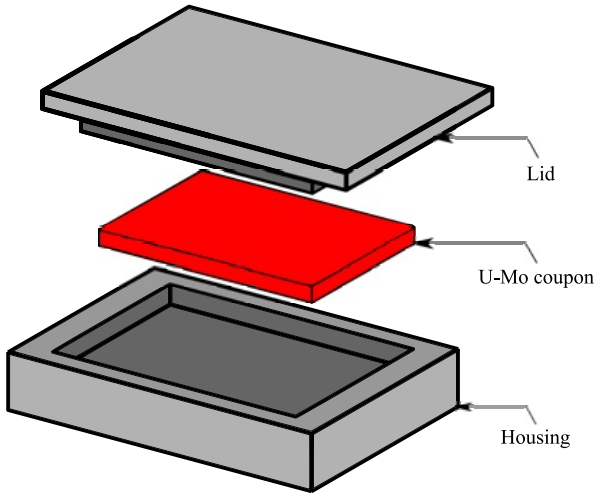

Figure 3.7: *Exploded view of assembly for U-10Mo bare foil manufacturing*

The material chosen for the canister is an **austenitic stainless steel** to reduce the price of consumables, as this part is removed after the process and keeps heat during hot rolling thanks to the austenitic structure. According to the manufacturing parameters chosen, the hypothesis of **identical deformation** between uranium and stainless steel is assumed here.

Regarding technology used for welding, the laser beam process is adequate to realise welding and to ensure good mechanical properties of weld for following manufacturing processes. Despite thermal and mechanical advantages compared to traditional welding processes, according to reports and articles, laser technology is not used to seal U-10Mo ingot into canisters. An understanding of stainless steel LBW is needed to prove feasibility and industrial usage to optimise the welding of the canisters.

Many experiments were done to highlight the feasibility of LBW, especially using diode and fibre lasers. Historically, diode laser was not considered to weld laser metallic parts due to a power and beam quality lack compared to CO_2 or fibre laser, which nowadays has been overcome by a technological jump. Experiments were realised to highlight parameter influence on stainless steel using laser technology in energy sectors or manufacturing. Different reports compare LBW to conventional processes to highlight laser performance for welding stainless steel parts. Elmesalamy et al. compared AISI 316L laser-welded and gas tungsten arc welding for multiple passes. Stress in the welded area is lower with better precision for multiple passes with laser compared to arc welding [88].

An optimisation of influent parameters, i.e., laser power, focal position, welding speed and gas pressure, is needed to obtain desired sets for welding and avoid defects such as inclusions, thermomechanical cracks, geometric defects, or fusion lacks. New parameters are needed to combine laser power and welding speed and understand their influences.

Suder and Williams highlight in their article that depth penetration is strongly linked to power density, i.e., heat input provided by the laser and a parameter called specific point energy, specific to the material to weld [81]. This parameter corresponds to a similar data to heat input, with the addition of beam diameter into the calculations. For the width of the weld bead, interaction time between the laser beam and surface should be a key parameter to obtain a width large enough to seal the ingot in a stainless steel canister and assure tightness [81]. According to studies on different stainless steel alloys [79, 89, 81], heat input between 30 and 50 $J \cdot mm^{-1}$, i.e., the ratio between laser power and welding speed, seems enough to achieve desired penetration depth of a few millimetres on a thin stainless steel plate. Heat input parameters give a relationship between power and speed, with a better influence analysis on depth penetration or width during the process. Critical parameters, welding speed and focal length mainly impact weld geometry.

Jiang and Zhang highlight in their study that the focal position of the diode laser beam is a crucial parameter for weld penetration, in addition to laser power and weld velocity imposed during the process [79, 90]. Microstructure is then locally modified by the laser. Microstructure kinetics of austenitic stainless steel leads to the formation of ferrite and pearlite according to the phase diagram and studies conducted on low carbon stainless steel, which could have an impact on thermal behaviour during the hot rolling step, and potential dissimilar properties between the weld area and the canister itself [91]. In addition, Yan et al. highlight changes in microstructure for welded parts, with dendritic structure along the weld bead [92]. Understanding this microstructure is significant to have desired global properties for the flat rolling process.

In conclusion, many reports and literature reviews bring numerous data about the welding of stainless steel by laser welding. These represent essential values to fit the process for requirement needed for both canister design and parameters combination for LBW.

Chapter 4

Laser beam welding process for canister sealing

After casting, the first step for the U-10Mo bare foil manufacturing process consists of encapsulating the ingot into the metallic canister. Laser beam welding technology is used to improve accuracy and optimise the process.

This section describes the process with LBW:

- **A description of the laser beam welding machine** with its characteristics in order to perform the welding of the assembly prior to the hot rolling process;
- **Laser beam schemes** used to ensure the mechanical link between the top lid and bottom housing of the assembly;
- **Setting-up of experiments conducted on laser beam welding**, with material and methods used, and numerical analysis used for weld bead geometry measurements.

4.1 Laser beam welding equipment

Laser beam welding technology was chosen as the manufacturing process for this stage of the U-10Mo bare foil manufacturing to ensure the ingot sealing into the metallic canister. Laser technology allows good accuracy thanks to a well-defined laser spot side and reduces operators' potential errors by automatised machine running, with a camera and vision system implemented. The machine implemented in the CERCA^{TM} laboratory is shown in Figure 4.1.

Figure 4.1: *Laser welding machine implemented in* CERCA^{TM} *laboratory*

Table 4.1 presents the experimental machine set-up parameter for welding. It sums up possible ranges of machine parameters such as laser power, laser speed and gas volume flow. The machine is fully configurable from an external computer, connected simultaneously to the laser beam machine and the laser source. A glazed door with protective laser standards protects operators.

Parameters	Minimum	Maximum
Laser power (W)	P_{min}	P_{max}
Welding speed ($mm \cdot min^{-1}$)	V_{min}	V_{max}
Gas volume flow ($L \cdot min^{-1}$)	Pr_{min}	Pr_{max}
Working distance (mm)	F_{min}	F_{max}

Table 4.1: *Parameters range of the laser beam welding machine*

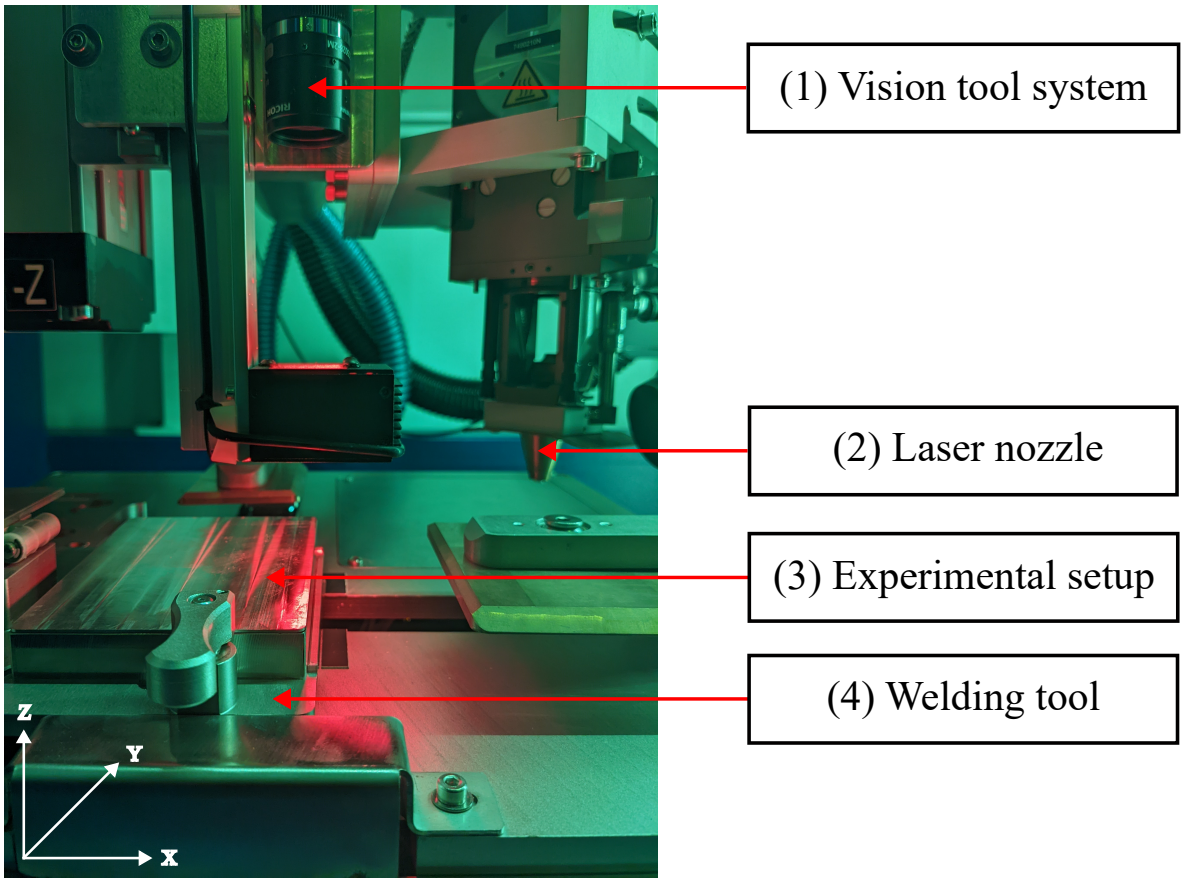

Figure 4.2: *Experimental device for laser beam welding*

The machine's interior and mechanical parts to perform laser welding are shown in Figure 4.2. The machine contains a moving table in X and Y direction and a motorised head in Z direction for the laser welding process. The laser head is composed of a nozzle to canalise the assisting shielding gas flow (Figure 4.2 - 2) and a vision tool to inspect weld beads after the welding process (Figure 4.2 - 1). A machined tool made with the canister geometry (Figure 4.2 - 4) is placed on the table to mount and maintain the canister. The mounted canister is welded on the concerned areas by coordinate positions for weld beginning. Then, the program interpolates the welding direction and makes appropriate corrections for welding length and angle of the welding according to the vision system.

4.2 Laser beam welding schemes

As shown in Figure 3.7, the lid is welded to the housing canister thanks to a mechanical link between the outer thin area of the lid and the corresponding base on the housing. Two types of welding were performed on canister samples to investigate this welding process, by adjusting the weld area and welding directions to assure the mechanical link between the lid and the housing. Due to confidential and sensitive data regarding the welding process, the weldings are pixelised on the following 4.3. The same procedure is applied for all welded assemblies in this report.

(a) First welding scheme (b) Second welding scheme

Figure 4.3: *Laser welding schemes used for canister sealing*

4.3 Material and methods

4.3.1 Experimental setup

Using a canister does not allow easy preparation for welding cross-sections, and support was developed because of the machining price. The experimental set-up consists of two assembled foils, and a metallic support is used. The top foil thickness is set to 1 mm to represent the thin lid part, and the bottom foil thickness is set to 2 mm to represent the housing. The support is designed according to the canister geometry set into the laser beam machine.

Four taps are manufactured in each corner to screw the assembly. Laser beam welding is then realised on the sample to weld them together: the top foil reproduces the canister lid, and the bottom foil reproduces the canister housing. The sample is screwed at every 4 corners to the support, designed according to canister geometry to fit with the existing welding tool to reduce bending due to thermal distortion.

Nuts are placed between the sample and the support before fixing them to physically separate both and avoid welding with the support thanks to laser defocus. As the laser program for canister welding is not optimised for welding line experiments, a dedicated program was developed for the laser welding machine. The program realises a succession of welding lines along the sample, as shown in Figure 4.4. All available welding experiment areas are used to maximise the weld bead number. Experimental lines are welded across the set-up with a 5 mm length distance between each to avoid thermal interaction for further analysis.

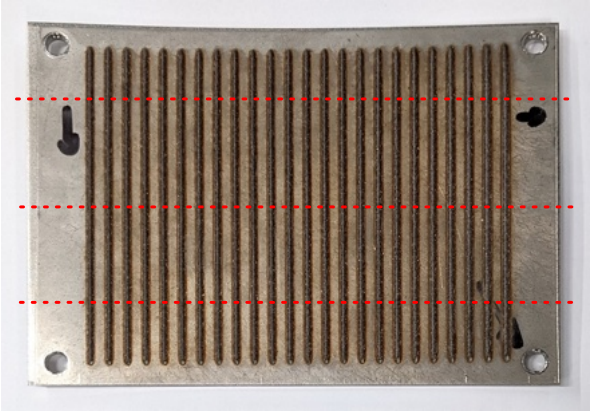

Figure 4.4: *Welded samples from top to bottom for cross-section examination Red dotted line: cross-section cutting for weld geometry measurements*

The laser welding sequence implemented is the following program:

1. Selecting starting point of the weld bead;
2. Choosing of parameters for weld bead: laser power and welding speed;
3. Welding of bead alongside the plate in width direction;
4. Moving to starting point and moving down by 5 mm to start the next welding line;
5. Repeating the steps 2 to 4 until the desired number of the weld bead is realised;

The sample is prepared for cross-section analysis on welding lines beginning, middle and end.

4.3.2 Sampling and numerical analysis for laser weld measurement

After welding of experimental lines with the desired set of power, speed and volume gas flow, foils are saw cut in order to exhibit cross-sections and to be analysed after etching under a microscope. The sample is cut according to the red dotted line from Figure 4.4 for further characterisation with a disk sawing machine in the transverse direction. Sample lengths are usually around 3 to 4 cm in height to put in two of them the same resin coating, saving raw material and polishing time. These cuts are then embedded and mechanically polished until the cross-section is shiny and chemically etched with an aqueous solution of HCl and $FeCl_3$ according to standard [93] to reveal a weld pool.

Chemical etching lasts 5 to 30 seconds, according to welding visual aspects obtained after mechanical polishing. Then, weld depth and width are measured according to Figure 4.5 to understand process parameters. A sample is considered welded when the melted area crosses the separation line between both stainless steel foils. The weld width measured corresponds to the width of the welded section on the separation line. The surface width on the top of the welding cross-section is irrelevant in this study as it is not responsible for the mechanical link of the lid to the housing canister.

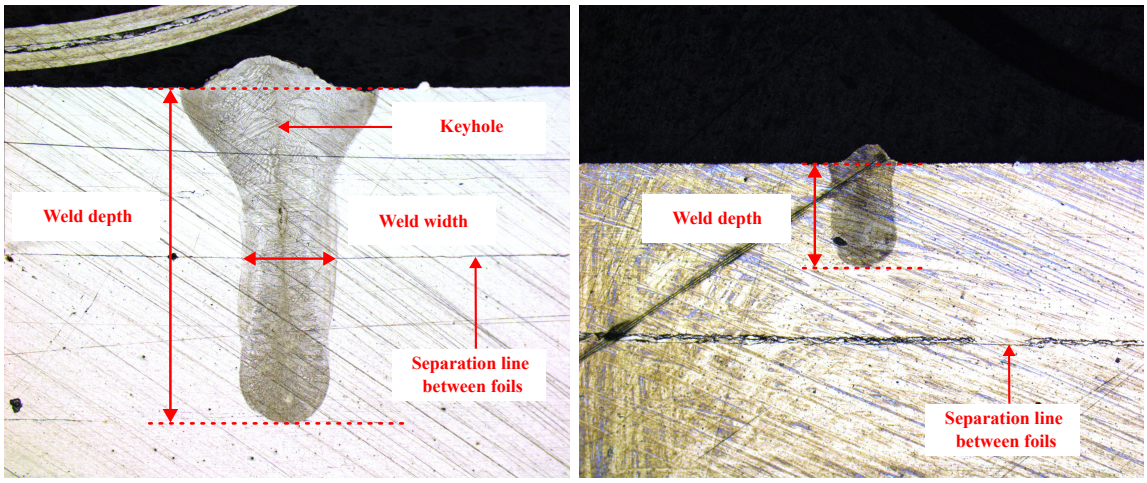

(a) Welded sample (b) Not welded sample

Figure 4.5: *Weld geometry measurement criteria for laser welding samples*

Chapter 5

Laser beam welding results

This section describes experiments conducted on the laser beam welding process to seal the casted U-10Mo ingot before the hot rolling process. Cross-section measurements from laser beads produced with material samples similar to the canisters used are performed. Then, measurements are plotted to highlight the influence of laser beam welding parameters on weld beads geometry.

Various experiments are performed for manufacturing parameters extraction:

- **Variation of laser power and welding speed separately** to understand their influence on the weld bead geometry;
- **Variation of power and speed with an identical heat quantity provided** to exhibit the main parameter between laser power and welding speed on weld bead geometry variations;
- **Laser beam welding on different materials with similar welding parameters** to highlight the influence of material properties on weld bead produced, being essential for canister material choice.

5.1 Laser welding parameters influence on weld geometry

5.1.1 Influence of laser power and welding speed

Influence of power

Experimental batch of laser welding beads is performed with **6 heat input** H_i values labelled from H_1 to H_6 in $J \cdot mm^{-1}$. The term *heat input* refers to the ratio between laser power provided and welding speed. H_1 corresponds to the lowest heat value and H_6 the highest. Laser power P_i for each line is labelled similarly from P_1 to P_6 in watt W. P_1 corresponds to the lowest power value and P_6 the highest. Then, the welding speed parameter is not modified for each line and is labelled as V_R as reference speed in $mm \cdot min^{-1}$. The laser source is configured in **continuous wave** with **no variation of working distance** between the focal length and the sample surface. Each line is reproduced twice for repeatability.

	Experiment sets					
Parameters	1	2	3	4	5	6
Heat input H_i $(J \cdot mm^{-1})$	H_1	H_2	H_3	H_4	H_5	H_6
Power P_i (W)	P_1	P_2	P_3	P_4	P_5	P_6
Welding speed V $(mm \cdot min^{-1})$	V_R					

Table 5.1: *Laser welding parameters for power variation on stainless steel*

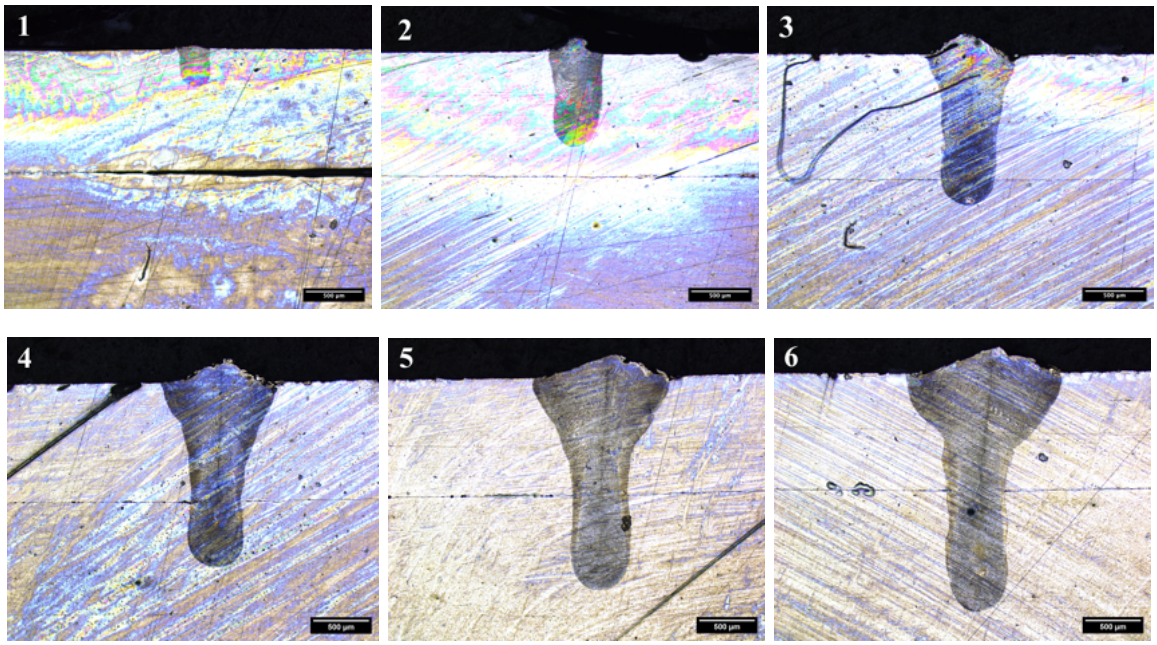

Figure 5.1: *Weld bead cross-sections with constant welding speed and power variation*

The cross-sections show clear evidence that for heat input and laser power equal or higher than H_3 and P_3, the LBW process succeeded in welding the foils together. The molten metal flow is not sufficiently deep to weld the two foils for lower heat input and laser power values. When the laser power is increased, the melt pool produced during the process grows in the depth direction. It enables a deeper penetration of the liquid. In addition, the molten pool head grows in volume for higher heat input and laser power values. For H_1 and H_2, the molten pool produced is not sufficiently deep to reach the transition line between both foils of the experimental assembly. A protuberance is also visible on the top of laser welds from H_2, with a size which increases with laser power. Microstructure is then slightly visible for welded samples. The typical pattern of liquid molten flow is visible with laser power values P_4, P_5 and P_6. Indeed, the liquid flow goes from the central keyhole produced by the laser in the middle of the weld and then goes on the left and right sides for cooling and producing this particular pattern.

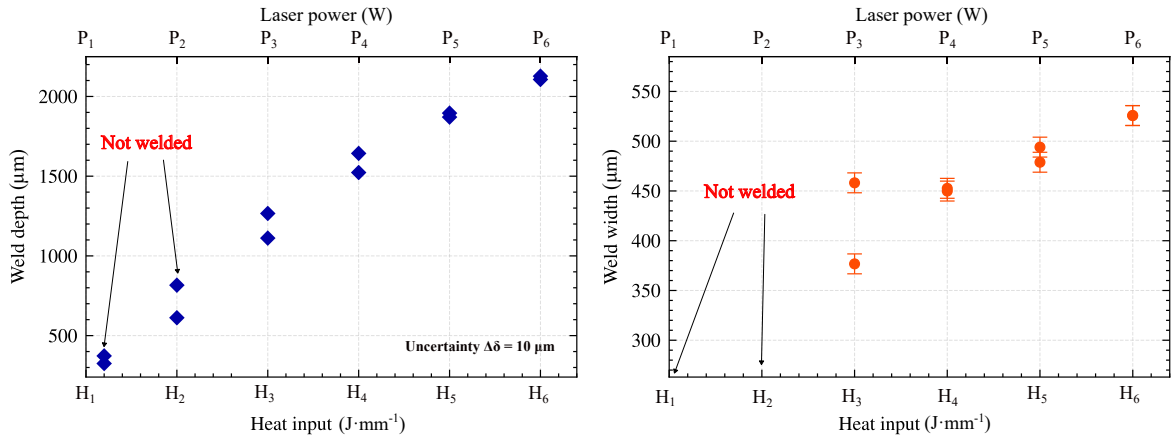

(a) Weld depth versus heat input provided

(b) Weld width versus heat input provided

Figure 5.2: *Measurement of laser weld bead geometries on stainless steel with power variation and constant welding speed*

The increase in weld depth occurs with successive increases in laser power values. Figure 5.2 - (a) illustrates this increase which follows a linear trend in a range of 300 to 2000 µm. The maximum value of weld depth achieved for H_6 is two times higher than the top foil thickness, which ensures the link between both foils. Also, the weld width is linearly increasing as a function of the laser power, similar to the weld depth increases. As a reminder, the width of the laser weld is the distance measured on the intersection of the weld bead and delimitation between the upper and the bottom foil of the sample. This part is momentous to ensure the link between the top lid and the bottom housing of the canister. Interestingly, the width's slope value is lower than the weld depth for a range of values from 400 to 520 µm.

Welding speed influence

This section of experiments concerns welding speed influence on laser welding beads. The same heat input variation as the previous experiment is performed with welding speed variation and constant laser power P_R, as summarised in Table 5.2.

	Experimental sets i					
Welding parameters	1	2	3	4	5	6
Heat input H_i $(J \cdot mm^{-1})$	H_1	H_2	H_3	H_4	H_5	H_6
Welding speed V_i $(mm \cdot min^{-1})$	V_1	V_2	V_3	V_4	V_5	V_6
Laser power (W)	P_R					

Table 5.2: *Laser welding parameters for welding speed variation*

V_1 corresponds to the highest welding speed value and V_6 the lowest. To assess measurements, twice repeated welding is used, except for the H_3 experiment due to an issue during sample preparation. Cross-section examinations are performed on laser beads to measure weld depth and width according to section 4.3.2. Microscopic pictures of cross-sections are shown in Figure 5.3 with measurement plots in Figure 5.4.

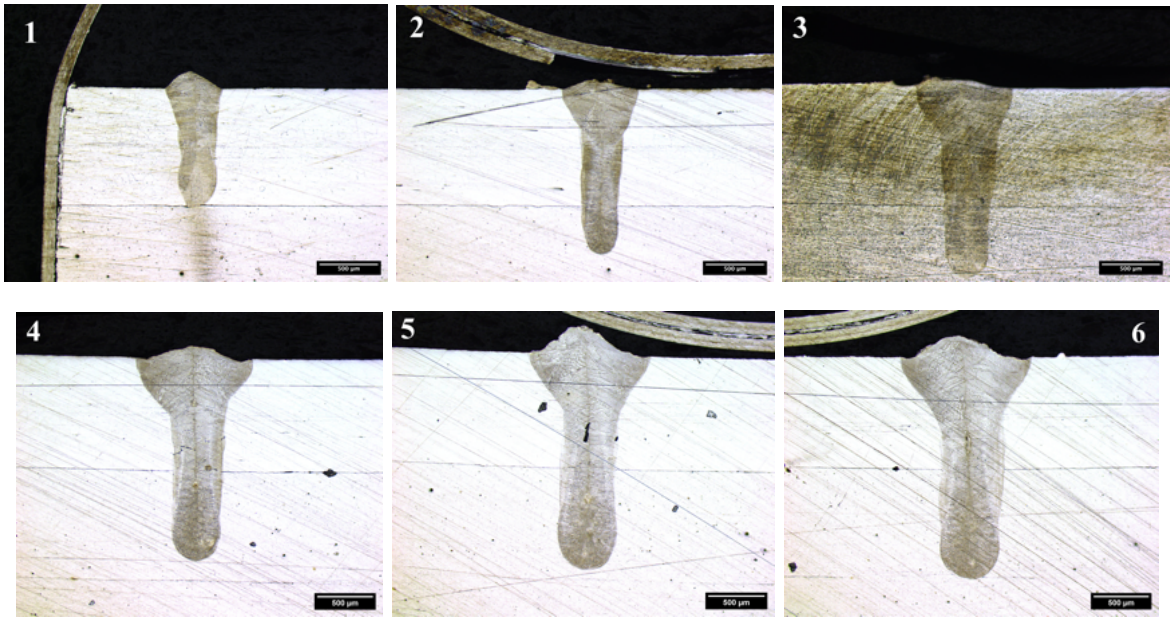

Figure 5.3: *Weld bead cross-sections with constant power and welding speed variation*

For a variation in welding speed, the minimal heat input needed to weld the two foils together differs from the laser power variation experiment. Welding is achieved for heat input equal to or higher than H_2 and V_2 welding speed value. Compared with the previous experiment for H_1, weld depth is closer to the transition between the upper and the bottom foil. Interestingly, there are also differences in the molten pool fusion head ratios. They are visible for all experimental sets and seem to keep a similar volume for samples with welding speed values V_4, V_5 and V_6. In addition, the molten pool fusion heads appear larger for these three last welding speed values. A protuberance is also visible on the top of the weld, similar to laser power variation. This artefact size is increasing while heat input is increasing too. Finally, as observed with laser power variation, a similar microstructure for solidifying the liquid flow is visible in these samples.

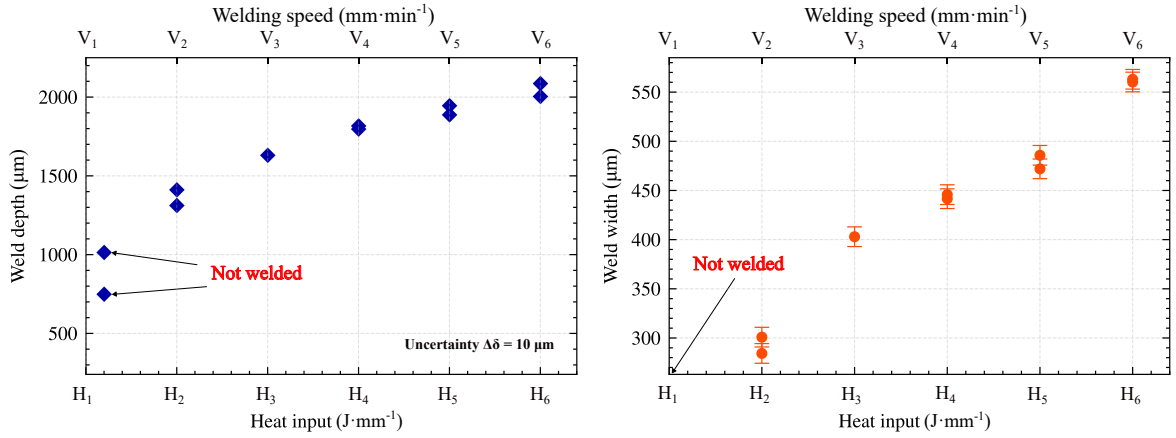

(a) Weld depth versus heat input provided

(b) Weld width versus heat input provided

Figure 5.4: *Measurement of laser welding geometries on stainless steel with speed variation and constant laser power*

As seen from Figure 5.4, successive decreases in welding speed, and consequence increases in heat input, increases weld depth and width values. Both curves follow a linear trend similar to laser power variation plots, ranging from 750 to 2000 µm for weld depth and 300 to nearly 600 µm for weld width. The weld depth curve has a higher slope value than the weld width curve. Furthermore, the slope value of weld width with welding speed variation looks higher than for laser power variation.

Comparison for identical heat input and different parameter set for laser welding

This section of experimental tests concerns both variations of welding speed and laser power with the same heat input applied. The welding batch is performed according to Table 5.3 to compare differences between different combinations of laser welding parameters.

	Experimental sets i							
Welding parameters	A	B	C	D	E	F	G	H
Laser power P_i (W)	P_A	P_B	P_C	P_D	P_E	P_F	P_G	P_H
Welding speed V_i $(mm \cdot min^{-1})$	V_A	V_B	V_C	V_D	V_E	V_F	V_G	V_H
Heat input H $(J \cdot mm^{-1})$	H_R							

Table 5.3: *Laser welding parameters with constant heat input for stainless steel sample*

The laser source is configured in continuous wave mode with identical working distance. Figure 5.5 shows cross-sections, with measurement heatmaps on Figure 5.6.

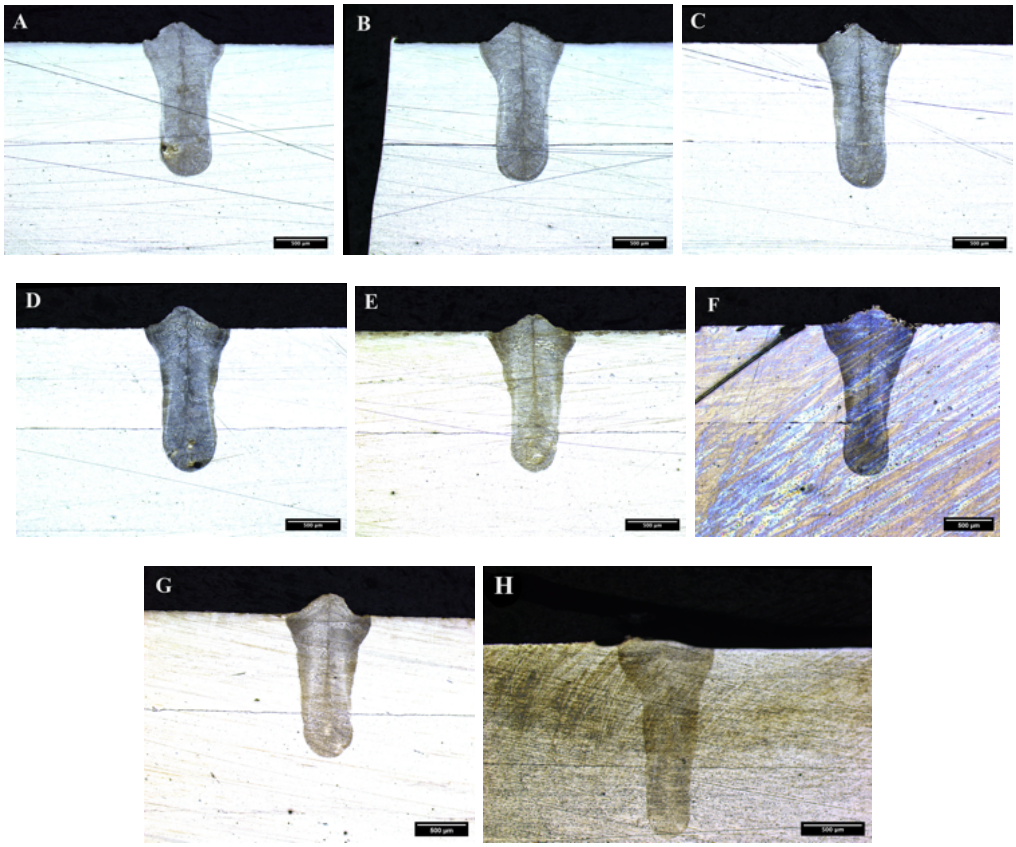

Figure 5.5: *Weld cross-sections for constant heat input with power and speed variation*

First, as shown in Figure 5.5, the results indicate that each welding line achieves the welding of sample foils together. As seen from previous experiments, the morphology and geometry of cross-sections look similar and typical for laser beam welding. The correlation between welding geometry and the parameters set is interesting because cross-section pictures do not give, as in the previous experiments, a striking trend of weld depth and width for samples investigated. Combining laser power with welding speed variation for the same heat input did not produce visible melt pool geometry changes.

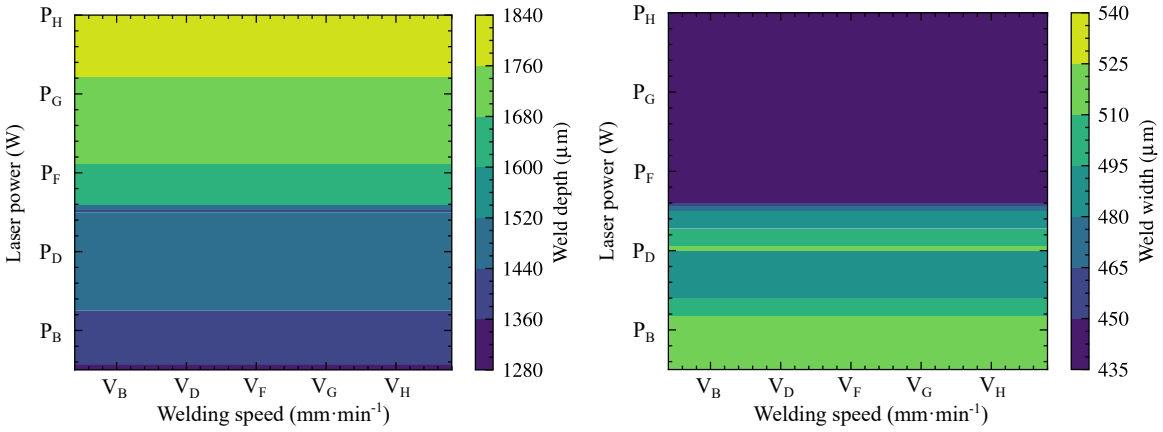

(a) Weld depth heatmap

(b) Weld width heatmap

Figure 5.6: *Measurement of laser welding geometries on stainless steel for constant heat input with laser power and speed variation*

In order to have a better view of weld geometries, Figure 5.6 - (a) and Figure 5.6 - (b) provide respectively heatmaps for both weld depth and weld width measured. For the weld depth heatmap, values follow mostly laser power values used in ascending order with laser power increasing. For the same welding speed, the laser power will affect the penetration depth of the weld produced: a high laser power value leads to a high weld depth. Every laser power stage increases weld depth on average by 90 µm, except for a laser power value on the transition around P_F, where the transition between two level colours is lower than others.

Then, the results plot has more variation for the weld width heatmap. Weld width is highly variable between P_B and before transition at P_F. Width value drops from high width values to lower values until P_F, then decline again to be at the lowest value of laser power value until P_H. High power tends to reduce the weld width obtained for any of the welding speeds selected during the process. Nevertheless, welding speed substantially influences weld width more than weld depth, where the laser power is the main factor, with some variability for lower laser power values.

5.1.2 Comparison between stainless steel and nickel alloy material

The last part of the laser welding section focuses on the difference between two metallic alloys: stainless steel and nickel alloy. Welding speed and laser power values have been varied in the same way as in previous experiments. Four heat input values were selected for these samples, from H_3 to H_6, where H_3 corresponds to the lowest heat input, and H_6 the highest. Figure 5.8 and 5.7 respectively expose cross-sections of both materials for each heat input applied, with plots of weld depth and width measured. The nickel alloy cross-sections were etched according to NF EN ISO 17639 standards [93].

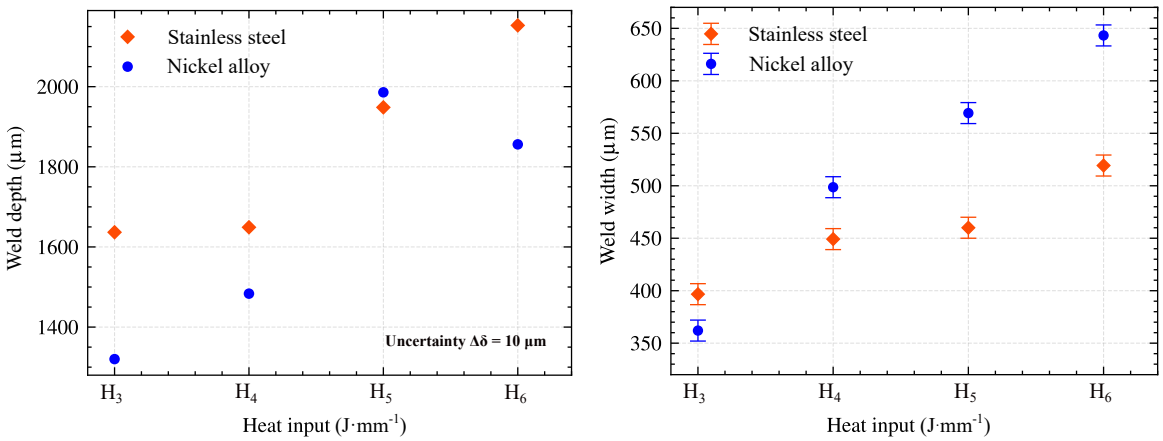

(a) Weld depth versus heat input provided

(b) Weld width versus heat input provided

Figure 5.7: *Plot of weld depth and width for stainless steel and nickel alloy*

The global geometry of the cross-section is close to the ones obtained before. The same heat input as stainless steel welded the nickel alloy samples. However, significant differences have been found, including the melting pool microstructure and the top weld cavity. The extending in both left and right directions from the central keyhole is shown in Figure 5.8. The nickel alloy microstructure is more lamellar from centre to right and left sides, which argues for a preferential direction for microstructure solidification. Regarding the weld depth plot in Figure 5.7 - (a), the value measured differs between both materials. Stainless steel weld depth is slightly deeper than nickel alloy for the same heat input. A higher heat value is needed to weld deeper in nickel alloy than stainless steel. Figure 5.7 - (b) highlights the weld width linear growth with heat input increase. The weld width of nickel alloy samples for the same heat input applied is lower compared to stainless steel on average of 50 µm for H_3 and H_4, and twice for H_5 and H_6. The exception is for H_3, where the width for stainless steel is higher than the nickel alloy. The data's most surprising aspect is that the width is higher for the nickel alloy, in contrast to the weld depth. This phenomenon could be explained by differential heat diffusion through the weld, with the preferential melting pool microstructure.

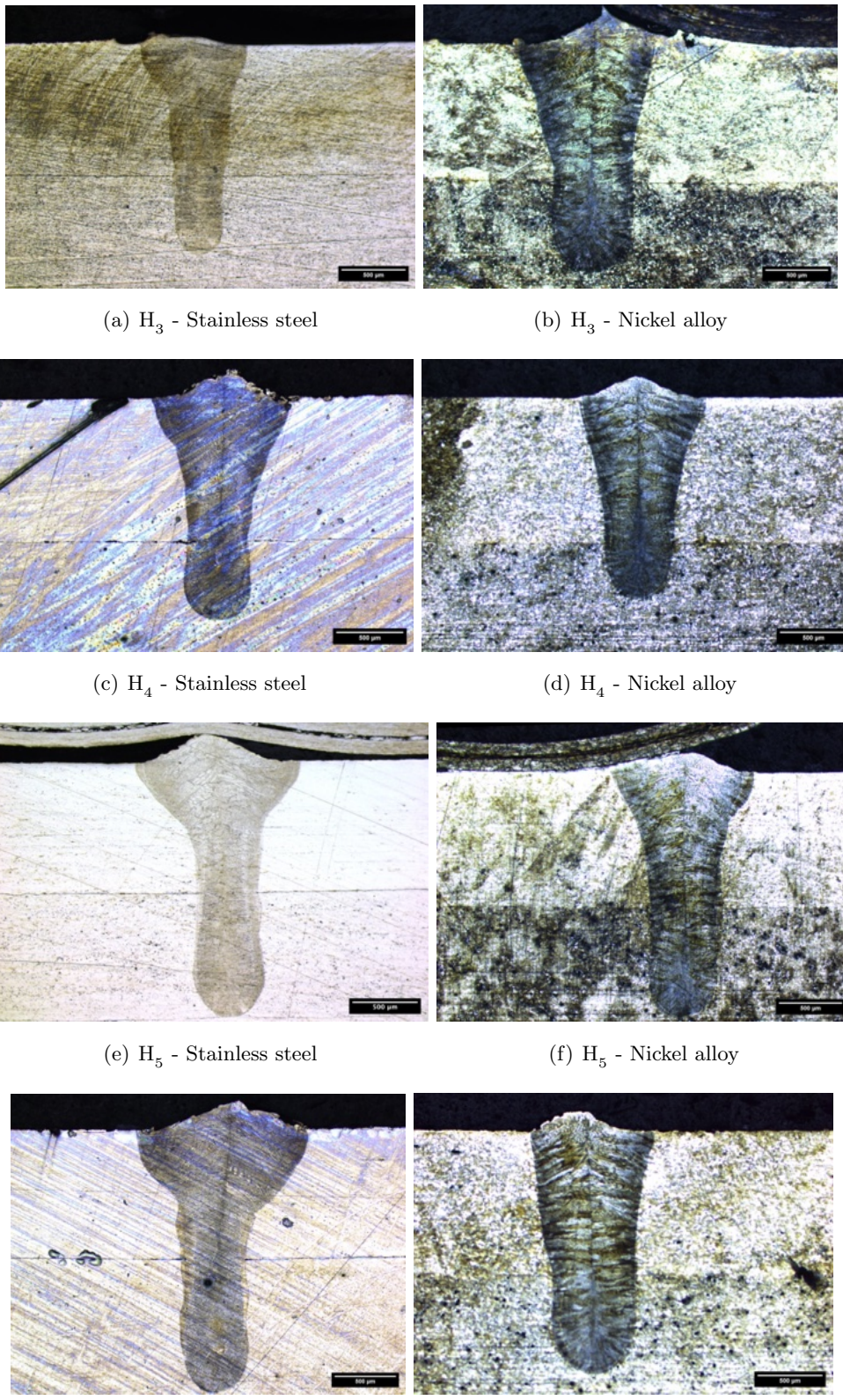

(a) H_3 - Stainless steel

(b) H_3 - Nickel alloy

(c) H_4 - Stainless steel

(d) H_4 - Nickel alloy

(e) H_5 - Stainless steel

(f) H_5 - Nickel alloy

(g) H_6 - Stainless steel

(h) H_6 - Nickel alloy

Figure 5.8: *Welding samples comparison between stainless steel and nickel alloy*

5.2 Discussion and summary

The choice of the parameters for canister welding, in addition to the material used for canister manufacturing, represent essential aspects of U-10Mo bare foil manufacturing to achieve the entire process, from mechanical tenacity to tightness of the assembly and for future substeps of hot rolling and laser cutting.

Laser power is the main factor in varying weld depth and width. A higher power value leads to higher values in both directions and increases mechanical strength by increasing the surface size between the lid and the canister. Nevertheless, a too-high-power value is not recommended to avoid the lid's bending and crack initiation during the hot rolling, as the molten pool provided by the process can be vaporised at high temperatures. This vaporisation initiates defects and cracks for future manufacturing substeps by removing the molten liquid required to link the two metallic parts. Welding speed is a secondary factor for LBW but could be used to reduce the heat input provided and optimise weld geometry, especially the weld width. The welding speed will influence the exposure time between the laser and the part, and heat exchange is modified. Then, reducing heat input also reduces the potential thermal deformation of foils. As the assembly manufactured in this substep of U-10Mo bare foil manufacturing does not represent the final step, weld appearance is not representative of the success of the process, and parameters are not chosen according to these criteria. The priority in the welding process is to have a high mechanical strength between the lid and the housing, achieved by optimisation of laser power and welding speed parameters.

The influence of other parameters, such as reflectivity, laser beam wavelength, and continuous or pulsed waves, on this welding process was not studied. However, they represent the experimental path to improve the process and industrial production. This process for the U-10Mo bare foil manufacturing line is promising thanks to its high accuracy and repeatability. LBW represents a breakthrough technology for fuel manufacturing as it is used for the structural part but not for fuel manufacturing. LBW has important advantages compared to standard sealing by welding the edge between two plates and a windows frame by TIG welding, as realised in the US development. Compared to LBW, more heat is provided to the part with the TIG welding process. Automation of the welding process is feasible for laser beam welding by programming a specific scheme according to the canister used. Finally, the choice of laser welding scheme would impact the mechanical behaviour of the assembly according to the hot rolling scheme chosen for different types of material.

Part III

— Laser beam cutting process of rolled U-10Mo alloy —

To increase the cutting accuracy and the global quality of the U-10Mo monolithic bare foils after the hot rolling process, Framatome-CERCA^{TM} and the FRM II have developed a process which involves laser technology: Laser Beam Cutting (LBC). This process consists of cutting by laser a wide range of materials, including multi-layer materials. For this manufacturing line, these composite materials can be U-10Mo foils coated with Zr, U-10Mo foils encapsulated into stainless steel cladding from the hot rolling process or a finalised fuel plate with the coated U-10Mo foil and the aluminium cladding. Using LBC for nuclear material also represents a breakthrough technology. Understanding this process is essential to prove the feasibility for industrial uses and improve the global quality of U-10Mo bare foils. This part does not investigate the laser theory as it is shared with LBW and reviewed in chapter 3.1.

This part is structured as follows:

- **A literature review of the laser technology application for metallic material cutting** and different purposes for nuclear materials;
- **Description of material and machines used for LBC for this work**, with the range of parameters used and experimental set-up for the experiments performed;
- **LBC results from various experiments on both inert materials and U-10Mo bare foils**, studied to highlight the parameter set influence on foil samples regarding the local microstructure, the visual aspect and the geometry of cutting produced.

Chapter 6

State of the art of laser beam cutting

6.1 Theory about laser beam cutting

Laser **B**eam **C**utting (LBC) is widely used in industry to obtain specific geometries with high precision. Many articles and reviews highlight laser cutting for metallic and plastic materials with different scopes: industrial production feasibility, parameter influence, and process optimisation. LBC advantages instead of the conventional cutting processes are multiple: edge quality and precision, workpiece and machine contactlessness, high level of automation, and fewer consumables needed. This process has been used in many sectors and appears to have widely been used for many years [94, 95, 96]. As LBW, LBC is a machining process using laser power to cut metallic and non-metallic parts. It allows better cutting precision thanks to laser spot diameter to affect a local area of the material. Process parameters such as laser power, cutting speed, pulse duration, and laser frequency, as well as assisting gas pressure, are parameters to take into consideration for laser cutting, especially for kerf width in entry and exit obtained [95, 96]. Figure 6.1 shows the LBC scheme with foil cutting and kerf obtained. During LBC, the laser pass entirely through the sample to be cut. The material located beneath the area affected by the moving laser melts entirely until all the volume in the thickness direction is melted with appropriate laser parameters. All the molten pool is ejected by assisting gas pressure during the process. The cut obtained is called a kerf, which is usually in a V-shape, with kerf entry wider than kerf exit due to the Gaussian beam shape of the laser. The workpiece is mainly affected by laser thermal stresses, which can affect the part with surface roughness modification, local microstructure changes, the flatness of cut sample, burns, and thermal stresses [95].

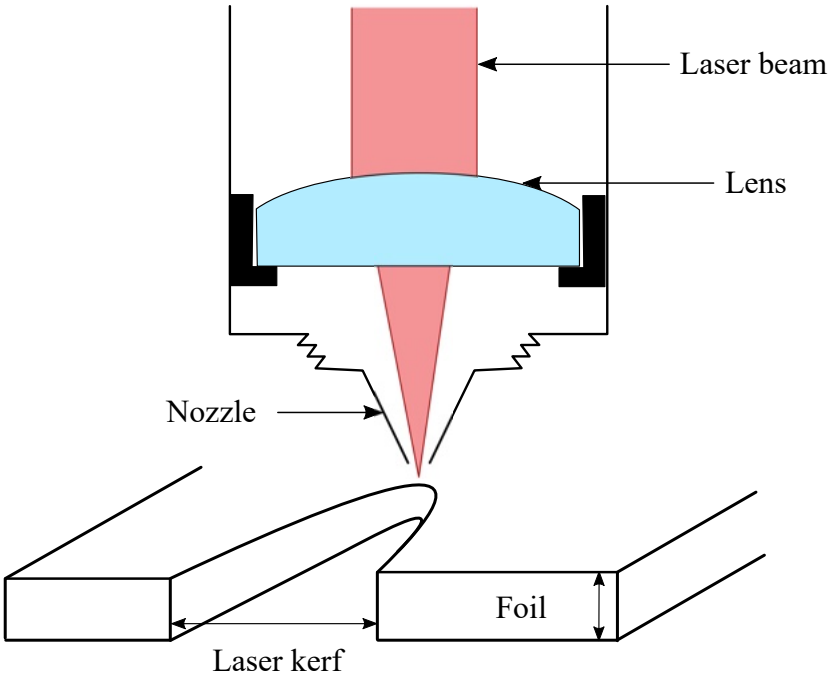

Figure 6.1: *Laser beam cutting scheme adapted from [78]*

Kerf width in entry and exit of the part are critical parameters for LBC to understand how entry variables influence the process. Low specific heat combined with high thermal conductivity leads to higher kerf width. The local hardness of the foil is also affected, particularly with O_2 gas uses, which leads to oxide formation, which is harder than the initial material [78]. As said before, the heat-affected zone (HAZ) affects the part by locally remelted area and alters the local microstructure. It increases with the power laser and decreases with the cutting speed. Sheng et al. emphasise that a higher power laser increase HAZ during laser cutting then decreases with a higher cutting speed [95]. Cut edge squareness, kerf slide slopes, and liquid ligament art he kerf exit from LBC, called dross, also represent exit variables to consider for cut quality [96].

The dross formation from laser cutting requires a comprehensive examination to be understood and avoided, especially for this work's final product, as U-Mo bare foil. The term dross for LBC concerns ligaments or particles from molten liquid created during the process, which were not ejected by the assisting gas jet pressure. The formation of dross is due to the formation of a liquid layer in the thickness direction during laser cutting. A part of this film is ejected by the gas used, and when all the liquid is not expulsed, a part stays on the kerf exit, solidifies, and generates drosses on the cut foil. Figure 6.2 depicts their formation during LBC.

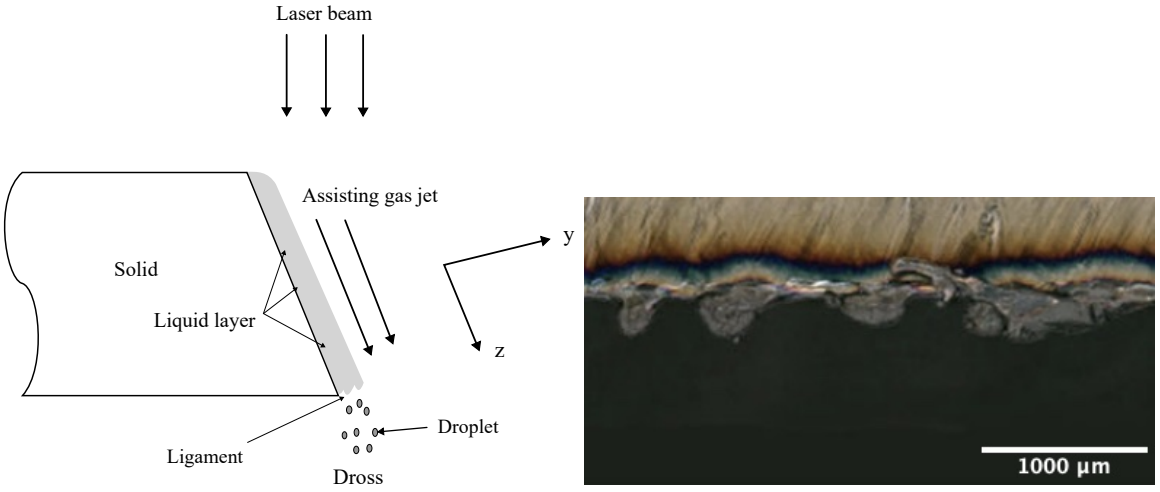

(a) Dross formation mechanisms [97] (b) Dross from stainless steel sample [98]

Figure 6.2: *Kerf dross appearing during and after LBC*

Caristan et al. highlight that assisting gas jet pressure and the focal length affect dross generation [78]. Yilbas et al. highlight the importance, in the best situation, of having the smallest volume of the liquid layer during the laser cutting process with an adequate gas pressure to eject the molten pool produced and avoiding dross appearance [97]. One solution would be to increase the laser beam's energy density to keep the liquid layer as long as possible and to eject it with the assisting gas pressure.

LBC shares the same critical parameters with LBW: heat input provided to the material, laser characteristics, inert gas flow, and focal length. However, different issues and defects are affecting the LBC process and the cutting quality and the final foil: local microstructure changes, surface roughness involved, and aerosols composition induced by the liquid vaporisation. Understanding these parameters is essential to ensure the requirement for U-10Mo bare foil production.

6.2 Laser beam cutting of metallic materials and uranium

Laser technology is not widely used in the nuclear sector to cut uranium. Studies about uranium laser cutting are difficult to find, especially for U-Mo alloy. They mainly concern uranium pellets or nuclear waste [99, 100].

Regarding metallic material, laser cutting technology is used to cut ferrous materials such as nickel alloys or stainless steel [101, 102] and non-ferrous materials, such as titanium [101], molybdenum, or aluminium [103, 104]. Yilbas et al. investigated thermal efficiency for mild steel to get an optimised kerf after laser cutting. Interestingly, changes in gas composition affect chemical changes of mild steel cut [97]. Ghany et al. highlight the impact of assisting gas pressure on kerfs measured: high gas pressure would lead to higher width and roughness of the kerf produced on austenitic stainless steel of 1 mm thick. In addition, higher-speed experiments conclude that high cutting speed leads to lower kerf width [105].

Regarding U-10Mo bare foil manufacturing, the composite structure has to be cut with U-10Mo and Zr coating and U-10Mo and the metallic canister after the hot rolling step. Irradiated and fresh fuels are available for laser cutting, in theory. With a high amount of energy provided in a local area, reaching a temperature to melt the material and cut it is possible. Chang et al. successfully cut stainless steel cladding uranium UO_2 pellets with a melting point of 2800 °C [99]. The thickness of uranium samples cut is 20 mm for rod diameter. In addition, fuel debris simulated by the CEA highlights laser cutting process feasibility for the nuclear sector. Dazon et al. simulated the cut of nuclear debris from the Fukushima incident with similar material, with the same properties as uranium and irradiated UO_2 pellets, especially about thermal conductivity and latent heat [106]. These studies highlight the capacity of using laser tools in a radiative environment. Laser beam polarisation influences sidewalls and geometry of cut parts with privileged orientations of local structure. This geometry represents essential data for the finished products [103].

Finally, another aspect of laser cutting is the microstructural modification of uranium with cavities and phase changes. Micro-pores, fragments, crispness phenomena, and caves are present on the cutting edges of pellets due to thermal expansion and assisted gas pressure used [99]. Higher energy input involves a higher temperature, so a modification of the uranium structure in affected volumes. In addition, using of O_2 gas for laser cutting modifies existing uranium. The second is responsible for aerosol production. Knowledge about the source and composition of aerosols after laser machining is needed for safety and security reasons. Uranium and molybdenum particles in filters with specific sizes must be registered to list inventory and the weight of uranium losses during the process. Cabanillas and al. used laser cutting to validate the feasibility of laser cutting in the nuclear sector for U-Mo by cutting 1010 steel. Particles mainly present after the cutting measure around 104 µm, which is suitable as particle size for manufacturing processes involving powder [107].

Chapter 7

Laser beam cutting process of rolled samples

The last manufacturing step for bare uranium-molybdenum foils involves removing the foil from the metallic canister after the hot rolling process. The U-10Mo bare foil must be resized to match the required geometry for the PVD coating and aluminium cladding process. Laser cutting is preferred instead of conventional shearing tools to improve cutting accuracy.

This chapter describes the process using laser beam cutting:

- **A description of the laser beam cutting machine** with its characteristics in order to extract the U-10Mo bare foil with required tolerances;
- **Laser beam cutting schemes** used for foil removing and resizing for further manufacturing substeps;
- **Setting-up of laser beam cutting experiments**, and the numerical analysis performed for kerf geometry measurements and methods for the hardness measurement conducted;

7.1 Laser beam cutting equipment

The machine set-up for cutting is composed of a laser cutting machine implemented in a controlled atmosphere glovebox for the operator's safety and to preserve the atmosphere quality during the preparation. Table 7.1 sums up the possible range for machine parameters.

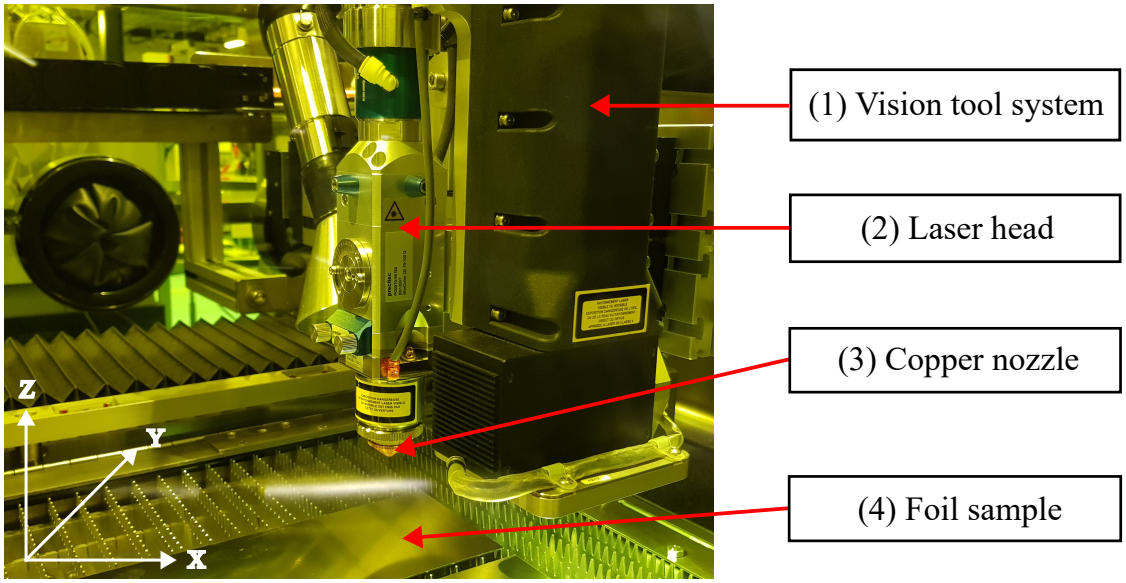

Figure 7.1: *Experimental setup in the laser cutting machine*

Parameters	Minimum	Maximum
Laser power (W)	P_{min}	P_{max}
Cutting speed ($mm \cdot min^{-1}$)	V_{min}	V_{max}
Assisting gas pressure (bar)	PR_{min}	PR_{max}
Working distance (mm)	F_{min}	F_{max}

Table 7.1: *Parameters range for the laser cutting machine*

The laser machine consists of an immovable table with jagged supports and a motorised head for laser movement (Figure 7.1 - 2). The laser head is composed of a nozzle (Figure 7.1 - 3) to canalise an assisting gas flow and a vision tool (Figure 7.1 - 1) to prepare the cutting and to inspect kerfs during the process (Figure 7.1 - 4). In addition, an inductive system is implemented in the nozzle to calibrate the z-axis with the sample before the cutting process. An example of a cut assembly after the hot rolling process is shown in Figure 7.2 with the extracted U-10Mo bare foil in the middle, separated from the canister with the lid and the housing, respectively, on the top and the bottom of the U-10Mo bare foil.

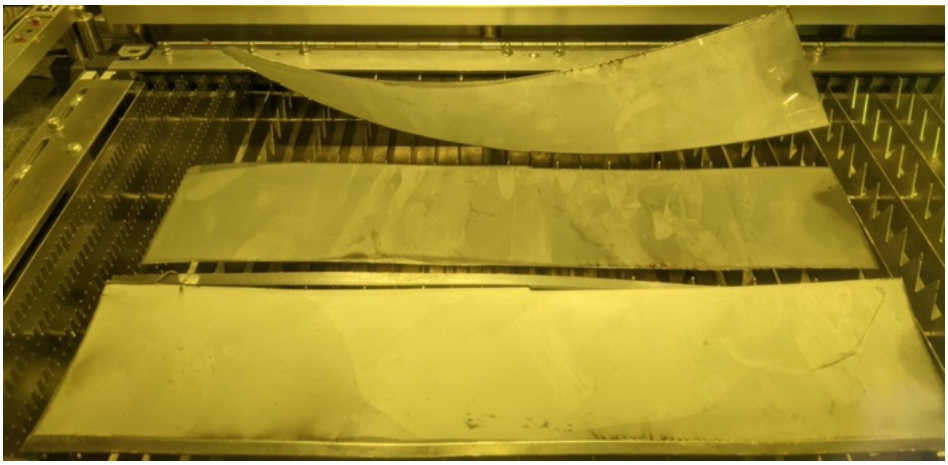

Figure 7.2: *U-10Mo assembly removed from the metallic canister in laser cutting machine Top: Lid - Middle: U-10Mo bare foil - Bottom: Housing*

The U-10Mo bare foil is then resized to the desired geometry, and the canister's top and bottom cover are also cut for further retreatment and analysis if needed.

7.2 Laser beam cutting scheme

After cutting the different edges of the metallic canister, the U-10Mo bare foil is removed and resized according to Figure for PVD coating.

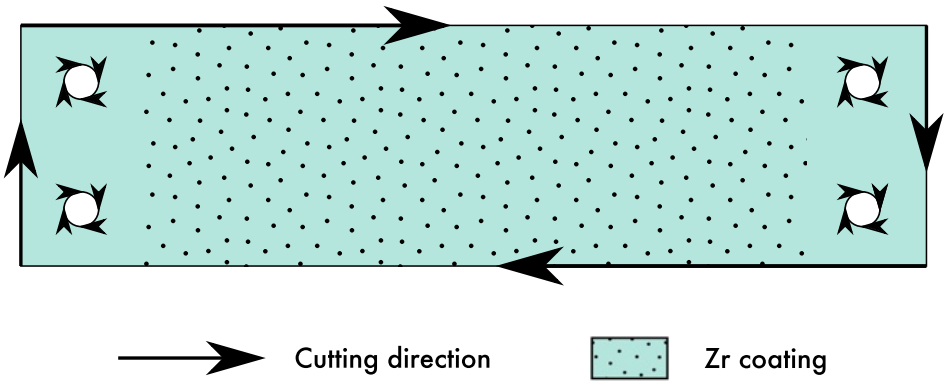

Figure 7.3: *Laser cutting scheme of U-10Mo bare foil prior to PVD*

The black arrows above indicate the cutting scheme and nozzle direction. Four holes are laser cut on each edge to maintain the bare foil during the PVD coating.

7.3 Material & methods

7.3.1 Experimental setup

U-10Mo bare foil scraps with thicknesses varying from 0.4 to 0.3 mm have been used for laser cutting experiments. The set-up comprises the sample set on the supporting table (Figure 7.1 - 4). Similarly to welding scheme experiments, cutting lines are realised as illustrated in Figure 7.4. Cutting lines produced are separated by a distance of 5 mm to ensure thermal diffusion of the laser for each kerf. The inductive sensor maintains the same working distance for each cutting line. The kerf width is measured with a light microscope.

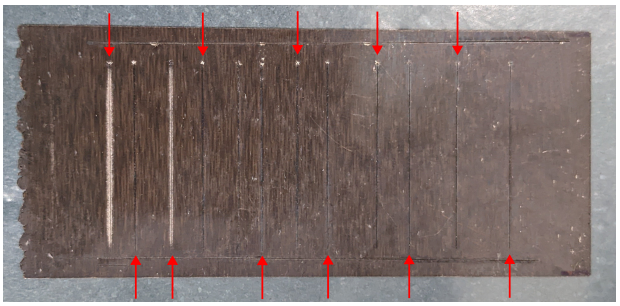

Figure 7.4: *Laser cutting experiment on U-10Mo sample - Red arrows: Kerfs produced*

7.3.2 Sampling & preparation

After the laser cutting line experiment, the foil is resized to analyse it under an optical microscope. The sample size for analysis is a square of 200 x 200 mm^2. When the sample is smaller than the U-10Mo bare foil from Figure 7.4, it is analysed without resizing. No etching is done on the kerf produced, and different luminosity and contrast on the microscope are performed to exhibit the best picture for kerf measurements. Figure 7.5 shows an example of microscopic kerf pictures with uncut and cut samples. The kerf is then measured in three areas to obtain an overview of width: at the beginning, middle and end of the kerf produced.

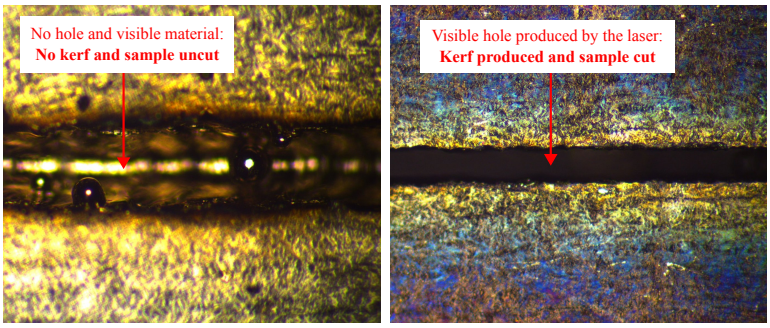

(a) Uncut sample (b) Cut sample

Figure 7.5: *Kerf observation under an optical microscope with cut and uncut samples*

7.3.3 Numerical analysis for laser kerf measurements

Laser-cutting kerfs are usually difficult to measure with high accuracy. Conventional tools and physical instruments typically can not be used for a measurement accuracy of a few microns. A numerical tool with image processing and automatic kerf detection on microscope pictures has been developed via a Python program to improve measurement, as shown in Figure 7.6.

The principle is the following:

1. Having optimal focal length for both sides of the kerf with the microscope in order to capture the most detailed picture;
2. Processing the picture to have it as straight as possible;
3. Separating the kerf from the rest of the foil by using threshold values;
4. Obtaining pixels of separation between the foil and the kerf on both sides;
5. Measuring the distance between both pixels to obtain the kerf size.

Data of pixel and kerf length measurement are given by a Python code which treats the data file containing all the information about the pixel value extracted from the picture. It returns the first pixel on the top and the first pixel on the bottom of the kerf (Figure 7.6). The difference between both then gives the kerf width. A series of values are taken for a defined pixel interval in the cutting direction along the kerf to ensure repeatability of the kerf width. It also returns the maximum and minimum value, uncertainty and length measured.

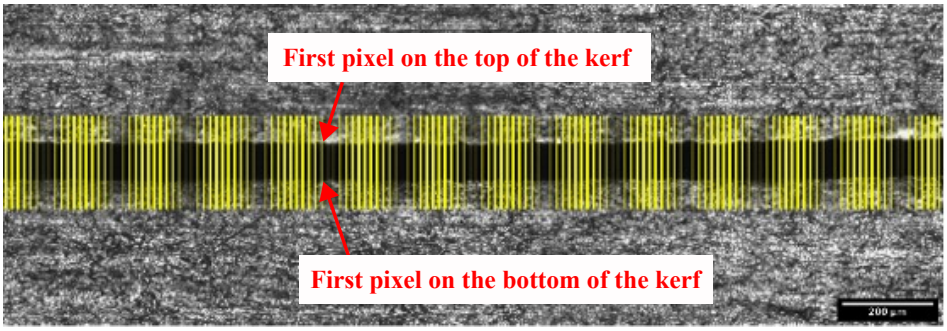

Figure 7.6: *Mapping of numerical measurements for laser kerf. Each yellow line is equidistant from each to obtain an appropriate distribution of kerf measurements.*

This technique gives an accuracy depending on the lens chosen during the picture taking and the threshold technique used for the picture. Results quality also depends on the colour and light balance used during image capture, which can conduct potential bias from image processing. After image treatment and numerical measurement, kerf values are summarised, including mean value, kerf extremum, total length measured, and uncertainties.

The kerf measurement is performed on three areas to obtain representative kerf values and increase accuracy. The alongside kerf measurement is essential to ensure good parallel parts, tolerances on desired parts and kerf width repeatability for future manufacturing processes.

7.4 Hardness measurements of cut edges

Hardness measurements at the kerf entry were performed in the same way as U-10Mo bare foil measurements described in section 10.4 with particular attention to exhibit potential HAZ induced from heat provided by the laser. Figure 7.7 highlights a laser cutting kerf and hardness marks performed according to specific mapping from the kerf to the rest of the foil. Mark pattern is chosen with a regular distance between each mark of 30 µm. The first mark is performed at a distance of 45 µm from the kerf edge to avoid a misconducting of penetrator between the kerf and the foil sample. Then, the foil sample is set as flat as possible on a thick support to avoid any movement during the hardness measurement.

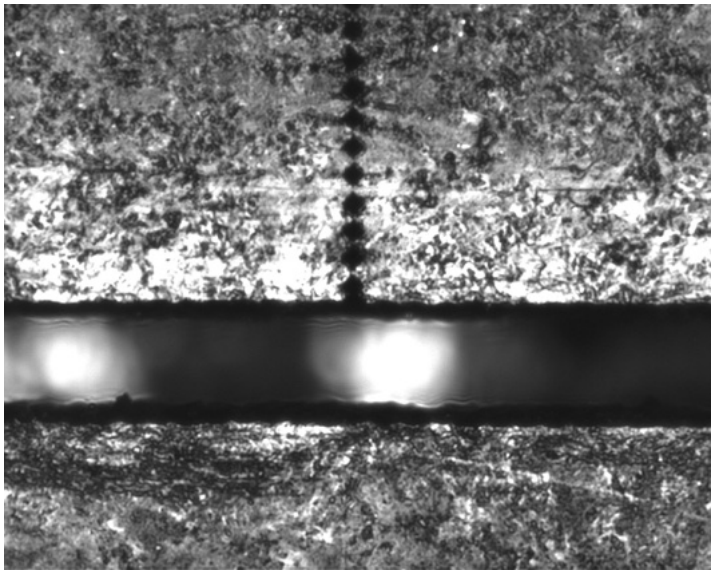

Figure 7.7: *Mapping of hardness measurements on laser cutting edges of U-10Mo sample*

As the samples were not polished before the hardness measurements, three numerical treatments on pictures were realised, as shown in Figure 7.8. ImageJ software performs these different numerical analyses and measures each diagonal with an appropriate scale. Measurements are then used for Vickers hardness calculation and uncertainties with Equation 10.2.

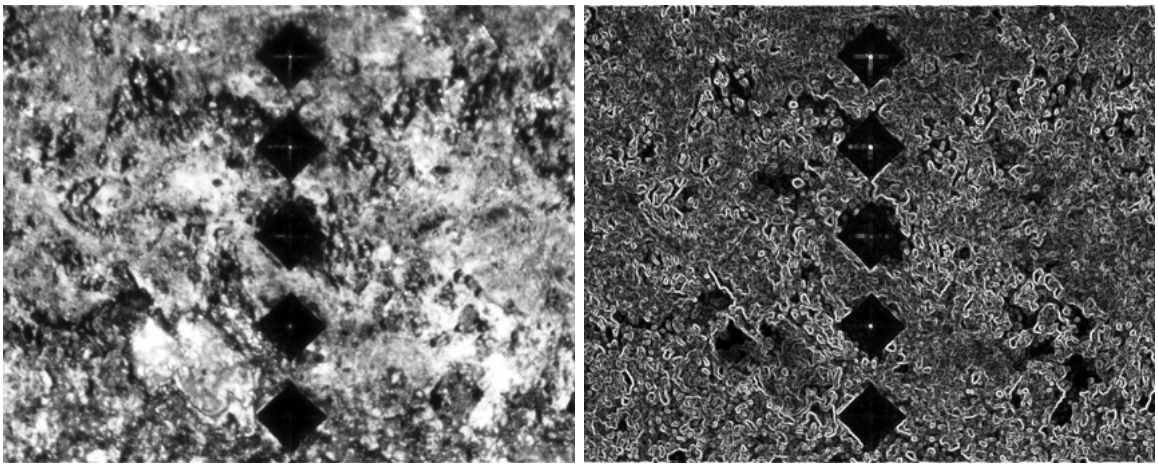

(a) Contrast enhanced (b) Edge detection

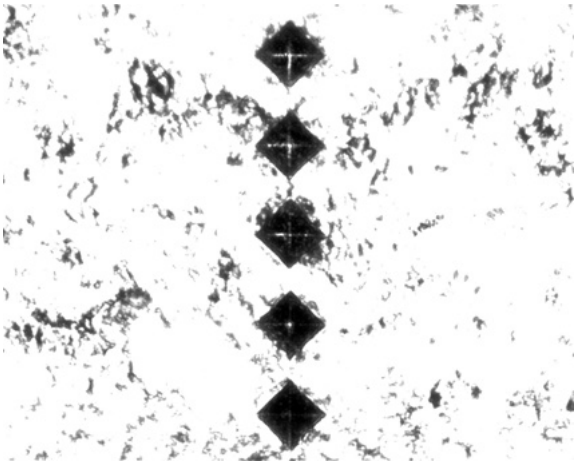

(c) Brightness enhanced

Figure 7.8: *Numerical treatment on hardness samples from laser cutting experiments*

Chapter 8

Laser beam cutting results and analysis

This chapter describes experiments conducted on laser beam cutting for U-10Mo bare foil manufacturing. The LBC process is essential to remove the enclosed bare foil from the stainless steel canister and resize it for PVD coating and aluminium cladding. Laser kerfs are measured with microscopic pictures. Then, additional mechanical tests are performed for further analysis around the laser kerfs produced.

Various experiments batches are realised for manufacturing parameters extraction:

- **Variation of laser power, cutting speed and assisting gas jet pressure separately** to understand their influence on the laser kerf produced;
- **Laser cutting of different materials with similar cutting parameters** to highlight the influence of material properties on laser kerf produced;
- **Hardness measurements of the laser kerf produced** to highlight the impact of laser cutting parameters around the kerf produced.

8.1 Laser cutting parameters influence on kerf geometry

8.1.1 Influence of laser power and cutting speed

Influence of laser power

This experimental batch of laser cutting concerning power variation is performed with **6 heat inputs** H_i values similar to the laser welding process. This experiment gives a first range of heat needed to cut U-10Mo foil. Table 8.1 summarises laser cutting parameters used.

	Experimental sets i					
Parameters	1	2	3	4	5	6
Heat input H_i $(J \cdot mm^{-1})$	H_1	H_2	H_3	H_4	H_5	H_6
Laser power P_i (W)	P_1	P_2	P_3	P_4	P_5	P_6
Cutting speed V $(mm \cdot min^{-1})$	V_R					

Table 8.1: *Laser cutting parameters for power variation on U-10Mo foils*

P_1 corresponds to the lowest power value and P_6 the highest. The cutting speed parameter is set to V_R as reference cutting speed. The highest assisting gas pressure is also set, with laser configured with highest gas pressure value PR_{max}. Figure 8.1 shows microscopic kerf pictures obtained on U-10Mo foil samples, with kerf width measurements plotted on Figure 8.2.

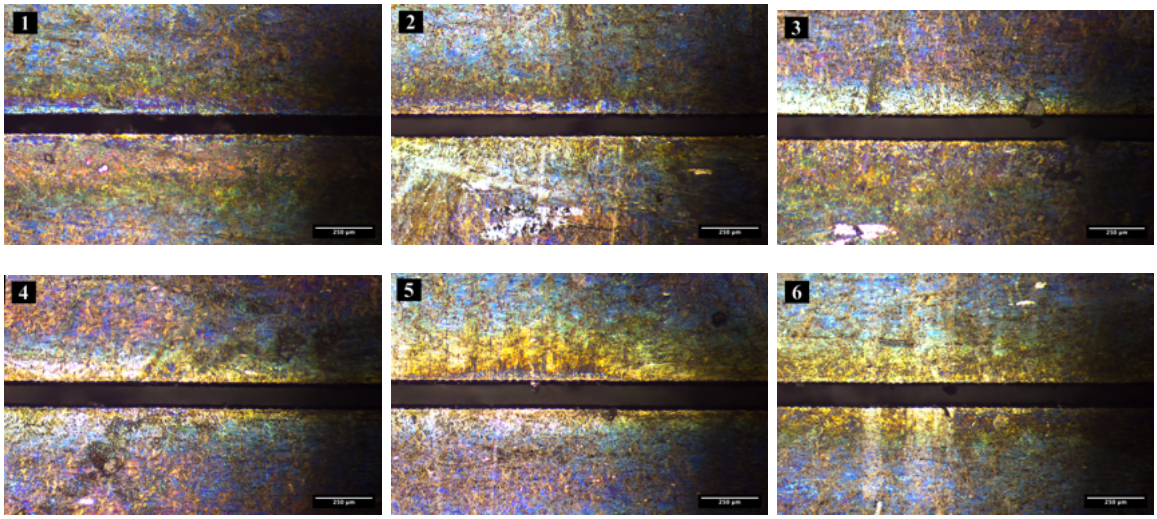

Figure 8.1: *U-10Mo laser cutting samples with laser power variation and constant speed*

The results indicate that all parameters set succeeded in cutting the foil, as kerfs are visible for each sample. The gradient of colour from yellow to shiny blue increases when power increases around the kerf produced. This phenomenon might indicate a higher HAZ for H_6 compared to other samples with lower laser power values. Regarding kerf appearances, some dross are visible into the kerfs for H_1, H_2, H_5 and H_6, with the small black artefact in the middle of the kerf. The overlapping of the laser spot is observable for each sample. Finally, the last sample H_6 looks visually thinner than other experimental sets.

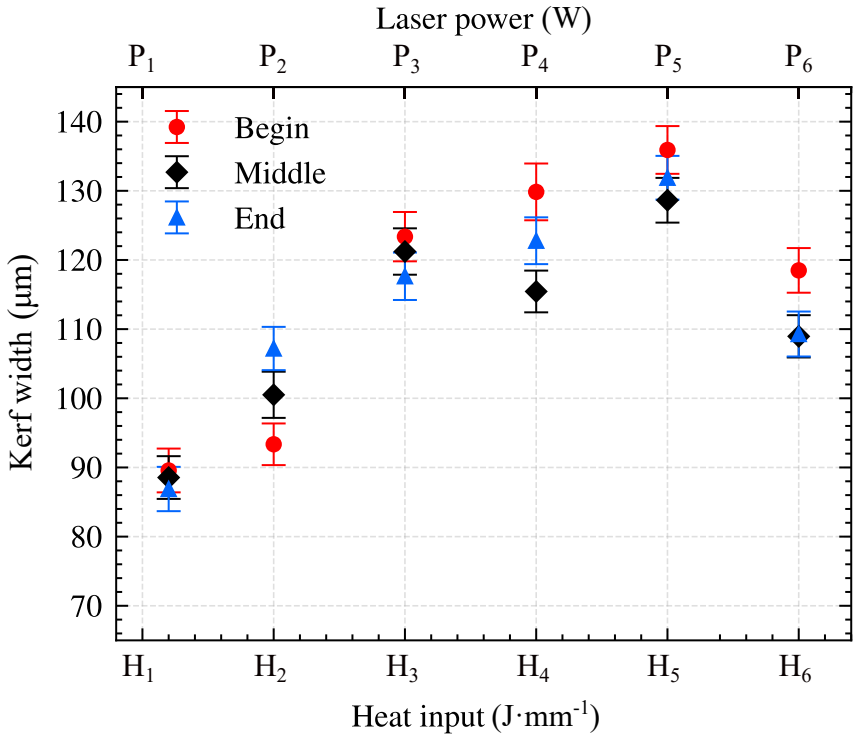

Figure 8.2: *Kerf width of U-10Mo according to heat input changes with laser power variation*

As shown in Figure 8.2, kerf width increases when the laser power increases. Similarly to the phenomena observed for the laser welding process, high laser power increases the melt pool created on the top and, consequently, the obtained kerf width. The kerf width follows a linear trend with both heat input and laser power, except for H_6 value which decreases compared to other parameter sets. Kerf width measured for this heat is lower and can be explained by a local thickness caused by the rolling process with inhomogeneous thickness distribution. The minimal laser power exhibits the lowest kerf width, around 90 µm. With low laser power parameters, thermal effects from the laser are reduced with a smaller melt pool and the heat effect on the rest of the foil. H_1 seems to be the best heat input value to obtain the lowest kerf width. Finally, all width values measured from the beginning to the end of the kerf do not vary more than 5 µm between each. These values stay homogeneous with variations in laser power.

Influence of cutting speed

This section of experiments concerns the cutting speed influence on the obtained kerfs. A similar cutting batch to laser power variation is performed with **the same six heat input values**. The cutting speed is modified for each experimental set with the constant reference laser power P_R and highest assisting gas pressure, as summarised in Table 8.2.

	Experimental sets i					
Parameters	1	2	3	4	5	6
Heat input H_i $(J \cdot mm^{-1})$	H_1	H_2	H_3	H_4	H_5	H_6
Cutting speed V_i $(mm \cdot min^{-1})$	V_1	V_2	V_3	V_4	V_5	V_6
Laser power P (W)	P_R					

Table 8.2: *Laser cutting parameters for speed variation with U-10Mo foils*

V_1 corresponds to the highest cutting speed, V_6 the lowest. The laser is configured similary to the previous laser power variation experiment. The working distance is unchanged during this experiment. Figure 8.3 shows microscopic pictures of kerfs obtained on U-10Mo foil samples, with kerf width measurements plotted on Figure 8.4.

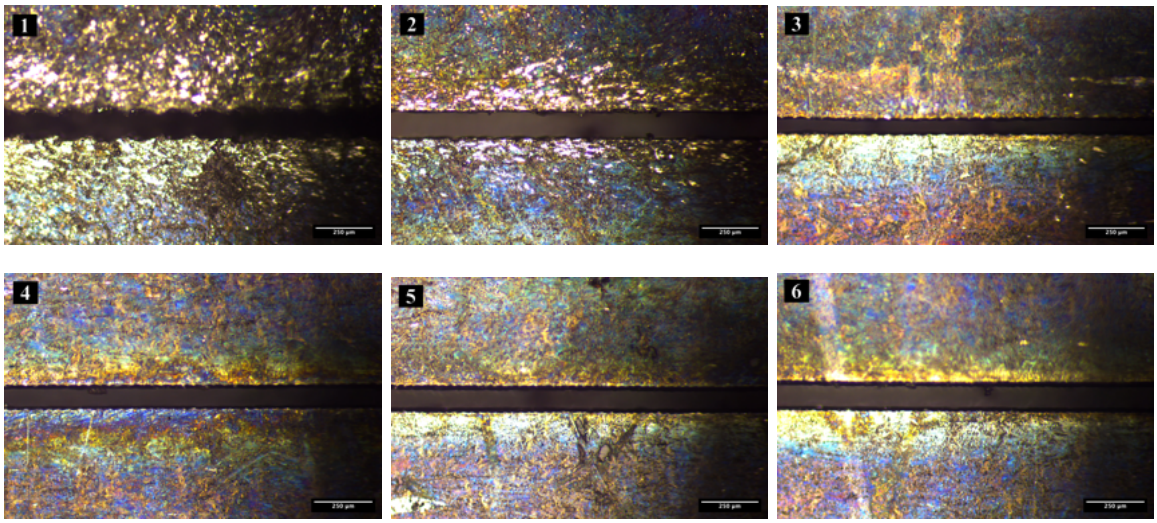

Figure 8.3: *U-10Mo laser cutting with speed variation and constant laser power*

In the same way as laser power variation, all heat inputs successfully cut U-10Mo foil samples. The multicolour gradient around the kerfs is still visible for each sample. Of interest here is the increase in overlapping caused by laser pulsation, i.e., a shared affected area by a laser pulse with the previous pulse.

It directly affects cutting areas and, consequently, the cutting pattern. Indeed, the laser spot emission remains the same in time through the laser source. Nevertheless, the time to cross the entire sample decreases when heat input increases due to the lower cutting speed used. Then, areas where the laser spot affects the sample, differ with cutting speed variation. H_1 with the highest speed seems to be the sample with the higher laser spot radius. All samples have laser spot overlapping expecting H_1. H_3 has the lowest kerf width from the microscopic picture and measurement plot. Another interesting aspect is the liquid drop of the melt pool visible for H_1 and H_2. The high speed performed ejects the liquid drop on the top of the kerf, solidifying on the surface around the laser kerf.

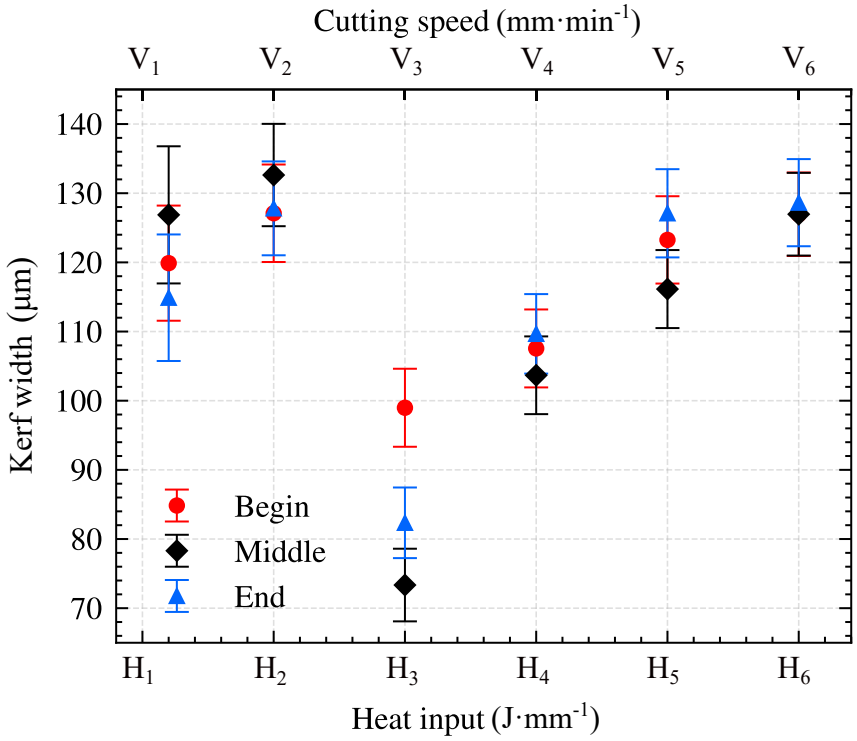

Figure 8.4: *U-10Mo kerf width according to heat input changes with cutting speed variation*

As shown in Figure 8.4 and compared to laser power variation, kerf width is not mainly affected by the cutting speed variation. Exceptions for H_3 and with reduced effects for H_4 heat input value are visible, where kerf width measurement is 10 to 50 µm lower than average measured for other heat inputs, around 125 µm. These lower values of kerf width for H_3 and H_4 are due to a local variation of U-10Mo thickness, similar to laser power variation, and the laser power reference chosen. Values extracted from the beginning, the middle and the end kerf confirm that the laser's position during the process does not influence the kerf width, with the highest standard deviation for H_1. Kerf widths measured along the kerf do not vary from each one, except for H_3.

8.1.2 Influence of assisting gas jet pressure

The laser cutting experiment for this batch focuses on the variation of assisting gas jet pressure, using **5 different values**. Laser power and cutting speed are selected from the best experimental sets, with the lowest kerf width, low dross quantity and best aspect as no burned areas or no-cut parts from previous experiments. Table 8.3 summarises the parameters used. PR_1 corresponds to the non-zero lowest gas pressure value, PR_5 the highest.

	Experimental sets				
Parameters	1	2	3	4	5
Assisting gas pressure PR_i (bar)	PR_1	PR_2	PR_3	PR_4	PR_5
Heat input H ($J \cdot mm^{-1}$)			H_R		
Cutting speed V ($mm \cdot min^{-1}$)			V_R		
Laser power P (W)			P_R		

Table 8.3: *Laser cutting parameters for cutting distance variation with U-10Mo foils*

Laser cutting parameters such as frequency, pulse duration and working distance are kept constant during the experiment. Heat input is maintained constant with selected laser power and cutting speed. Figure 8.5 shows microscopic pictures of the kerfs obtained on U-10Mo bare foil scraps, plotting width measurements on Figure 8.6.

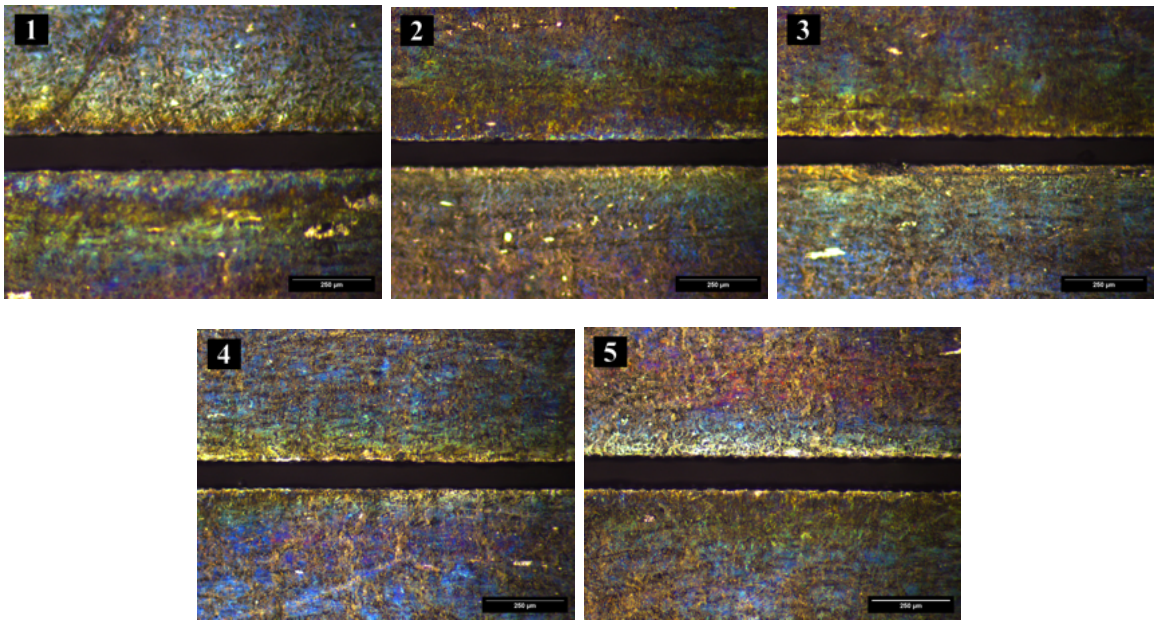

Figure 8.5: *U-10Mo laser cutting kerfs with assisting gas jet pressure variation*

All gas pressure values investigated during the experiment succeeded in cutting the U-10Mo bare foil sample. As the heat input is the same for all cutting lines, gas pressure variation does not influence laser overlapping or the global aspect of the kerf produced. Among gas pressure variations, PR_2 has the lowest kerf width compared to the others, with 84 µm. No variation in heat affected zone is visible from the microscopic structure, nor is the potential excess of dross in the entry or exit laser kerf.

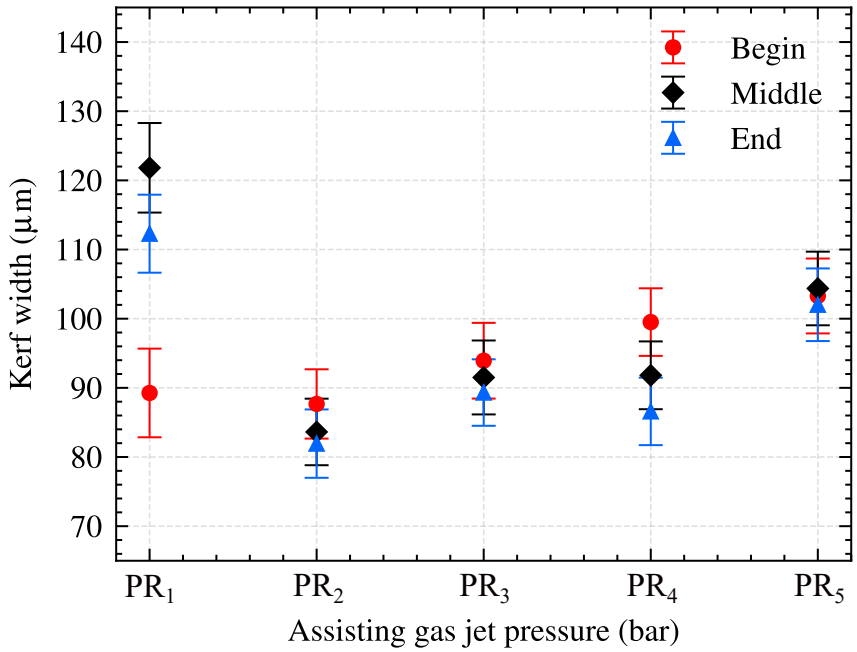

Figure 8.6: *U-10Mo kerf width according to gas pressure variation*

With increasing assisting gas jet pressure, a slight and continuous increase in kerf width is observable from PR_2 to PR_5 values as shown in Figure 8.6. An exception with the lowest pressure PR_1 is highlighted where irregular width variations over the cut length are observed. Kerf width measured increases slower than the two other experiments performed for laser power and cutting speed, with a relative increase of 23 % between PR_2 to PR_5 values. Without gas or low gas pressure, the molten material produced during the process cannot be ejected from the kerf. This particular manufacturing condition of laser cutting appears as a laser welding process. Laser cutting for PR_0, i.e. for no assisting gas shielding, is not plotted in Figure 8.6 and looks like welding of U-10Mo bare foil, and shown in Figure 7.5. Lower assisting gas jet pressure seems to lead to failure of the laser cutting process or to exacerbate defects on the kerf produced with high width and dross quantity.

8.1.3 Influence of working distance

The last parameter studied is the working distance, i.e., the distance between the sample and the nozzle used for the cutting process. **Nine working distances** are used with constant cutting speed and laser power, the same parameters for assisting gas jet pressure experiment to the maximum value. Table 8.4 summarises all parameters used.

	Experimental sets								
Parameters	1	2	3	4	5	6	7	8	9
Working distance F_i (mm)	F_1	F_2	F_3	F_4	F_5	F_6	F_7	F_8	F_9
Heat input H ($J \cdot mm^{-1}$)					H_R				
Cutting speed V ($mm \cdot min^{-1}$)					V_R				
Laser power P (W)					P_R				

Table 8.4: *Laser cutting parameters for cutting distance variation with U-10Mo foils*

F_1 corresponds to the lowest working distance value, F9 the highest. Figure 8.7 shows the kerfs obtained for these experiments with width measurements plotted in Figure 8.8.

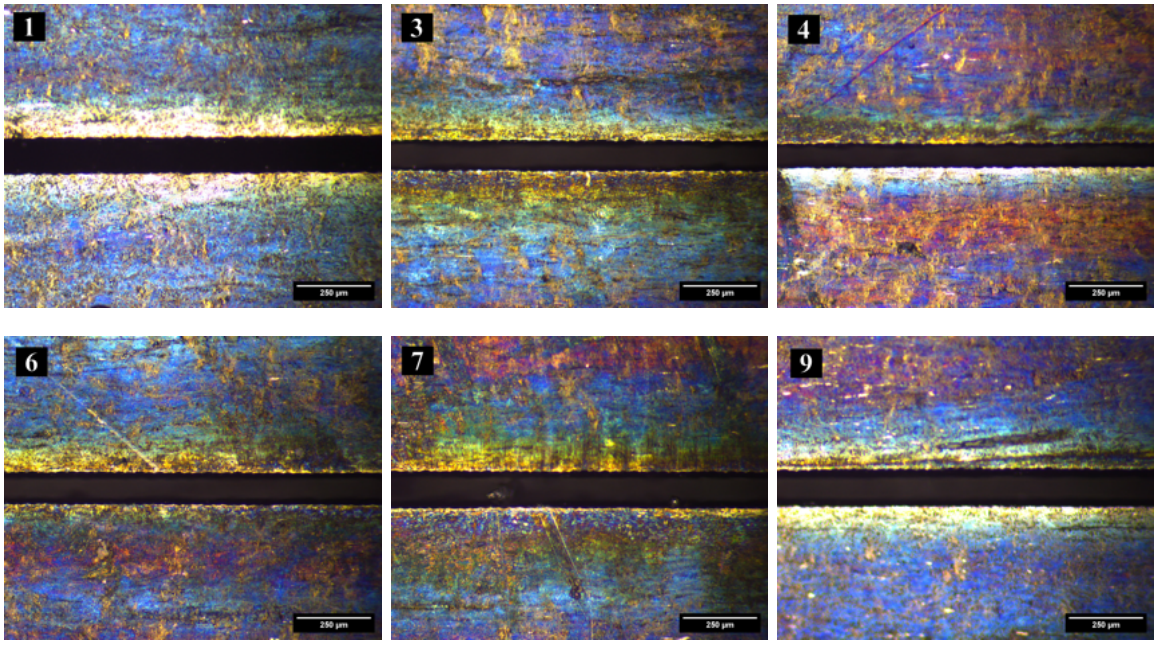

Figure 8.7: *Laser cutting kerfs on U-10Mo foil samples with working distance variations*

All working distances used for laser cutting succeeded in cutting the U-10Mo foil samples with visible kerfs. Laser kerfs from high to low working distances show several variabilities in width. In addition, some drosses are visible, with F_7 sample where black spots are visible in the kerf. The overlapping is still present on each sample, in the same way as prior experiments performed.

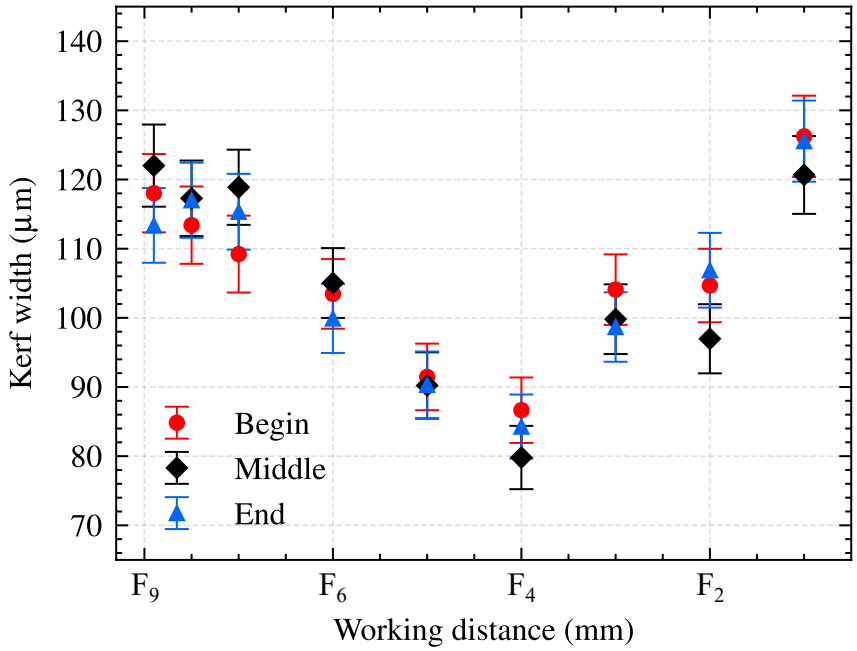

Figure 8.8: *U-10Mo kerf width according to working distance variation*

Regarding kerf measurements, the variation of working distance significantly impacts kerf width measured as shown in Figure 8.8. From the lowest working distance to F_4, kerf width follows a linear decrease to reach the lowest width measured around 85 µm, decreasing from the lowest working distance by 41 %. Then, from this value to the highest working distance, the kerf width increases linearly to reach a similar value as the kerf width measured for F_1, i.e., 125 µm. Figure 8.8 highlights the symmetrical behaviour of kerf width with an optimum for F_4. A limit working distance is then highlighted for F_4 to perform the optimal and lowest kerf width with the given laser power and cutting speed parameter. This working distance corresponds to a lower value than the lens's focal length, around F_3 from sample to cut. In consequence, the power peak must be inside the matter to reduce the kerf width for U-10Mo foils, for the given thickness of U-10Mo foil sample investigated between 0.4 to 0.3 mm.

8.2 Comparison between stainless steel and U-10Mo cutting

Studying laser cutting parameters influence between U-10Mo bare foil and the canister material is crucial for the U-10Mo bare foil removal. Parameters for industrial manufacturing are selected according to the kerf produced, the heat provided, and minimising defects added to the bare foil. After the hot rolling, the U-10Mo bare foil is removed by laser cutting the rolled assembly. It usually involves cutting the canister and the bare foil simultaneously due to mechanical constraints applied during the rolling process. Knowledge of similarities between both materials allows a better parameter choice to reduce the appearance of the defect on U-10Mo bare foils and to increase the process yield.

This section of laser cutting experiments concerns differences in kerf geometry investigated for stainless steel and U-10Mo samples, with similar thicknesses of 0.4 to 0.5 mm. The laser source with pulse duration and frequency remains constant. First, laser power variations and cutting speed experiments are performed similarly to previous experiments, with constant working distance and assisting gas pressure. Parameter sets are similar to those used before and summarised in Table 8.1 and 8.2. Then, assisting gas jet pressure and working distance experiments are performed on stainless steel for comparison with previous results from U-10Mo experiments. Parameter sets are similar to those used before and summarised in Table 8.3 and 8.4, with the same laser power and cutting speed. Figure 8.9 summarises the results obtained of kerf width for each of these experiments on stainless steel and U-10Mo foils.

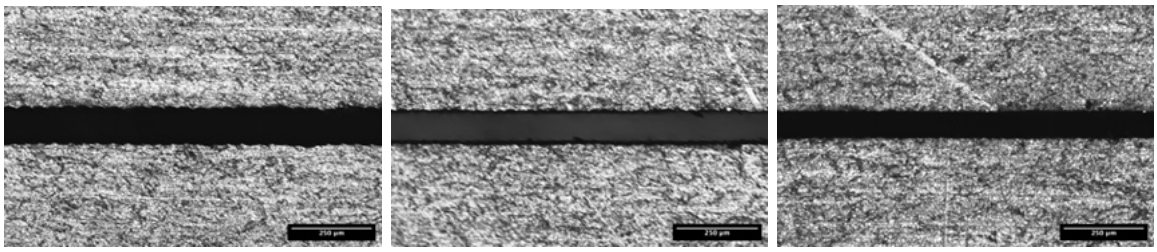

(a) Power variation with H_4 (b) Speed variation with H_4 (c) Focal variation F_5

Figure 8.9: *Laser cutting kerfs on stainless steel foil samples*

Both stainless steel and U-10Mo share several key features. The global aspect of kerf appearance is the same for both materials. All heat inputs successfully cut SS foil, similar to U-10Mo foils. An interesting aspect is the absence of burned areas or different gradient colours compared to U-10Mo. Finally, overlapping from laser pulse mode is still present according to the parameter set, as visible in Figure 8.9 - (a). Regarding kerf width measured, Figure 8.10 highlights interesting differences between both materials and for each experimental set.

Regarding heat input variations, kerf width increases linearly as U-10Mo. Unexpected values are measured, as H_1 for cutting speed variation or H_2 for laser power variation, which could be explained similarly by a local over-thickness or surface condition which affects the melting pool produced. For cutting speed variation, the kerf width between materials is close from H_4 to H_6. By contrast, laser power variation exhibits wider kerfs of 20 µm for U-10Mo, with the exception for H_2 & H_6 where stainless steel kerf width is higher than U-10Mo by 20 µm.

Assisting gas jet pressure and working distance shows that both materials follow similar trends. Regarding the gas pressure, the lowest value exhibits the highest kerf width. Widths follow a similar linear trend from PR_2 to PR_4. The highest value, PR_5, exhibits a difference of 20 µm between both widths, with the highest width for U-10Mo. Interestingly, the width increases for U-10Mo foils for high working distance while the width for stainless steel decreases. It does not have the same symmetrical behaviour as highlighted in Figure 8.8.

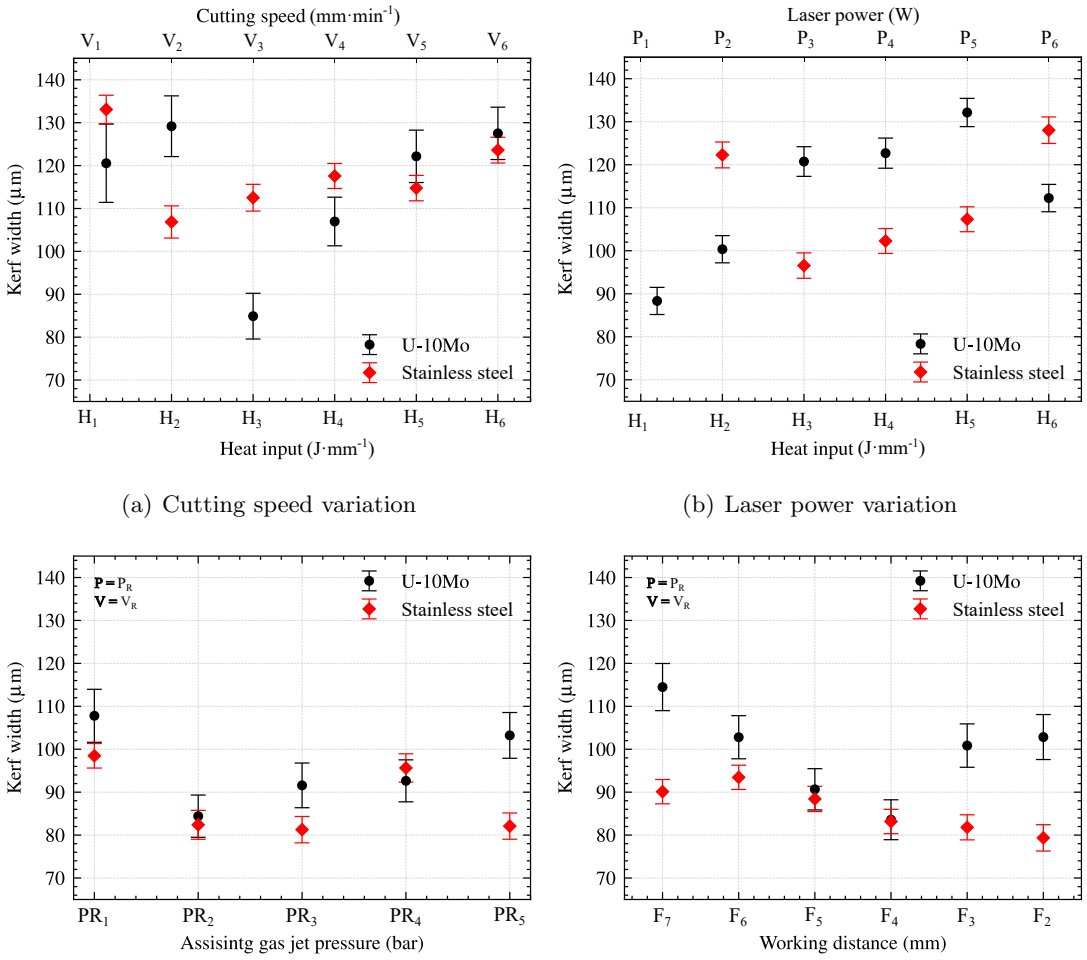

(a) Cutting speed variation

(b) Laser power variation

(c) Assisting gas jet pressure variation

(d) Working distance variation

Figure 8.10: *Kerf width comparison between U-10Mo and stainless steel foil samples*

8.3 Hardness measurements of U-10Mo cut edges

Cutting metallic foils involves complex thermal interactions due to heat provided to melt the material combined with laser cutting parameters. One of these aspects concerns local microstructure changes which occur on kerf borders. A first and simple way to analyse and exhibit potential changes in local microstructure is hardness experiments from the border of the kerf to the unaffected foil area. This hardness test is performed as explained in section 10.4 concerning hardness measurements by stamping the sample from the kerf border to the rest of the foil with a specific pattern. This experiment aims to characterise the length of the potential heat-affected zone provided by the laser cutting, with different parameter sets separated by laser power and cutting speed variation, summarised in Table 8.5 and 8.6. It involves cutting speed and laser power variation in the same way as laser experiments performed before. Assisting gas jet pressure PR and working distance F are not investigated, and values stay constant for these experiments.

	Experimental sets for power variation				
Parameters	**1**	**2**	**3**	**4**	**5**
Heat input H_i ($J \cdot mm^{-1}$)	H_1	H_2	H_3	H_4	H_5
Laser power P_i (W)	P_1	P_2	P_3	P_4	P_5
Cutting speed V ($mm \cdot min^{-1}$)				V_R	
Assisting gas pressure PR (bar)				PR_R	
Working distance F (mm)				F_R	

Table 8.5: *Laser power variation for hardness measurements with U-10Mo foils*

	Experimental sets for speed variation				
Parameters	**1**	**2**	**3**	**4**	**5**
Heat input H_i ($J \cdot mm^{-1}$)	H_1	H_2	H_3	H_4	H_5
Cutting speed V_i ($mm \cdot min^{-1}$)	V_1	V_2	V_3	V_4	V_5
Laser power P (W)				P_R	
Assisting gas pressure PR (bar)				PR_R	
Working distance F (mm)				F_R	

Table 8.6: *Cutting speed variation for hardness measurements with U-10Mo foils*

Figure 8.11 summarises results obtained from hardness measurements of kerf produced with each parameter set to U-10Mo foils. Hardness stamps were performed on the same U-10Mo sample to underline desired hardness variation from these measurements and to compare these values to a reference hardness of the sample. The reference hardness value was set to 337 HV after the laser's hardness stamping of the unaffected part.

Regarding global hardness values, measurements do not highlight a linear variation between the kerf border and the rest of the sample. Trends of values are polynomial fitting curves to match as close as possible to the values measured. They are mainly located around the reference hardness value. Few hardness stamps have values which divert from the reference. Grain boundaries, uranium carbides, differences in roughness and surface defects could affect these hardness values measured by affecting the stamp penetration load and, consequently, the geometry of the punch measured. Hardness kerfs have a wide range of uncertainties from 1 to 10 % for worst. These are mainly due to surface conditions which affect diameter measurements and uncertainties, as samples were not polished for the experiments.

Regarding heat input values H_1, high cutting speed seems to reduce the hardness of the kerf analysed, with a decrease by 10.5 % from the kerf border to reach the reference value at 245 µm from the kerf border. On the contrary, a low laser power increases the measured hardness value. In the average of both fitting curves, no variation in hardness compared to the reference with fitting curves is highlighted. For heat input H_2, no significant hardness variation for both cutting speed variation and laser power is also highlighted. No variation in hardness could argue for a low change in microstructure during the laser cutting with low heat input applied.

In contrast, for H_3 with laser power variation, the hardness value appears to decrease by 5 % from the reference in a reduced area before joining the reference value, around 130 µm from the kerf border. The same phenomenon is visible for higher heat input performed H_4 and H_5, where hardness values decrease respectively by 9.77 % and 6.98 %, and distance from the kerf border of 200 and 160 µm.

In contrast to laser power variation, experiments with cutting speed variation do not argue for changes in local microstructure except for H_1, where the hardness is lower than the reference. For other fitting curves, values vary with random distribution around the reference value to approach sinusoidal fitting curves as shown by Figure 8.11 - (c). The initial choice of high laser power for cutting speed variation experiments could explain the lack of evidence of hardness variation close to the kerf border. A high laser power value could bring a more significant influence on hardness variation compared to cutting speed.

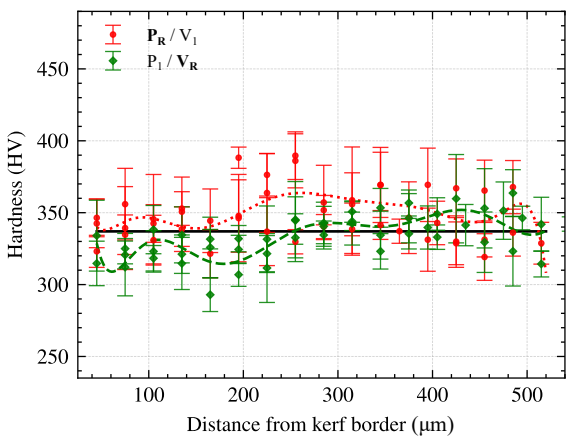

(a) Heat input H_1

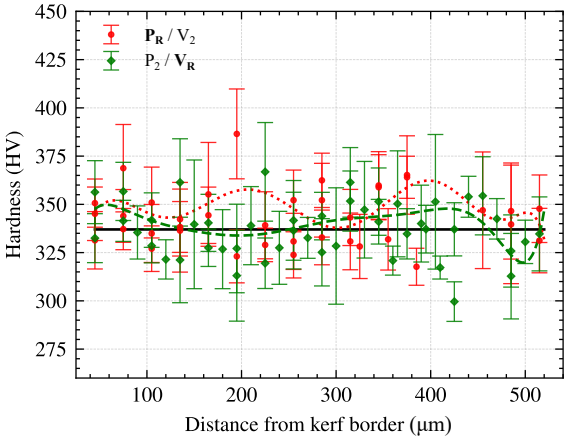

(b) Heat input H_2

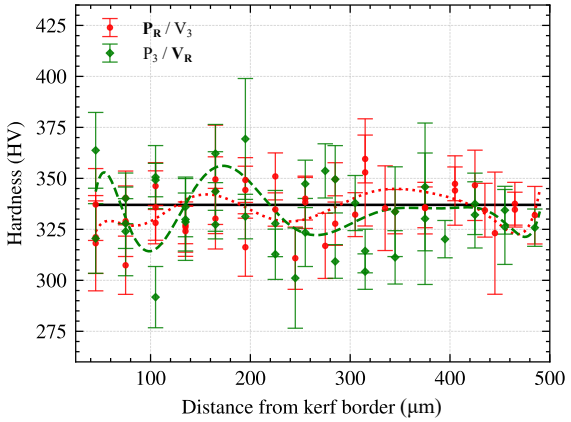

(c) Heat input H_3

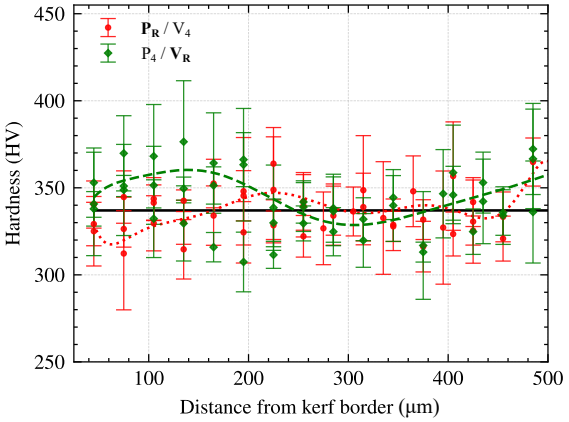

(d) Heat input H_4

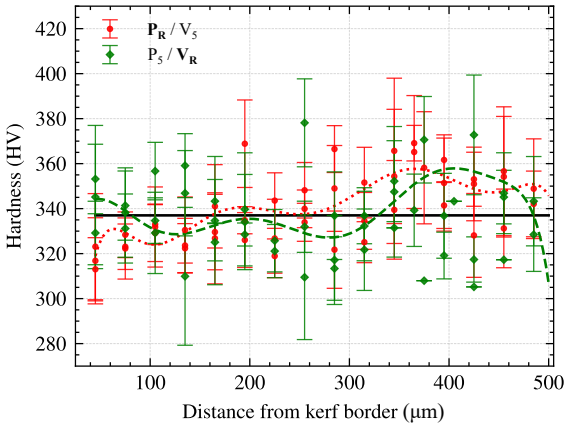

(e) Heat input H_5

Figure 8.11: *Kerf hardness for heat input variations on U-10Mo bare foils Circle ● : Laser power variation - Diamond ◆ : Cutting speed variation*

8.4 Discussion & summary

As highlighted by previous experiments, using laser technology as a cutting process for U-10Mo bare foils involves different interactions compared to laser beam welding. Kerf width results confirmed that LBC for resizing the foil is an appropriate manufacturing process to improve geometrical accuracy with specific parameters. Regarding laser power and cutting speed, the lowest heat input performed H_1 was enough to cut U-10Mo bare foil of 0.3 to 0.4 mm thickness, with an accuracy on the geometry of 45 µm for the lowest kerf width. In the same way as LBW, laser power increase still achieves to cut the foil. Nevertheless, the width measurement is higher compared to lower power values. The laser power should be increased to cut bare foils with higher thicknesses, where higher heat input is needed, or to cut a composite material with different thermal properties. It is the case in this work for U-10Mo assembly after the hot-rolling, where higher heat input values are used to remove the bare foil from the assembly. As the thickness of each layer is difficult to estimate, combined with potential waviness, which changes the working distance to use, appropriate parameters for both materials are necessary for the U-10Mo assembly cut. Laser power influence on LBC confirms trends and results from LBW where the same laser power variation increased weld width, comparable with the kerf width for LBC. Increasing cutting speed was also significant for kerf measured as speed influenced overlapping of the laser spot and kerf obtained.

Regarding the working distance, this parameter significantly influences the kerf geometry, with a lower width value measured for the working distance close to the focal length. According to experiments, the laser power peak should be inside the material to obtain the lowest kerf width. This parameter has to be strongly linked with the thickness of the foil to cut, as different thicknesses should lead to a different working distance to perform the cutting. The influence of assisting gas jet pressure was also investigated. It highlights that it has not an influence as crucial as laser power or cutting speed. Nevertheless, a gas flow excess seems to increase the width, and the foil quality with exit dross, as the gas pressure is essential to remove the formed liquid molten pool. In addition, the gas type is momentous for this process, as O_2 gas should oxidise the material and lead to material defects.

Both laser power and cutting speed also impact material properties from the U-10Mo bare foil with modification of local microstructure in HAZ. Hardness values obtained from experiments differ from other reports as U-10Mo foil samples were not polished and prepared for specific hardness measurements. However, it gives a first value and especially a good representation of hardness evolution with different parameters set of LBC. A lower heat input provides a lower HAZ and better homogenisation of material properties between borders and the rest of the foil. Nevertheless, a lack of laser power or a high cutting speed could also lead to a respective increase and decrease in the border hardness, as the heat input applied by the laser will modify the surface texture around the concerned area [108].

These differences in hardness properties could introduce cracks following mechanical stress provided by the hot rolling process. As U-10Mo bare foil borders have different mechanical properties than the rest of the foil, highlighted by hardness experiments, differences between hard and soft material could lead to cracks, as shown in Figure 8.12.

Figure 8.12: *U-10Mo bare foil with edges cracks after laser cutting resizing*

Choosing laser parameters for U-10Mo bare foil cutting in this manufacturing line, especially for canister removal and resizing, is essential to avoid fuel meat defects. Laser cutting with high variability of working distance due to different thicknesses or waviness of the foil after the rolling process leads to different manufacturing issues. In the worst scenario, these defects can be excess dross, dissimilar HAZ with different material properties, and foil cracks. These defects affect the aluminium-cladding process and decrease irradiation performance in the reactor. In addition, contamination from canister material, as shown in section 11.3.4 before EDX analysis, could happen during the LBC by mixing uranium and canister particles, mainly on the bottom of the foil. Resizing the foil, with appropriate parameters for U-10Mo according to the foil thickness, waviness and tolerances required, is essential to obtain the best U-10Mo bare foil before following manufacturing substeps.

Part IV

— Flat rolling process of U-10Mo alloy —

The hot rolling process is performed to reduce the high thickness of the U-10Mo casted ingot into thin U-10Mo bare foils. This process depends highly on LBW, as welding defects can lead to hot rolling failure and bring complex contamination and manufacturing incidents. The last part below reports all the work performed for U-10Mo rolling for this manufacturing line with specific parameter ranges, rolling mill calibration, and experiments with different canister materials. The goal is to extract the best U-10Mo bare foils in terms of thickness, waviness, and mechanical properties before the next manufacturing substeps for fuel plate manufacturing.

This last part is separated as follows:

- **A literature review of the flat rolling process, specifically for metallic and uranium materials** is performed. A theoretical approach to the process is reported by considering important mechanical values for this process and the mechanic behind the rolling process. Afterwards, a review of U-Mo bare foil manufacturing is performed to extract a first range of data about the canister used, rolling parameters selected, and results obtained on U-Mo bare foils produced;
- **Material and machines used for the hot rolling process** are described, with the range of parameters used and experimental set-up for the experiments performed;
- **Hot rolling results from various experiments, first with inert material and then with U-10Mo samples** are studied. The first experiments concern the rolling mill configuration and preliminary study of rolling parameters on inert materials, similar to the canister used for U-10Mo rolling. These experiments expose the influence of rolling parameters regarding the load required and the first parameter range for U-10Mo rolling. Then, an accurate investigation of the process with U-10Mo assemblies is performed to validate the previous parameters and to extract potential optimization paths to improve the production of U-10Mo bare foils.

Chapter 9

State of the art about flat rolling process

9.1 Theory and principles about flat rolling process

Flat rolling refers to **the permanent plastic deformation of a thick part** in its thickness profile by frictional contacts with rotating rolls in metallurgy. This process allows thin foil manufacturing, long products, and more complex geometric parts such as train rails or metallic rings with adapted machines. The rolling process is based on **a section reduction of raw products** with one or several passes. For rolling machines used in the industry, a minimum of two rolls and an auxiliary system allow variation of the distance between rolls and setting parameter sets to perform the process. Machines with a higher quantity of rolls exist. They are designed for industrial or specific foil production, as Sendzimir rolling mill machines with multiple rolls to ensure foil thickness and flatness.

(a) Industrial rolling mill [109] (b) Sendzimir rolling mill [110]

Figure 9.1: *Rolling mill machines implemented in metallurgical industries*

From the flat rolling process, mainly three parameters are essential to control the manufacturing and flat products obtained:

- **the differential in friction** between the ingot and the rolls during the entire process, and according to surface and geometry changes;
- **the normal pressure applied** to the sample by rolls with specific speed and roll radius;
- **the mechanical behaviour of rolled sample** with complex mechanical aspects between the rolled sample and the rolling mill machine.

First, frictional contact combined with a given normal stress from the rolls leads to the sample deformation. Figure 9.2 illustrates the process for an initial sample with a thickness h_A to achieve a rolling pass with a target thickness dimension of h_B. As the process is symmetrical from the central axe of the sample, only one part is represented on the rolling process scheme.

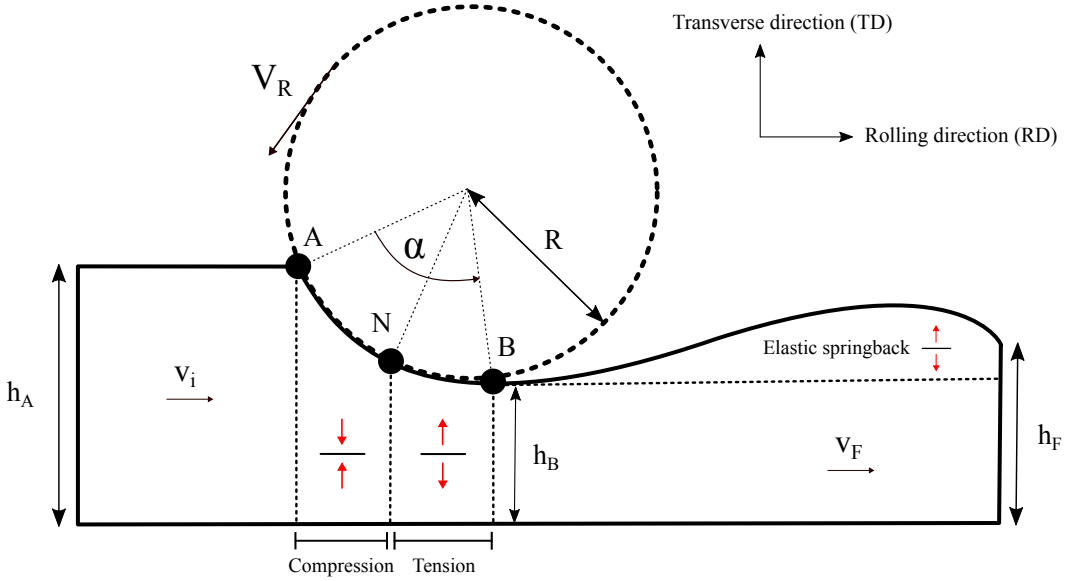

Figure 9.2: *Mechanical interactions scheme for flat rolling process*

The sample enters with a thickness h_A between rolls to perform the target thickness h_B. The entry angle bite changes and affects the stress measured and the rolling scheme according to initial thickness. Then, with a roll speed v_R and a bite angle α, the sample is pushed and pressed by rolls. On the contact area, three areas are discernible:

- Between points A and N, an **"engine" area**, where the sample is pushed and pulled along the roll and metallic guide. The part is mainly constrained under rolls by compression. During this time, the sample section is reduced with the necessary stress for permanent plastic deformation. The speed in this section is lower than the roll speed.

- Between point N and B, a **"brake" area**, where the sample is slowed down and maintained under the roll. The part is under tension, with stress applied between the limit for permanent deformation and material break. This section's speed is higher than the speed of entry and roll speed.
- Around point N, a **neutral area**, where the sample and roll speed are the same. The speed of the sample is equal to the speed of the rolls. Indeed, when the part is set to the entry of rolling, the initial speed is lower by conservation of part volume, as explained in Equation 9.1. It leads to material springback, also called elastic recovery, i.e., an elastic return of the material, which increases the final thickness compared to the target thickness h_B. A load parameter called **load-deflection** (LD) is usually set before the rolling to compensate for the material springback by adding additional load to the pass.

These three areas are explicable by the volume conservation of the sample during the process. The rolling process mainly affects the thickness value, which gives the sample a higher value in length. With a similar mathematical law in fluid mechanics for flow conservation, and assuming that h_A is higher than h_F, the following equation is obtained:

$$h_A.v_A = h_F.v_F \Leftrightarrow \frac{h_A}{v_F} = \frac{h_F}{v_A} \Leftrightarrow \frac{v_A}{v_F} = \frac{h_F}{h_A} \Leftrightarrow v_F > v_A \tag{9.1}$$

Each pass is subject to a specific rolling speed with thickness and length obtained from the previous one. An important parameter which sets up the rolling scheme is called **reduction ratio** $r_{\%}$. This ratio is applied for each rolling pass to ensure thickness reduction of the sample and calculated with entry and exit sample thickness as follows:

$$r_{\%} = 1 - \frac{h_F}{h_A} \tag{9.2}$$

The rolling process with thickness obtained after each pass can also be measured by using the **thickness ratio** $t_{\%}$ as follows:

$$t_{\%} = \frac{h_i}{h_0} \tag{9.3}$$

h_i : Measured sample thickness after the current pass (mm)
h_0 : Initial sample thickness prior to the rolling process (mm)

This last parameter is defined individually for each rolling pass and allows us to follow the process pass after pass with the load applied.

Rolls radius and entry and exit tension applied to the sample during the rolling also affect the stress applied and measured to the rolled foil. A high roll radius increases the stress applied to the sample, facilitating the rolling. However, roll radius increase is limited by the machine side and roll flexion under the sample pressure [111, 112]. In addition, by applying liquid or solid lubricant, friction coefficient modification affects the neutral point by moving it during the process. As the rolling process is mainly operated by the differential friction between the sample and the rolls, the modifying surface property could be interesting to optimise the process and have the required stress for rolling of U-10Mo. In this case, no lubricant is used for radiological and safety reasons with nuclear material. The mechanical behaviour of rolled samples and the initial geometry determine the rolling scheme performed during the process.

The permanent deformation induced by the rolling process is achieved when the stress provided to the part overcomes a specific value: **the yield stress**. This term refers to **the stress value needed to deform a material plastically**. The value usually taken corresponds to the stress needed for plastic deformation of 0.2 %. Yield stress values are usually found in reports and experiments written as σ_{YS} or $\sigma_{0.2}$. This inherent value to the material is not sufficient to determine the rolling scheme.

The stress value to overcome increases with a successive cycle of section reducing with work-hardening appearance, i.e., the appearance and distribution of micro dislocations into the sample during the rolling. Consequently, a higher specific load is needed to perform the rolling after several passes in theory. When the stress is too high, it leads to a material break, significantly if this value overcomes another inherent mechanical value of the sample: the ultimate tensile stress value or **tensile stress** usually labelled UTS, TS or σ_{TS}. For metallic material, these values are typically high, as shown in Table 2.2 with a comparison of $\sigma_{0.2}$ and σ_{TS} for different metallic materials. The workpiece can be heated to a specific range of rolling temperatures to reduce the load. A higher temperature decreases the $\sigma_{0.2}$ and makes the sample's formability easier. This process is named the hot rolling process, contrary to the cold rolling process performed at lower rolling temperatures. The terms cold and hot are different according to rolling and metallurgy. In metallurgy, hot refers to a high increase in the temperature of the metallic sample beyond room temperature. In rolling, to increase the ductility and to improve the metallic sample forming, this term refers to a working temperature higher than 0.5 of the melting temperature, usually between 0.5 and 0.7 [111, 113]. For example, the hot rolling of conventional aluminium alloys, performed at 400 °C, or even for other alloys with a low value of $\mathrm{T_M}$, could be considered cold rolling for stainless steel alloys. Both cold and hot rolling processes are similar in terms of mechanics, with differences in working temperature and mechanical purposes. Hot rolling is usually the first process to initiate thickness reduction, while cold rolling is performed as a finishing process.

9.2 Modelling equations for rolling

Many methods exist to model the rolling process with mechanical and thermal interactions, such as taking the deformation speed from each sample deformation line, with energy levels, or with the slice method [111]. Rolling process modelling is essential to optimise manufacturing steps. This section presents the slice method to highlight essential rolling variables. It separates the sample into infinitesimal slices and establishes the mechanical equilibrium for each. Figure 9.3 depicts external and internal loads applied to half of the slice.

The following assumptions are considered for the slice method for a slice between x and $x+dx$:

- **The gravity and inertia are not considering** into the equations;
- Deformation is considered as **plane with x-axis and z-axis** with no variation in width, i.e., in the y-axis, with no internal shearing loads;
- **Stress and deformations are homogeneous according to y and z-axis**;
- **Thermal equations are not considered**, as material properties are chosen according to the working temperature used;
- **The material springback with elastic return is not considered** in this part and fully plastic behaviour according to **Von Mises criteria** is selected as:

$$\sigma_{xx} - \sigma_{zz} = \frac{2}{\sqrt{3}}\sigma_{0.2} \tag{9.4}$$

- **The Coulomb equation** for the friction force τ, with normal stress σ_{n} and friction coefficient μ, is used as:

$$\tau = \mu\sigma_n \tag{9.5}$$

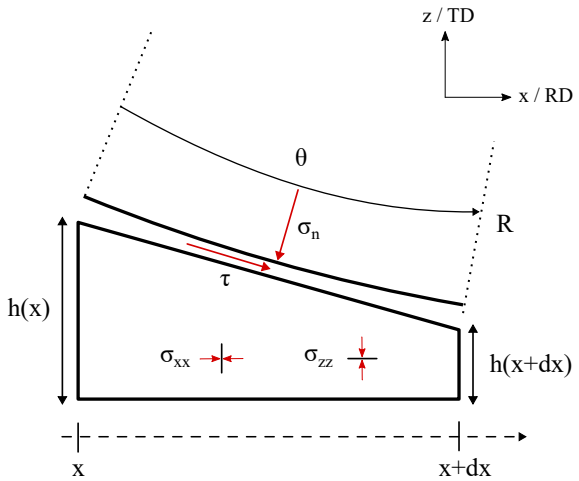

Figure 9.3: *Slice method resolution on half of the slice for the rolling process*

Regarding external loads, **normal stress** σ_{n} from rolls to reduce the thickness, and the **frictional tangential load** τ to lead the sample through the rolls, are applied to the top part. The length of this part is set to $Rd\theta$, where R is the roll radius and $\mathrm{d}\theta$ the infinitesimal angular rotation of the slice. With trigonometric laws and orthogonal projection, the affected top part length can be written as:

$$Rd\theta = \frac{dx}{\cos\theta} \tag{9.6}$$

Then, the applied load by projection on rolling direction x is written as:

$$(\tau\cos\theta - \sigma_n\sin\theta)\frac{dx}{\cos\theta} \tag{9.7}$$

As only a slice is set for the calculation, the sample has **boundary loads** to maintain its structural integrity on the right and left side, as governed respectively by the following equations:

$$-h(x)\sigma_{xx}(x) \tag{9.8}$$

$$+h(x+dx)\sigma_{xx}(x+dx) \tag{9.9}$$

The equilibrium equation for the slice by projection on rolling direction x can be written as:

$$d(h\sigma_{xx}) = (\sigma_n\tan\theta - \tau)dx \tag{9.10}$$

The equilibrium on the slice by projection in a transverse direction can be written as:

$$\sigma_n = \frac{\sigma_{zz}}{1 \pm \mu\tan\theta} \tag{9.11}$$

Finally, differential equations to calculate stress and thickness with the slice method and by replacing normal pressure, tangential friction load and σ_{zz} by equivalence with σ_{xx}, yield stress $\sigma_{0.2}$, rotation angle θ and friction coefficient μ is written as:

$$\frac{d(h\sigma_{xx})}{dx} = -\left(\sigma_{xx} - \frac{2\sigma_{0.2}}{\sqrt{3}}\right)\frac{\tan\theta \pm \mu}{1 \pm \mu\tan\theta} \tag{9.12}$$

Runge-Kutta methods will resolve these equations numerically to compare theoretical values and values extracted from experiments on both sides from the neutral point. The stress is calculated for both sides of the neutral zone with changes in sign of friction coefficient: positive on the left side, negative on the right side. The intersection point between these two plotted curves gives the neutral point and the entire stress plot measured.

9.3 Experiments about uranium-molybdenum alloys rolling

9.3.1 Hot rolling parameters performed

Rolling in metallurgy is the primary process to reduce element thickness for thin foil manufacturing. The U-10Mo flat rolling process involves different parameters, from flat rolling machine parameters to global material properties. With a melting temperature of U-10Mo around 1165 °C [6, 114], a theoretical temperature higher than 600 °C would be recommended to work in the high-temperature range of the alloy for hot rolling, i.e., 0.5 to 0.7 of the melting temperature. Interests for working in a range of high temperatures for U-10Mo bare foil manufacturing are to increase the sample ductility, to have easier formability and a better flatness of the ingot, and also to retain the isotropic γ-U phase structure for both irradiation and manufacturing purposes [22, 114]. More specifically, the hot rolling process should be performed at a temperature above the eutectoid, i.e., above 575 °C. This upper temperature is necessary to avoid γ-U decomposition into undesired anisotropic $\gamma\prime$-U_2Mo and α-U. Tensile tests on U-10Mo alloys with different working temperatures and strain rates highlight changes in ductility, especially for temperatures higher than 600 °C [43, 115]. Peterson et al. highlight that for work temperature higher than 550 °C, mechanical properties of the alloy decrease and make more manageable the alloy formability for the flat rolling process, with the addition that work hardening does not appear during the process [42]. During tensile tests, work hardening appears for temperatures below 550 °C for U-10Mo alloy [43]. A higher working temperature is needed to remove work hardening during rolling and to reach the easiest ingot formability. This condition is achievable in the case of bare ingot rolling, which is not the case for the US development due to the co-rolling of zirconium and in this work due to the welded metallic canister and potential chemical diffusion risks. Then, flow curves extracted from tensile tests at temperatures below 600 °C highlight a reduction in true stress [115] as well as heat treatment for U-10Mo recrystallisation [57].

Thus, the flat rolling process is conducted under a specific time range and with a specific temperature during the rolling between each pass. Usually, from reports and review about foil manufacturing, 10 to 20 minutes are enough between each pass to heat the sample, with an initial heating time of a few hours to heat the samples before the first rolling pass. Table 9.1 resumes parameters used for U-10Mo bare foil rolling from main manufacturing reports, with **entry thickness** h_e, **working temperature** T_{work}, **average reduction** per pass when available and **target thickness** h_s.

Author	Properties			
	h_e (mm)	T_{work} (℃)	Average reduction (%)	h_s (mm)
Sease et al. [116]	250	930	*Per pass*: 10 to 20	0.508
Moore et al. [85]	3.25	650	*Per pass*: 5 to 20	0.380
Brown et al. [117]	2.50	670	*Total*: -	0.450
Lisboa et al. [84]	3.11	680	*Total*: 81.65	0.508 - 0.490
Soulami et al. [118]	2.72	591 to 650	*Per pass*: 5 to 10	0.970
Hubbard et al. [119]	5.08	675	*Per pass*: ≧ 15	0.635 to 0.216
Schulthess et al. [43]	3.66	650	*Per pass*: 5 to 10	0.762
Nielsen et al. [120]	-	650	*Single pass*: 50, 65 & 80	-

Table 9.1: *Parameter range for U-10Mo rolling used for other manufacturing processes*

This table highlights that all target thicknesses are below the millimetre, with a global average value of 0.58 mm. One interesting aspect of these values is the similar working temperature used, which matches the prediction of hot rolling temperature for U-10Mo, i.e., around 600 ℃. The higher temperature from Sease et al. comes from the absence of canister material for rolling. This temperature range allows a higher range in reduction ratio for each pass. Different ways to heat the samples before the rolling step, such as a salt bath for Sease et al. or Brown et al. to oven heating for others, as reported in Table 9.1. In addition, the reduction ratio is between 5 and 20 % for each rolling step, according to initial and final thickness. Nevertheless, as canister material is used in both manufacturing lines, the parameters set with the balance between the reduction ratio, the heating temperature, and the canister material is essential to obtain the desired U-10Mo bare foil for fuel manufacturing.

9.3.2 Canister material used

For different reasons, a cladding canister to encapsulate the ingot is often used for the U-10Mo foil rolling. The co-rolling is performed with the U-10Mo ingot and additional thin foils of zirconium to roll in one time a coated U-10Mo foil ready for the aluminium cladding. It reduces the operation time and the produced foil cost. The US development of U-10Mo monolithic fuel is using this process for cladding the bare foil with a zirconium layer as a coating barrier [83, 85], which explains a temperature of 650 °C to ensure the sticking. The canister composition consists of a frame and two metallic plates, mainly low-carbon stainless steel, to enclose the ingot. Many materials were tested to satisfy the hot rolling process's mechanical and thermal properties: resilience under high clamping stress, high-temperature resistance and heat refractor capability during the rolling. Metallic materials able to handle these constraints were studied for the hot rolling process as described in Table 9.2.

	Canister material			
Author	Copper	Stainless steel	Zircaloy-2/4	Bare
Sease et al. [116]				X
Moore et al. [85]		X		
Brown et al. [117]		X		
Lisboa et al. [84]		X		
Soulami et al. [118]		X	X	X
Hubbard et al. [119]				
Schulthess et al. [43]				
Nielsen et al. [120]	X			
Pedrosa et al. [121]			X	

Table 9.2: *Canister material for U-10Mo foil manufacturing according to process reports*

Conventional and low carbon stainless steel [91], Zircaloy-2 and 4 [118, 121], and copper were used to extract the best canister material according to machining facility, high capability to handle mechanical stress and final geometrical properties for U-10Mo foils. The cost is also an important parameter because of the impossibility of reusing the canister for subsequent foil manufacturing. Experiment results highlight the fact that Zircaloy-2 as canister material is the best choice, according to Soulami et al., concerning the minimal gap between the U-10Mo ingot and canister on edges, and also by reducing inherent defects of the rolling process as dog-boning, flatness issues and thickness differential alongside the foil. These defects are due to a difference in mechanical properties between the U-10Mo ingot and the canister used [83, 85]. Then, a material with characteristics and flow stress similar to the U-10Mo ingot is more appropriate to reduce hot rolling defects. Nevertheless, the primary material used is stainless steel with low carbon content because of its low cost, good machining and rolling properties. Indeed, using expensive canister material does not match the industrialisation of U-10Mo bare foil manufacturing.

Defects occurring during rolling with composite materials using a canister are similar to bare rolling as flatness defects or cracks initiation during hot rolling. These defects are due to a difference in mechanical properties between the U-10Mo ingot and canister material. In addition to classic issues of the flat rolling process (flatness defects, cracks, dog-boning), canister use involves foil stickiness with the canister and void's appearance during the rolling. In order to avoid foil sticking during the process, different lubricants were applied to the U-10Mo coupon. Neolube^{TM}, a colloidal graphite paint, is used as a lubricant to avoid foil sticking and is easier to remove from the canister. Yttrium oxide Y_2O_3 is used in the same way, with a low quantity of carbon, to avoid carbon diffusion inside the U-Mo coupon [84].

9.3.3 U-10Mo bare foil analysis

U-10Mo bare foil microstructure resumes both mechanical and thermal properties of the fuel, as well as irradiation behaviour during in-pile operation. Investigation of foils obtained was realised to optimise the process and understand influent parameters.

Three parameters impacting microstructure have to be considered to minimise the swelling and to control thermal and irradiation issues during the in-pile operation: alloy composition, homogenisation procedure and thermomechanical constraints applied.

First, Mo homogenisation is only partially obtained after the different treatment processes. To resolve it, heat treatment procedures, with specific temperature ramps and heating duration, are needed to ensure Mo homogenisation and recrystallisation into the desirable γ-U structure. They are also needed after casting and during the flat rolling process to ensure the recrystallisation and the homogenisation of the U-10Mo sample. For as-cast ingots, the sample structure presents equiaxed grains with dendrites. The size depends on the Mo content and the annealing procedure: grain size measured by Nielsen et al. are 152 µm (U-7.4Mo) and 76 µm (U-9.5Mo) [120], 60 to 80 µm for Joshi et al. and then 174 µm (U-7.4Mo) and 98 µm (U-9.5Mo) after heat treatment respectively [55].

The influence of the carbon content in the alloy also affects the microstructure composition with uranium carbide. Grain size growth also depends on parameter sets for each process [43]. Typical grain sizes for as-cast, annealed, and hot-rolled ones have differences according to process, like microstructure after laser cutting and grain orientation by rolling. Wang et al. simulated numerically the distribution of carbides along rolled part [122], as well as Frazier et al. for grain growth [123]. Post-rolling heat treatment affects the grain structure and size, already affected by the dynamic recrystallisation occurring during the hot rolling process [124]. Numerical analysis was performed to understand grain refinement phenomena during heat treatment and flat rolling. It affects grains orientation and shapes with a privileged direction in rolling direction [57, 120, 124]. As-cast grain size is measured between 16 µm for a rolled part with annealing at 700 °C and 156 µm at 1000 °C [124, 56].

Chapter 10

Flat rolling process set-up experiments

Following ingot encapsulating by laser beam welding, the flat rolling process is the primary manufacturing step to transform the thick uranium ingot into flat foil. Experiments were performed to understand the influence of process parameters and have a first range for manufacturing. A dedicated rolling machine on a laboratory scale, with specific tools for experimental measurements, was used to perform U-10Mo bare foil manufacturing.

This chapter describes the hot rolling process used in this manufacturing line:

- **A description of the hot rolling machine** with its characteristics in order to perform the rolling process of the welded assembly;
- **The rolling scheme pattern** used for samples rolling;
- **The setting-up of experiments conducted on the hot rolling mill**, with material and methods used, in addition to hardness measurements conducted on different foil samples;

10.1 Flat rolling process equipment

U-10Mo bare foil manufacturing involves specific equipment which allows plastic deformation of thick uranium assembly into a thin bare foil for fuel manufacturing. The hot flat rolling process allows the flattening of thick samples and then making thin foil by reducing the stress yield needed to plastically deform and using high pressure and rotating rolls to perform the process. The machine used for rolling implemented in the CERCA^{TM} laboratory is shown in Figure 10.1, with Table 10.1, which sums up the machine parameters.

Figure 10.1: *Hot-rolling machine implemented in* CERCA^{TM} *laboratory*

Parameters	Minimum	Maximum
Thickness range (mm)	e_{min}	e_{max}
Rolling speed ($mm \cdot min^{-1}$)	V_{min}	V_{max}
Working temperature (°C)	T_{min}	T_{max}
Roll types available	2-Hi	4-Hi

Table 10.1: *Parameters range and controllers of the hot rolling machine*

The hot rolling experimental set-up is composed of the main machine in the middle of Figure 10.1 to perform the rolling and an oven on the left to ensure the heating of the samples during the rolling process. Two rolled tables are on the right and left sides of the rolling stand, i.e., the space where the rolls are set up. Ceramic tools are used within the oven to heat the rolled products during manufacturing to avoid temperature loss by conduction with the oven sides. Figure 10.2 shows an example of ceramic placement.

Figure 10.2: *One ceramic support configuration used for sample holding during rolling process*

10.2 Experimental rolling scheme pattern

Experiments follow the same pattern of rolling schedule, with only variation in parameter sets according to the experiment goals:

1. The sample is heated during the required time at the working temperature used;
2. Data for rolling parameters are set into the machine for the current pass;
3. The sample is extracted from the oven to be set on the entry stand for the rolling;
4. The entry width stand is adapted according to the sample width;
5. The sample is pushed between the rolls to perform the current pass;
6. The sample thickness is measured and returned to the oven for the next pass.

All rolling parameters must be filled in into the human-machine interface for each pass. It has to consider the goal of the experiment conducted and the previous pass realised to set up the next pass parameter set. Thickness measurement performed in the previous step 6 is the most critical value for the rolling schedule, with load applied to avoid mechanical failures of the machine or the rolled assembly.

10.3 Material & methods

10.3.1 Experimental set-up and tools

Before rolling, the sample is measured in length, width and thickness to compile initial assembly data. The thickness is the most important as it determines the reduction ratio to perform for each pass. Samples used for the hot rolling scheme are designed according to the initial geometry of the induction casted ingot. Then, it is encapsulated into the metallic canister by LBW. Protective equipment with a protective helmet, aluminium protective coat and gloves are required. A wrench is used to handle samples at high temperatures from the oven to the entry rolling stand.

10.3.2 Experimental measurements

Results of rolling experiments are constituted with values of maximum load measured, the temperature at entry and exit rolling stand, and thickness measured before and after the pass, with corresponding reduction ratio. Figure 10.3 describes a typical rolling pass with the load measured, its variation, and speed variation with temperature recording moment.

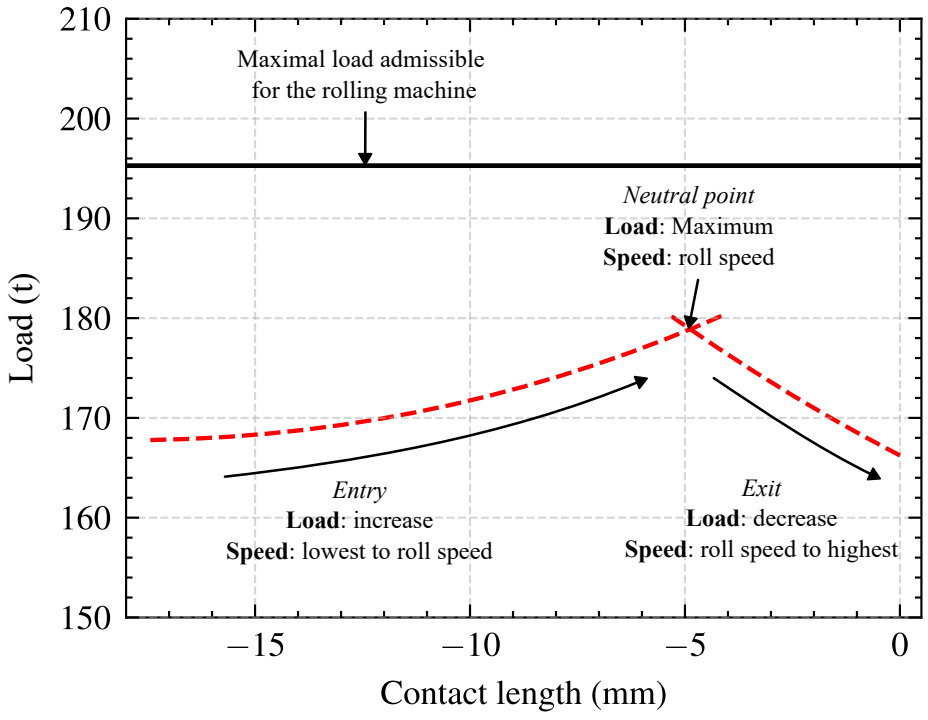

Figure 10.3: *Load curve from a hot rolling pass. The process begins at the left with the entry temperature measurement. Then, the load and the speed increase until the neutral point, where the maximal load is measured. Finally, the product goes faster with a lower load value to finish the rolling pass, where the exit temperature is measured again.*

The sample temperature is measured with at the entry and exit rolling stand machine to obtain a valeu of the temperature lost during the rolling pass, which has to be well-known to highlight the heat loss after each pass.

Regarding load measurements, the maximum value is measured during each rolling pass according to the rolling scheme performed. As measured loads depend on roll radius and material rolled, a parameter called **load ratio** $l_{\%}$ is used to describe loads applied to the sample as follows:

$$l_{\%} = \frac{l_i}{l_{max}} \tag{10.1}$$

l_i : Applied load during the current rolling pass (t)
l_{max} : Maximal load admissible for the rolling machine (t)

Finally, the thickness measurement is performed with a micrometre after each rolling pass to prepare the next rolling pass by setting-up the rolling parameters such as rolling speed and reduction ratio.

10.4 Mechanical analysis by Vickers hardness study

After hot rolling experiments, hardness measurements are performed to extract the sample's first range of mechanical behaviour. Hardness measurements were performed according to standards for Vickers hardness measurement on metallic materials [125] to set the proper distance between marks and loads used for the hardness measurement. The penetrator sets here is a straight pyramidal one with a square base, with an angle α of 136 °. Marks are performed with an experimental load F mentioned in the results. Diagonals d_1 and d_2 are then measured in order to calculate Vickers hardness (HV) as shown in Figure 10.4.

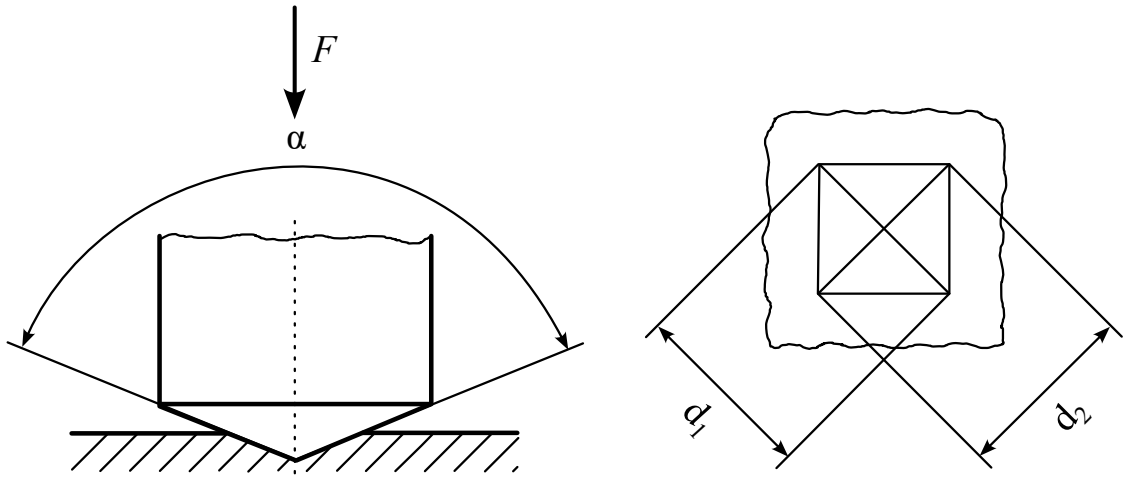

Figure 10.4: *Mark geometry for Vickers hardness measurements* [125]

Both cross and flat-section hardness measurements were performed, i.e., respectively, in the normal thickness direction and the normal top surface direction when the sample can be removed from the canister. In other situations, the location of measurement will be mentioned. The number of marks would differ according to the sample size, and this value is mentioned in the results part when hardness measurement is presented, in addition to the load used. Then, random spots in each section were selected for an acceptable measurement distribution. Vickers hardness obtained from diagonal measurements is calculated according to the following formula [125]:

$$HV = \frac{1}{g_n} \frac{2F \sin \frac{\alpha}{2}}{d^2} \tag{10.2}$$

HV : Hardness value (HV)
g_n : 9.80665 $\mathrm{m \cdot s^{-2}}$ - Conversion constant from Kilogram-force **kgf** to Newton **N**
F : Experiment load applied to mark the sample (N)
α : Penetrator angle with an angle of 136 °
d : Diagonal average from $\mathrm{d_1}$ and $\mathrm{d_2}$ from experimental marks (mm)

Chapter 11

Flat rolling process results of U-10Mo

This part presents studies on the hot rolling process of U-10Mo bare foils conducted for this manufacturing pilot line. Different material sets are used to exhibit the best combination for the canister and the rolling parameter sets to be used for the U-10Mo bare foil manufacturing.

Different experiments were implemented to identify suitable parameter sets according to the welded assemblies and experimental data measured:

- **Hot rolling parameters** were investigated by performing load-deflection experiments on samples with similar material and geometries to U-10Mo assemblies. Rolling speed, reduction ratio and working temperature for the rolling process were then studied with similar materials;
- **Inert samples, both monolithic and welded**, i.e., rolling of one material block and welded assembly with encapsulated ingot, are rolled to understand material behaviour and foil characteristics. Experiments on two welded sample types allow to highlight manufacturing differences and extract a first range of parameters for U-10Mo bare foil manufacturing. In addition, different sets of materials with slightly different mechanical behaviour were used, with various ranges of rolling parameters. The goal is to highlight the influence of mechanical properties on composite material rolling;
- **U-10Mo assembly samples** are then rolled to keep the canister's mechanical integrity and remove the U-10Mo bare foil after the process. Foils were characterised by hardness, waviness profile, microstructure and chemical composition.

11.1 Hot rolling parameter influence

11.1.1 Load-deflection and roll calibration

Mechanical properties from initial samples and the rolling machine impact the rolled products. Under mechanical stress, the sample and the rolls are stretched like springs to store energy from contact pressure to reduce the product thickness. This phenomenon leads to a thickness measured at the stand exit greater than desired with the rolling scheme, known as **material springback**. It is now understood that this springback plays an important role in rolled products, especially for achieving the targeted thickness and matching with tolerances, but also for the structural quality and absence of defects. The elasticity of the rolled material leads to a mechanical springback at the end of the pass. As total strain of the product ϵ_{tot} is equal to the addition of both elastic ϵ_e and plastic strain ϵ_p, when the product exits the rolling stand, ϵ_e reaches null value as shown in Figure 11.1.

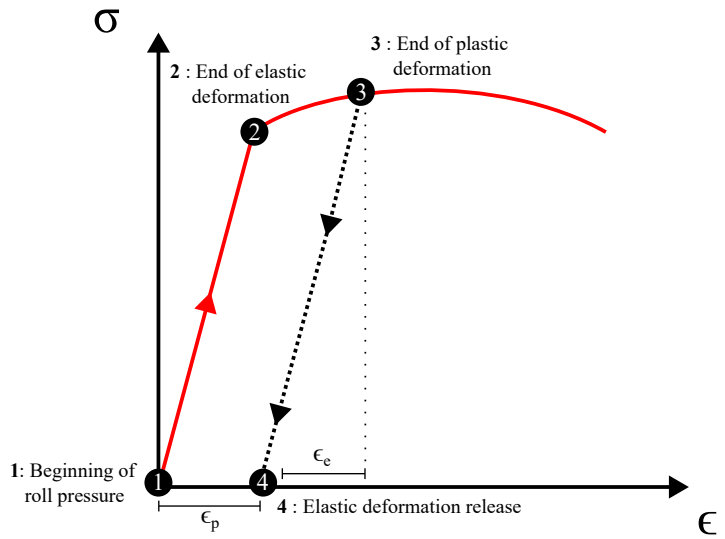

Figure 11.1: *Example of the stress-strain curve of the sample during the rolling process*

The roll's and sample's elasticity play a significant role in the material springback by contact with the products. In addition, the transmission chain through rolling mill components involves thickness variation during the process. Material springback and transmission chain through rolling mill components are critical driving factors of thickness variation between the targeted and measured thickness. Then, a parameter called **load-deflection** (LD) allows us to reduce this phenomenon. This parameter corresponds to the added stress needed to compensate for the material springback. It must be controlled and known for each rolled material, especially for composite ones involving different properties. Experiments called **push tests** must be performed to obtain the range of load-deflection required. These tests are dedicated to the specific material rolled and the rolling scheme performed.

With the stainless steel material used in this work, three push tests were implemented using **three different LD values**, labelled LD_1, LD_2 and LD_3, from the lowest to the highest value. Each experiment was performed with constant LD chosen at the beginning of the process. Monolithic stainless steel samples, with similar alloy and geometry to the canister, are rolled for each push test. A monolithic stainless steel sample refers to one block without encapsulated ingot. Regarding the rolling scheme, a reduction ratio is set according to the thickness measured from the previous pass, with a wide load data range and thickness values for future parameters choice for U-10Mo bare foil rolling. The working temperature is constant and set to T_1. Separated results of each experiment are shown in Figure 11.2, with bare plots for thickness measured and scattered points for maximum load.

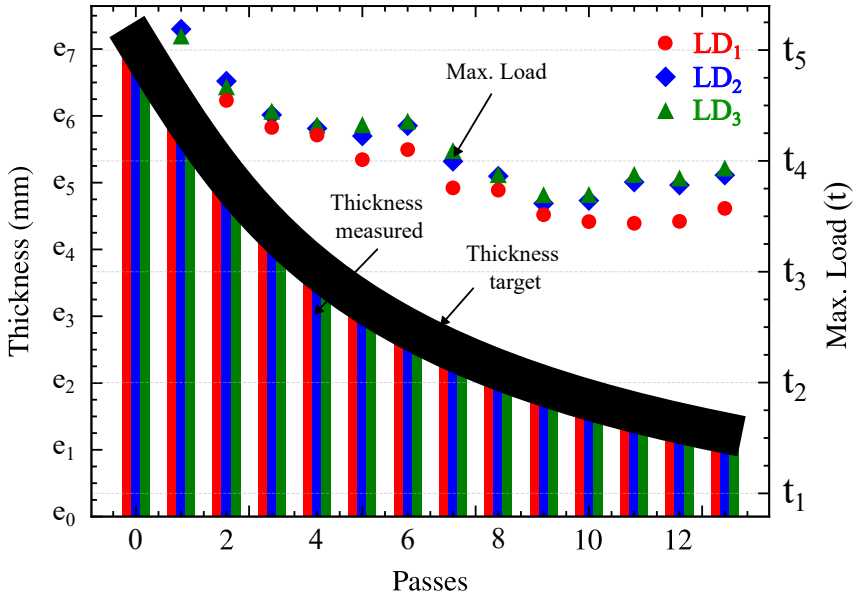

Figure 11.2: *Thickness and maximum load with different LD for monolithic stainless steel*

First, the measured load data decreases with passes realised when the reduction ratio decreases. As the roll distance ratio with the rolled sample increases, the load applied decreases. Interestingly, the correlation between the theoretical and measured thickness does not follow the same tendency from pass 6 onward for each load-deflection value. For the highest LD value, thickness deviation increases compared to the two others. Indeed, for the pass 8, the difference between the thickness target and the measured thickness values is for LD_1, LD_2 and LD_3 respectively 1 %, 4.6 % and 9 %. For the last pass 13, this variation becomes 2 % for LD_1, 6 % for LD_2 and 12 % for LD_3. Load-deflection has to be chosen according to the targeted thickness to match it without exceeding the maximal load available for the rolling machine. For the material and rolling machine used here, a load-deflection value between LD_1 and LD_2 is suitable to match the thickness target.

These push tests are used to plot the maximum load needed according to the difference between the target thickness and the measured thickness. The difference between both values is the **delta thickness**. This parameter is linked with the load applied during the rolling process and then permits the choice of the right amount of load-deflection needed to perform the rolling pass. Figure 11.3 shows the plot of maximum loads measured from previous experiments according to the delta thickness calculated for each rolling pass and each push test. The null delta thickness value, i.e., a measured thickness equal to the target, represents the theoretical load needed to compensate for the material springback from the beginning of the rolling process for monolithic stainless steel. For a variation in thickness, the LD value needs to be adjusted to perform the next rolling pass to achieve the desired thickness.

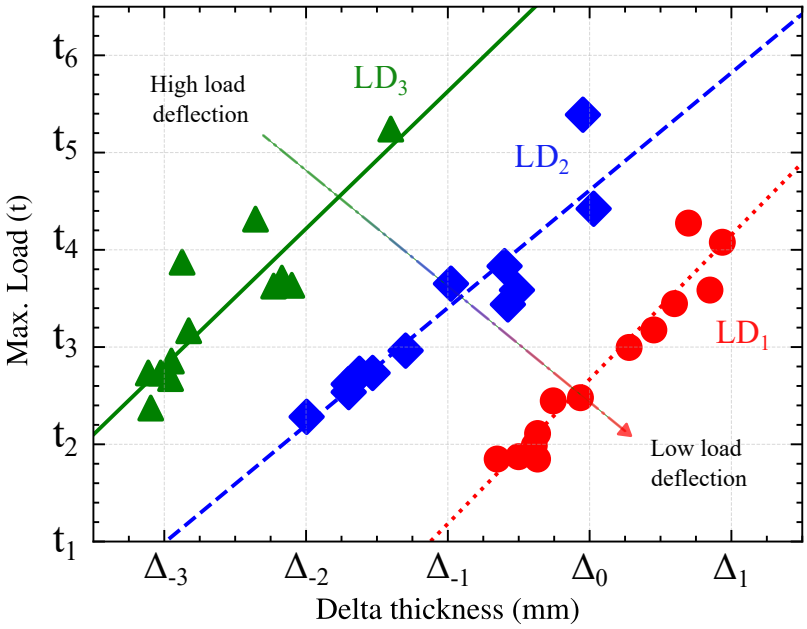

Figure 11.3: *Load-deflection curves with stainless steel material*

The plot of maximal load according to delta thickness shows that when the maximal load increases, the thickness value measured is lower than expected, i.e., the delta thickness value is negative. On the other hand, a reduced load value involved higher thickness in stand exit compared to the theoretical, i.e., the delta thickness value is positive. Finally, the load-deflection applied drives the intercept value with null delta thickness: high LD values lead to a high intercept with null delta thickness. The load-deflection is necessary to achieve the thickness target of the rolling scheme and optimise the stress applied during the rolling. It represents an entry parameter to correct the thickness variation. It is necessary to optimise the flat rolling process according to the rolled sample material. Previous push test experiments are mandatory to ensure the geometry requirements for rolled assemblies.

11.1.2 Working temperature and reduction ratio influences

Several factors are essential in the hot rolling process to control foil manufacturing. Both **reduction ratio** and **working temperature** contribute to the sample deformation and the rolled foil properties. By reducing the roll gap, the ingot inserted into the rolling mill cage handles more stress with a high reduction ratio. The working temperature is another significant parameter affecting the deformation rate and the stress needed for the sample plastic deformation by modifying its mechanical properties.

Regarding the working temperature and its influence, **two values**, labelled T_1 and T_2, with T_1 higher than T_2, are experimented. These two temperatures are chosen to be higher than 0.5 of the melting temperature of U-10Mo alloy. Samples used are the same for both working temperatures, similar to the stainless steel alloy canister used for the U-10Mo bare foil manufacturing, with the same initial geometry. Then, the same reduction ratio scheme is applied for each batch. A constant reduction ratio is applied per pass according to the thickness measured during the previous passes, until the foil target thickness is reached. The load-deflection applied is set according to the push test realised for this material sample in paragraph 11.1.1. Figure 11.4 and 11.5 present a visual inspection of the produced foils.

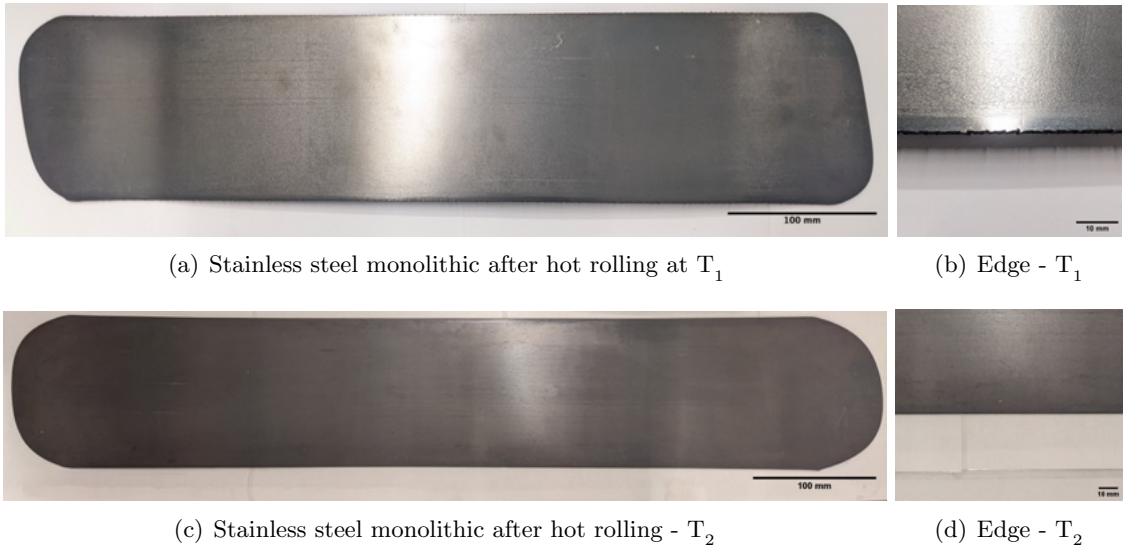

(a) Stainless steel monolithic after hot rolling at T_1

(b) Edge - T_1

(c) Stainless steel monolithic after hot rolling - T_2

(d) Edge - T_2

Figure 11.4: *Stainless steel monolithic samples rolled at different temperatures*

Figure 11.4 exhibits an example of two rolled foil samples after a hot rolling schedule for temperature values T_1 and T_2 with similar final thicknesses. First, the surface condition is the most striking result of these two foils. For T_1, the surface is shiny with less oxide layer. In comparison, foil rolled with T_2 temperature has a tint more matt, with higher oxide layer thickness on its surface.

By looking to Figure 11.4 - (b) and (d), respectively showing edges from T_1 and T_2 samples, more cracks are visible on the first sample compared to the second one. Lower working temperature leads to higher crack distribution on edges, with less oxide layer on foil surfaces. Finally, samples rolled at T_1 are more wavy compared to T_2.

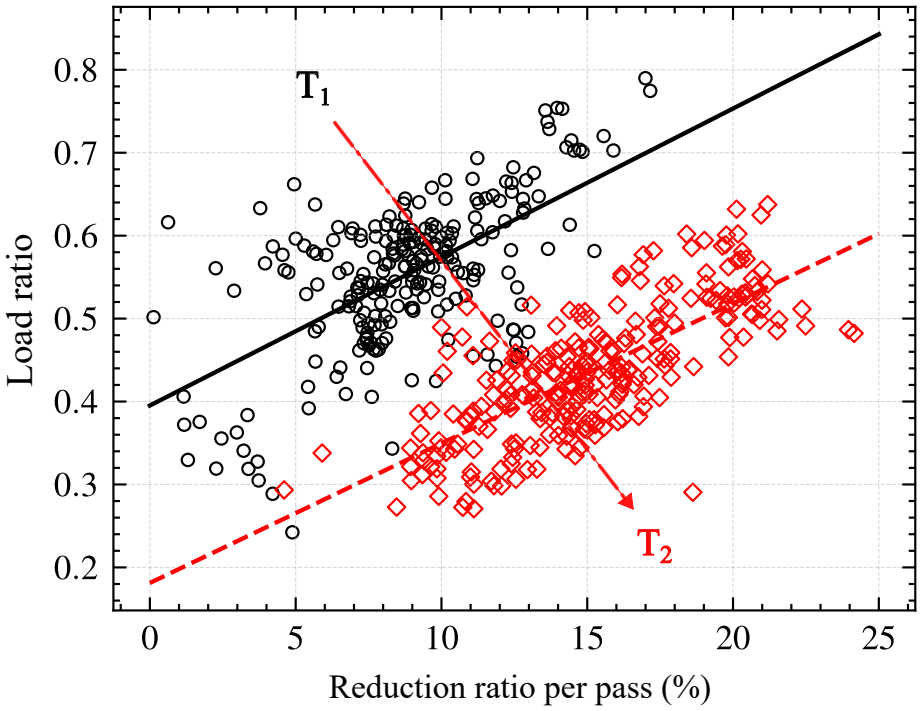

Figure 11.5: *Load ratio comparison of monolithic stainless steel with working temperatures*

Figure 11.5 compares the experimental data of the load ratio measured according to the reduction ratio for both working temperatures. The load ratio is the ratio value between the maximum load measured during the pass and the maximum load achievable by the rolling machine in operation without failure. This plot is quite relevant in several ways. First, strong evidence of working temperature influence is highlighted. High working temperature leads to a lower load ratio measured for similar reduction ratios applied. For the same reduction ratio applied, the load measured is higher for the sample hot rolled at T_1 compared to the sample rolled at temperature T_2, more than twice the load value of T_2. It can be seen that the load ratio follows a linear regression while the reduction ratio increases for both working temperatures. Finally, a lower reduction ratio leads to higher uncertainty ranges, as seen in the graph for reduction ratio from 0 to 5 % for working temperature T_1.

11.1.3 Rolling speed influence

Rolling speed is another parameter to understand and control the hot rolling process. The rolling speed influences material with differences in strain rates applied similarly to tensile tests with deformation speed. Experiments with **four rolling speeds**, labelled V_1 to V_4, are performed. V_1 corresponds to the lowest value and V_4 the highest. Speed roll control is only on the peripherical speed, i.e., the tangential speed of each point on the roll edge. Indeed, as the samples rolled are not deformed in the same way within each area, the local thickness is different between the entry, middle and exit stand. By volume conservation, the ingot speed does not follow the roll speed except at the neutral point. In these circumstances, the roll speed affects the ingot speed, and its speed is not equal to the peripherical speed during the entire process. Both temperature loss and thickness ratio measured with load applied are highlighted by this experiment. The thickness ratio is the ratio between the thickness measured at the end of the pass performed and the initial thickness before the rolling scheme, i.e., before the first rolling pass. Figure 11.6 depicts these measurements.

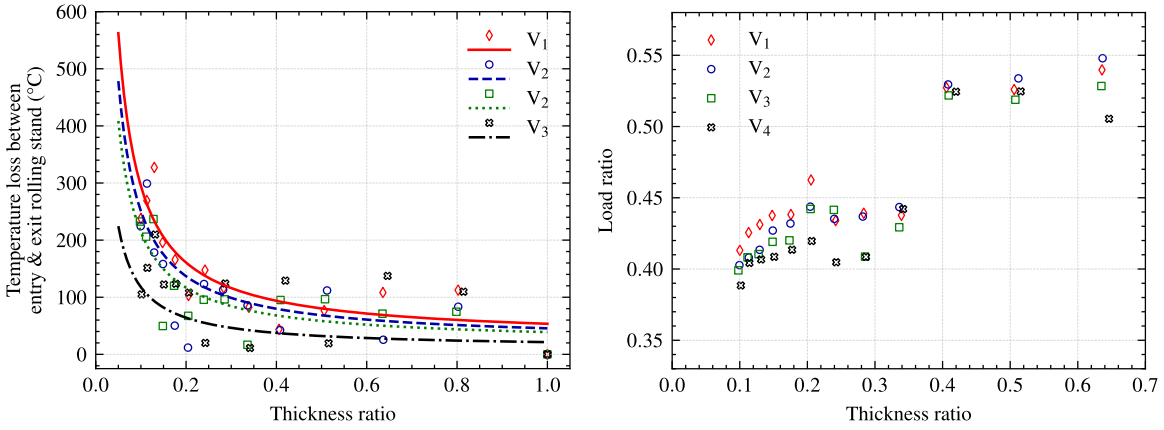

(a) Temperature loss between entry and exit stand

(b) Load measurements according thickness ratio

Figure 11.6: *Experimental results for hot rolling of monolithic stainless steel with different rolling speed and similar working temperature and rolling schedule*

Regarding temperature loss during the hot rolling process, Figure 11.6 - (a) highlights a tendency for low-speed value V_1 to increase heat loss compared to the highest V_4. Speed variation may cause heat loss during the time spent under the rolls. What can be seen in this plot is the phenomenal growth in heat loss when the thickness ratio achieves the value of 0.4 from 100 °C. It reaches a maximum value of a few hundred degrees when the thickness ratio is close to zero. Moving on now to consider the load measured. The load is not varying for each rolling speed. Nevertheless, the hot rolling with V_1 exhibits the highest load from a low thickness ratio. Other roll speeds are going the same according to their value, i.e. low values lead to load decrease.

11.1.4 Discussion and summary

Previous experiments investigated all controllable parameters for the hot rolling process with the rolling speed, the working temperature and the reduction ratio. Combining these three parameters leads to a performant foil manufacturing process to obtain the required products in terms of geometry and quality.

Reduction ratio and working temperature as main process parameters

The reduction ratio and working temperature combination represent the most critical parameter to control during the process. These parameters influence material deformation behaviour, as the reduction ratio imposes a deformation rate in both thickness and length directions, and working temperature reduces yield stress to perform the plastic deformation. In addition, a high reduction ratio tends to increase manufacturing process performance by increasing thickness reduction per pass and reducing the number of passes. Similarly, a working temperature increase improves the thickness reduction and optimises passes to reduce heat loss during each pass. Another interesting aspect of high working temperature is the formation of a surface oxide layer, which can be an advantageous element to avoid the sample sticking, especially for stainless steel material [126] and in this particular case, no use of external lubricant to decrease the friction coefficient. However, an excessive variation of both parameters could increase the number of structural defects on the foil and lead to process failure. High stress applied leads to edge cracks when the working temperature is too low, as highlighted in previous experiments. In addition, stress applied can affect the radius of the roll after several passes, which might conduct to roll deformation. This aspect is considered for numerical analysis with different roll radius equations, especially the Hitchcock radius formula, which calculates roll radius for each pass and according to rolling parameters and rolls mechanical properties [111]. Then, flatness and crown defects could be exacerbated by using too high stress during the process [127, 128].

Rolling speed as secondary process parameter

In addition to the reduction ratio and the working temperature, the rolling speed can be considered a secondary parameter according to previous experiments, especially for the measured load and the thickness ratio. Nevertheless, it can significantly impact the rolled products, especially for composite samples, as one performed here for U-10Mo bare foil manufacturing. As mechanical properties differ between different metallic materials and especially with temperature variation, the choice of the rolling speed leads to a specific strain rate applied during the process, which also depends on the reduction ratio during each pass. Different equations are available for strain rate calculations, which consider rolling parameters such as reduction ratio, rolling speed, or applied pressure [129, 127, 128].

Knowledge of this strain rate for each material combined with the plasticity initiation of composite samples has to lead to the same deformation rate for both to avoid hot rolling process failure. Then, heat loss during each pass could be reduced by increasing the rolling speed, with time reduction for the samples under the rolls. Optimisation of both parameters is then necessary for U-10Mo foil manufacturing.

Other parameters and potential ways for improving rolling process

Other parameters can be considered for the hot rolling process, such as friction between rolls and samples, external tension loads applied during entrance and exit of the sample, and then different geometry to homogenise the sample stress repartition. Application of algorithms and neural networks to improve and optimise the process could be necessary to take into consideration initial material properties from the previous processes in order to get a similar uranium foil with different manufacturing schemes [130, 131]. This method can ensure adequate repeatability for U-10Mo bare foil manufacturing even with different ingot characteristics, which can affect the process.

11.2 Hot rolling of assemblies with different characteristics

Previous experiments highlighted the influence of the reduction ratio, the working temperature and the rolling speed as parameters to control the hot rolling process. Experiments with monolithic samples were performed because of the simple set-up required and no other manufacturing process required for the rolling. However, these samples do not entirely represent the rolling of U-10Mo bare foils without internal interactions during the process inside the assembly. Indeed, the mechanical and thermal interaction of laser-welded lines is not considered for monolithic samples. As a reminder, monolithic refers to a block of the same material with the same properties in each sample area. The term assembly refers to an ingot encapsulated into a canister composed of a top lid cover and a housing sealed by LBW. Due to the restrictions inherent to uranium handling, rolling has been optimised with an inert material to have reproducible and safe experiments before rolling the U-10Mo ingot.

11.2.1 Difference between monolithic and welded stainless steel samples

Additional experiments are performed with assembled and monolithic samples to have a first range of adequate process parameters to roll U-10Mo ingot. Samples characteristics are similar to previous monolithic samples, with similar material and geometries for each. The hot rolling scheme used is similar for each pass, with the same heating time and working temperature, and load-deflection calibrated according to the previous experiments on a similar stainless steel alloy used. These experiments with welded assemblies are compared with monolithic experiments to establish potential similarities between monolithic and welded inert samples. This comparison will be used for further tests using only monolithic samples. Figure 11.7 and 11.8 show an example of a welded and rolled inert assembly sample at different stages in the rolling. Due to sensitive data regarding the manufacturing, welding lines are pixelised on welded assemblies.

Figure 11.7: *Welded stainless steel assembly after the rolling process with cracks*

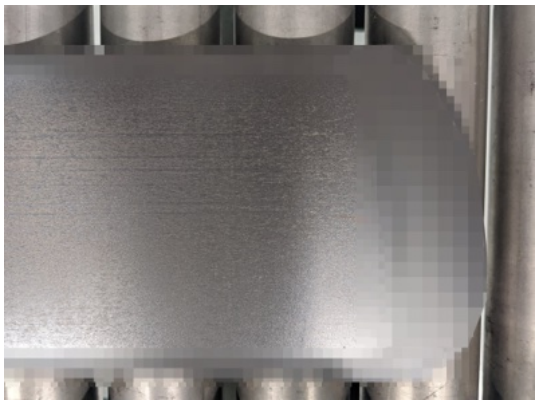

(a) First step of swelling

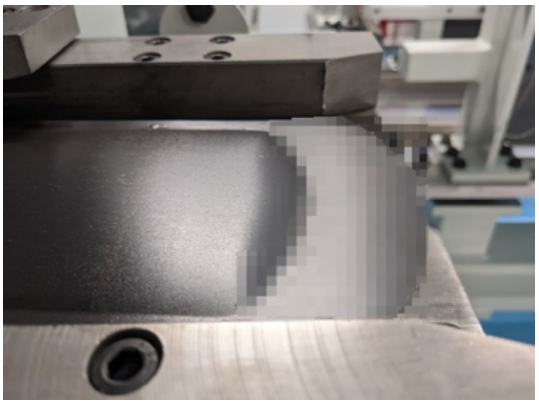

(b) Second step of swelling

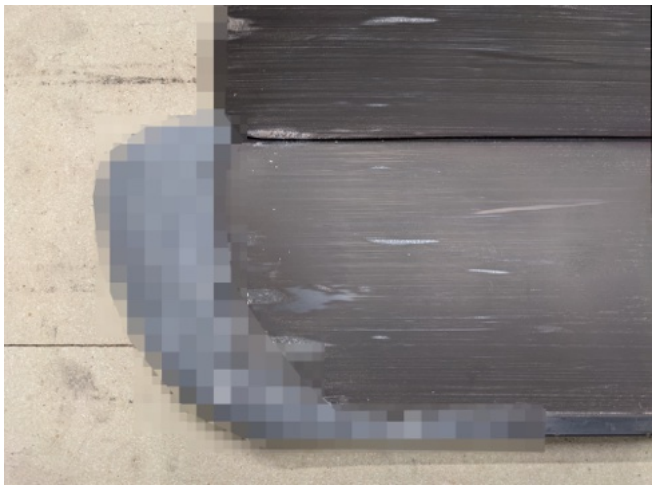

(c) Cover removed with internal foil

Figure 11.8: *Swelling stages of rolled stainless steel welded assemblies*

The most striking aspect is the swelling of the top lid cover on the ingot area. Few air bubbles are visible on the right and left edges of the swelling, with delamination of the top lid cover in the length-wise direction. Figure 11.8 depicts different assembly shapes following rolling passes. At the end of the hot rolling process, the top lid cover is delaminated from the canister, with the inside foil removable. Further, for the hot rolled sample at the working temperature T_2, no cracks on edges are visible, and rolling was performed with a good parallelism shape, with low deformation into a parallelogram shape. The most striking result from Figure 11.8 is the increased swelling on top of the ingot area and visible delimitation between the stainless steel canister and encapsulated ingot, especially on the edges. Cracks of welded area are visible on the transition between the ingot and the welded area of the canister at the bottom part. These cracks deteriorated pass after pass as illustrated by Figure 11.8 - (a) and (b).

If we now turn to measured load, Figure 11.9 compiles the load ratio measured during experiments between six welded assemblies and six monolithic samples. The thickness ratio is set for the x-axis in place of the reduction ratio to follow the entire thickness reduction process of the assembly during the rolling.

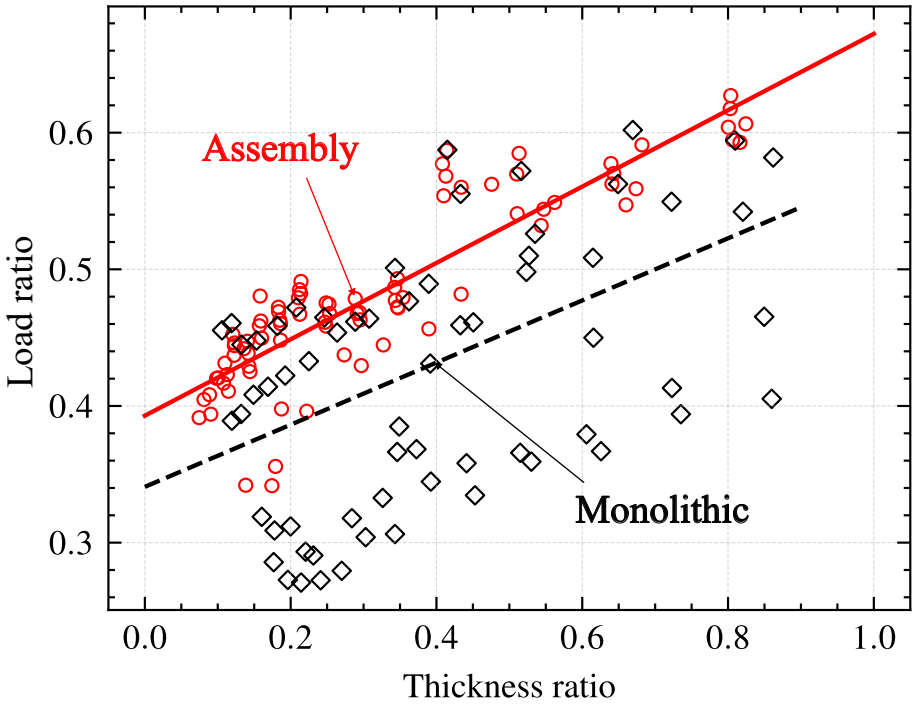

Figure 11.9: *Load ratio comparison between stainless steel monolithic and welded inert samples as a function of thickness ratio*

The plot follows a similar linear trend as depicted in Figure 11.5, with the load ratio measured according to the reduction ratio. The most striking aspect is that monolithic samples seem to be easier to roll compared to welded assemblies, with lower values of load measured. One possibility for this load difference can be the absence of frictional contact inside monolithic samples compared to the assembly. The ingot is in contact with the canister and rolled in the welded assembly thanks to the differential friction contact and tangential loads between both materials. Experimental measurements also highlight that monolithic measurement points are mainly located on both sides of the black-dotted linear curve. One seems to have a similar load value to the assembly when a 0.1 load ratio sets down the others. Different reasons could be at the origin of this difference, such as different mechanical properties or different manipulations during the process. In a global overview, load values for monolithic samples are lower than for assemblies. Welded assemblies require more stress to perform the same rolling process than monolithic samples.

11.2.2 Composite material rolling: titanium and nickel alloy ingots

U-10Mo bare foil manufacturing involves rolling composite elements with different properties during the entire process between the uranium ingot and the metallic canister used. This part describes experiments conducted with dissimilar inert materials for canister and ingot. Loads, foil thickness and behaviour under loads, defects formation and final rolled foil properties are investigated with these dissimilar properties on hot rolled composite samples. These aspects are studied for further use in U-10Mo bare foil manufacturing. The first experiment was conducted with titanium ingot into stainless steel canister, and then, stainless steel canister was used with nickel alloy ingot.

Titanium alloy ingot with stainless steel canister

The first batch of sample experiments with the titanium ingot into the stainless steel canister is performed with two samples and two different laser welding schemes for ingot encapsulating. The hot rolling process is performed with the same working temperature T_2 and heating time as previous stainless steel assembly samples. A similar reduction ratio between 20 to 5 % per pass is applied for thickness reduction, and the load-deflection configuration remains the same as for the previous stainless steel samples. Figure 11.10 illustrates the results of the first rolling of the titanium ingot with a first laser welding scheme.

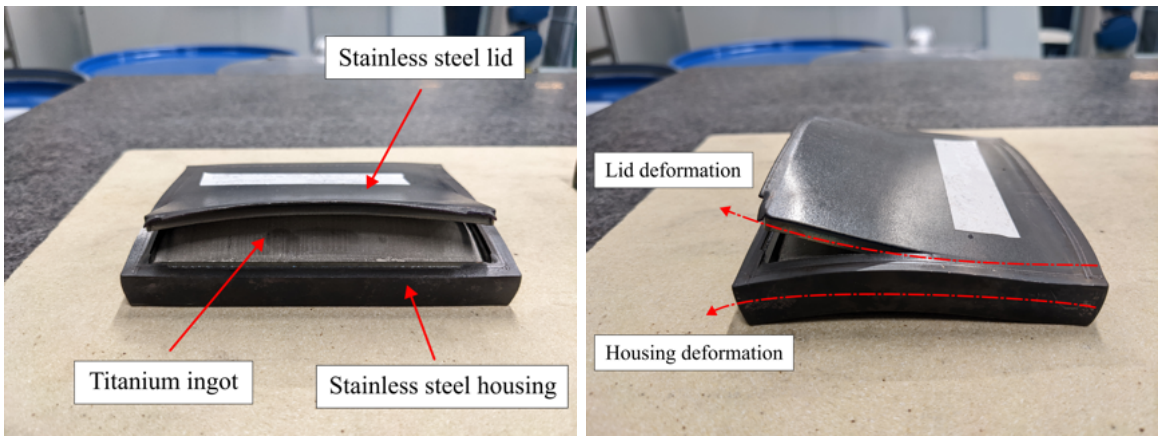

Figure 11.10: *First titanium sample into stainless steel canister with first welding scheme*

The top cover lid delamination is fully visible after two rolling passes of the assembly. Weld beads produced by laser welding are entirely dislocated from the bottom part of the assembly. The interesting aspect is the shape of the titanium ingot inside the canister and the top cover lid orientation after the mechanical failure. The ingot length-wise side pushes the stainless steel in the rolling direction. The visible curved part confirms this tendency to push the stainless steel. Figure 11.10 shows the assembly edge profile and exhibits the same behaviour as previous samples with top lid cover deformation by following the roll shape.

(a) Top-view

(b) Side-view

Figure 11.11: *Second titanium sample with second welding scheme*

Figure 11.11 depicts the second titanium sample with another welding scheme process to avoid cover delamination during the first pass, as occurred for the first sample. Nine passes were performed to roll this sample, with a load ratio measured between 0.46 to 0.58. The high curvature of the foil is visible, as seen in Figure 11.11 - (b). Typical orange-brown oxidation of titanium is visible on the foil. The most striking aspect is that the foil inside the canister is not removable due to material accumulation on one edge of the assembly, as exhibited on the right edge of Figure 11.11 - (a). This part of the ingot seems to push the stainless steel edge in one direction during the rolling, as layers can be distinguished on this side. The same aspect is slightly visible on length-wise edges where the titanium ingot seems to be enclosed in the stainless steel housing part, where the lid and the housing are linked together. The temperature T_2 used for rolling has decreased titanium yield stress lower than the stainless steel canister. This decrease is due to β transition of titanium which happens for T_2 [36]. Titanium deformation appears first compared to the stainless steel canister leading to cracks and delamination of the top lid cover, with pushed material on one side of the assembly.

Nickel alloy ingot with stainless steel canister

Regarding the nickel alloy ingot, a different pattern than the previous titanium sample is visible in Figure 11.12. Three passes were performed to roll this sample, with a load ratio measured between 0.76 to 0.79 and with a working temperature of T_2. Compared to the titanium sample, the curvature of the assembly is on the opposite side. The top cover lid delamination is still visible on the sample, with the same ellipsoidal deformation characteristics from the rolling process on the edges. Cracks are also visible on both edges of the rolled sample. For this experiment, the nickel alloy ingot does not push the stainless steel canister like the titanium ingot. The curvature tends to highlight a deformation of the canister prior to the nickel alloy ingot. The deformation of welded area located on the canister prior to the lid area with the rest also argues for an early canister deformation. Interestingly, the length-wide sides of the samples seem to have a higher curvature than the titanium or stainless sample rolled before. This curvature could be explained by a higher deformation rate in these areas, confirming the canister deformation assumption before nickel alloy ingot deformation.

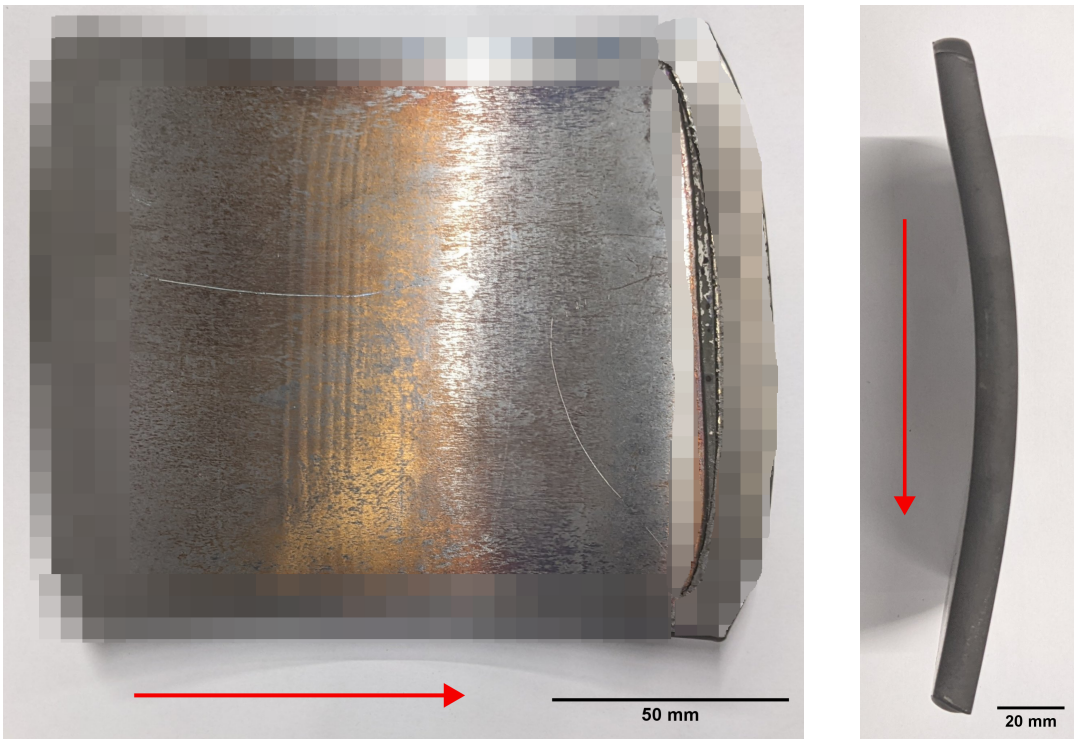

(a) Top-view (b) Side-view

Figure 11.12: *Ni alloy ingot into stainless steel canister / Red arrow: rolling direction*

11.2.3 Discussion and summary

Hot rolling of inert material with different characteristics as monolithic, welded or composite material gives an interesting rolling parameter database for U-10Mo bare foil manufacturing. Comparison between monolithic and welded assemblies was performed to extract similarities and differences to improve further experiments with uranium samples and to highlight the importance of canister design, its machining and the material choice.

Rolling of monolithic and welded assemblies

Experiment results suggest that the load ratio measured between monolithic and welded samples is slightly different. Welded assemblies need more load to be rolled with the same rolling parameters than monolithic samples. One explanation might be the additional contact stress between the ingot and the canister, in addition to the initial friction value of the sample, which increases the load measured. As no external lubricant is used due to potential liquid contamination with the uranium ingot, the entire rolling process is feasible thanks to a differential friction coefficient between rolls and rolled assembly. Oxide layer formation might be, in this case, a helpful added element to increase this differential friction coefficient [126].

Another explanation is that assembly manufacturing involves the laser welding process. Cracks and delamination initiation appear on weaker canister areas, mainly on thin welding areas of the lid cover. Laser welding beads produced are the only mechanical support for the assembly to handle the hot rolling pressure, which can lead to the heterogeneous distribution of stress on the sample. Different solutions could be implemented to increase the mechanical tenacity of welded areas, such as increasing laser welding areas to have a better distribution of hot rolling stress on the sample or increasing lid thickness on weldable areas to increase global lid mechanical load. Nevertheless, this last solution will have a limit due to the power of the laser source, which usually allows only one to two millimetres of thickness [87].

Canister design and material choice

The choice of canister material is crucial for U-10Mo bare foil manufacturing as the mechanical properties of both canister and ingot must be similar to avoid unanticipated delamination. Strategies to enhance the hot rolling of composite material involve a good knowledge of both plastic deformation properties of the assembly materials, including the specific geometry of the initial canister. A faster deformation of the ingot, as illustrated with the titanium in section 11.2.2, or the canister with nickel alloy ingot leads to cracks and cover delamination. Manufacturing solutions and adapted ingot size to the canister housing can reduce delamination and cracks.

Another solution to reduce faster deformation of the canister or ingot is to control the rolling speed during each pass according to other rolling parameters. The rolling speed variation influences the strain rate and the deformation speed. Consequently, stress yield for plastic deformation is affected by the strain rate. The working temperature is another parameter to obtain similar material properties between the ingot and the canister in the composite rolled assemblies. Higher temperature leads to a higher strain rate dependency on assembly deformation, which might be interesting to control the plastic deformation and set the desired value according to the materials rolled. About the canister design itself, the difference in thickness of different assembly parts, with thick ingot and canister bottom part with thin weldable areas on the lid, are leading to different deformation. These different deformation rates are due to different volumes to reduce between thick and thin parts, with potential delamination and process failure. Designing these parts by considering volume deformation might be an appropriate solution to resolve delamination issues and have a better load distribution. Finally, an appropriate system to push samples into the rolling stand to avoid a parallelogram shape might be another solution to improve the overall process and avoid delamination. Indeed, this specific shape leads to different sizes of each rolled assembly edge, especially on welded parts. After numerous passes, this shape breaks one of the edges due to dissimilar size and exacerbates the load required to keep the lid welded to the canister.

11.3 Rolling of U-10Mo ingot samples

This section highlights experiments with a U-10Mo ingot encapsulated into a stainless steel canister. Appropriate laser beam parameters and welding schemes for ingot sealing were selected according to the previous inert experiments. Rolling parameters investigated in the section before were also used to perform U-10Mo bare foil rolling. During the process, the working temperature is maintained constant at T_1, with an enough heating time per pass to heat the ingot to T_1, and a constant reduction ratio. Rolling mill load-deflection is calibrated with similar stainless steel material. Tools for experimental results obtained during these experiments are depicted in section 10.3.

11.3.1 Visual aspects of rolled samples

Surface aspects and defects of rolled assemblies

This part focuses on inspecting hot rolled assemblies before U-10Mo bare foil decaning. Surface layer condition, potential waviness of the assembly, defects on the metallic canister and other visual aspects are investigated. In addition, unsuccessful samples are also analysed to study the potential reasons for hot rolling failure.

(a) Welded assembly overview after hot rolling process

(b) RX-ray transmission pictures of U-10Mo foil (in black) in stainless steel canister (in grey)

Figure 11.13: *Successfull U-10Mo welded assembly rolled*

Figure 11.13 shows a successful hot-rolled U-10Mo rolled assembly. At the end of the process, the final assembly length is around 12 to 14 times longer than the initial length. Width does not increase as much due to the preferential deformation in the length direction compared to the width direction. Usually, the width increases by an average of 10 % at the end of the rolling process. The canister surface is coated with an oxide layer due to working temperature.

This layer is similar to the inert samples presented in part 11.2.1 and Figure 11.7. The right and the left edges constitute interesting areas to investigate. Indeed, as no void is set into the canister by sizing the ingot to housing size, the delimitation between the U-10Mo ingot and the metallic canister is visible, with tight swelling on both edges. This swelling is visible only on the sample's face where the lid cover seals the canister. Weld beads visible from the LBW process disappeared from the rolled assembly. The parallelogram shape is also visible at the edges of the foil. This phenomenon is due to the misaligning of the assembly for the first passes due to the low length value of the sample and then the difficulty in pushing it between rolls. This parallelogram shape is then tried to be corrected by pushing the shorter long edge under the rolls to obtain a rectangular shape. Finally, the curvature appears due to residual stress and frictional contact between the U-10Mo ingot and the canister during the rolling process. Welded lines contribute to this curvature shape with high stress around the laser weld beads.

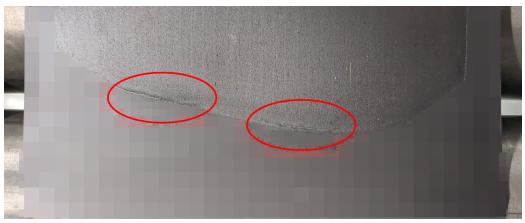

(a) Width-wise necking initiation

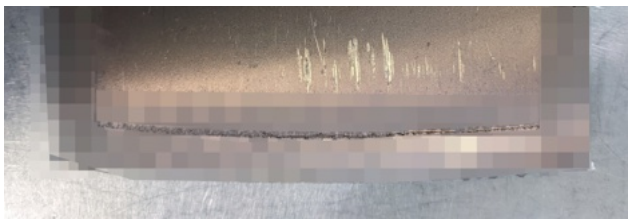

(b) Width-wise crack along weld bead

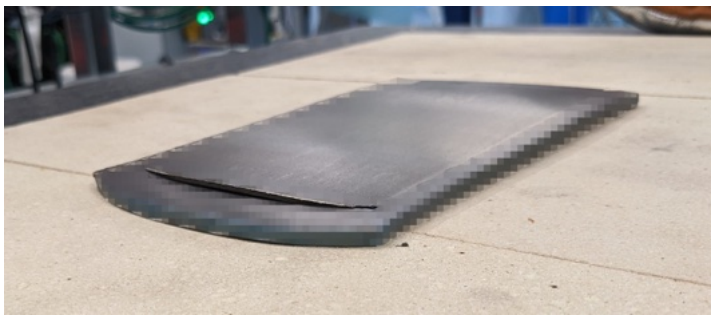

(c) Unsuccessful rolling with cover delamination

Figure 11.14: *Width-wise crack on U-10Mo assemblies during hot-rolling*

Rolled assemblies that did not achieve the thickness targets are subject to cracks appearing in the width-wise direction, i.e., cracks in the left and right edges. After a few passes, width-wise necking appears around the welded lines in the transition area between the ingot location and the welded area, as shown in Figure 11.14 - (a) and (b). Cracks occurred with successive increases in pass number and load applied to the sample. These defects lead to cover delamination, as shown in Figure 11.14 - (c), which leads to the end of the rolling process.

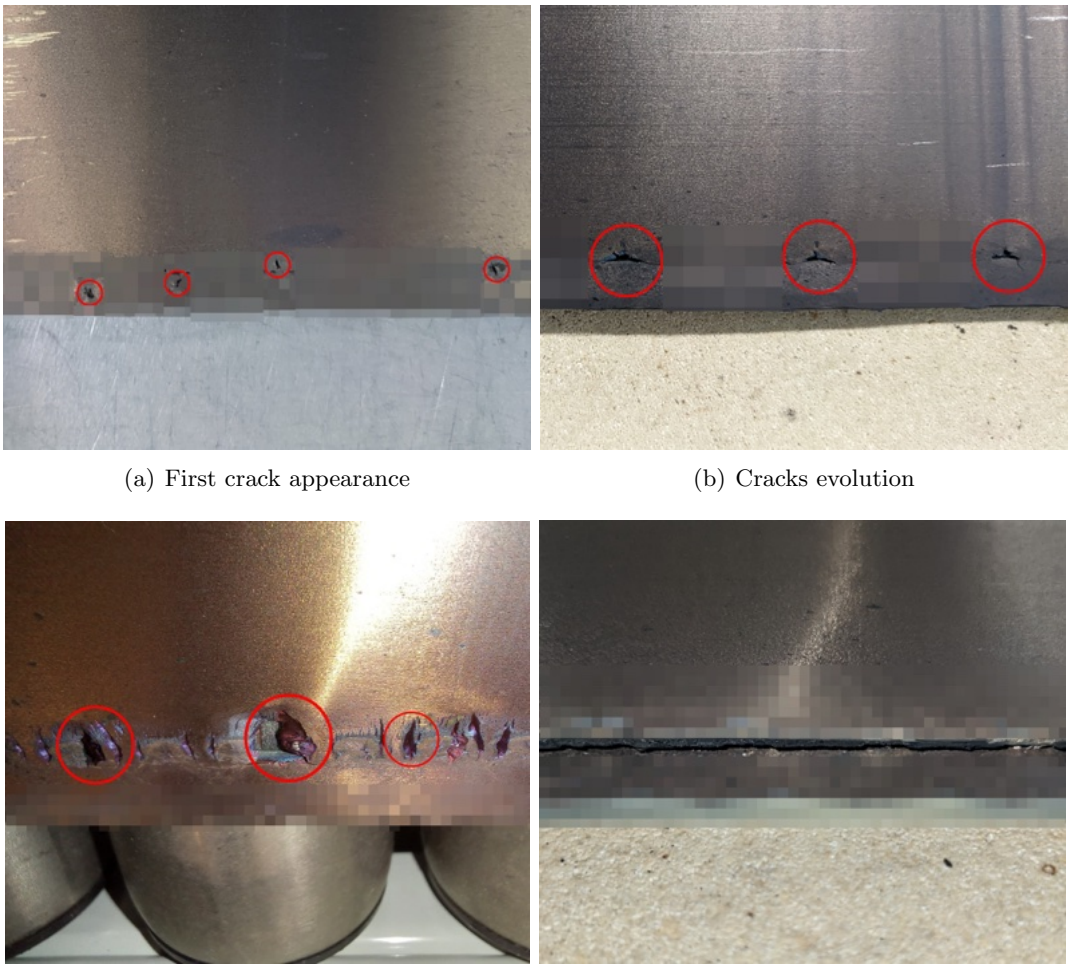

(a) First crack appearance

(b) Cracks evolution

(c) Cracks collapse

(d) Cover rupture and canister delamination

Figure 11.15: *Length-wise cracks evolution stages for U-10Mo assemblies during hot rolling*

In addition to width-wise defects, length-wise cracks also appear during the hot rolling process, leading to canister delamination with different crack steps. During the rolling process, a few hot rolled assemblies were subject to crack appearance. Figure 11.15 highlights this evolution. The first step consists of areas with necking, with in a few cases, the little void around the laser weld bead as shown in Figure 11.15 - (a). Usually, this happens for a thickness ratio between 0.9 to 0.8. The second step is crack evolution by metallic rupture on the welded area, especially on the transition between the thin and the thicker area of the canister top lid cover. The third stage consists of profound increases for existing cracks from the previous rolling passes and still along weld beads. Finally, the last stage consists of delamination and total rupture of the canister top lid cover with its housing, which conducts to the end of the process to avoid contamination and potential rolling mill damage. The shearing of welded areas is visible and mainly impacted by cracks. It conducts finally to the top cover lid delamination as shown in Figure 11.15 - (d).

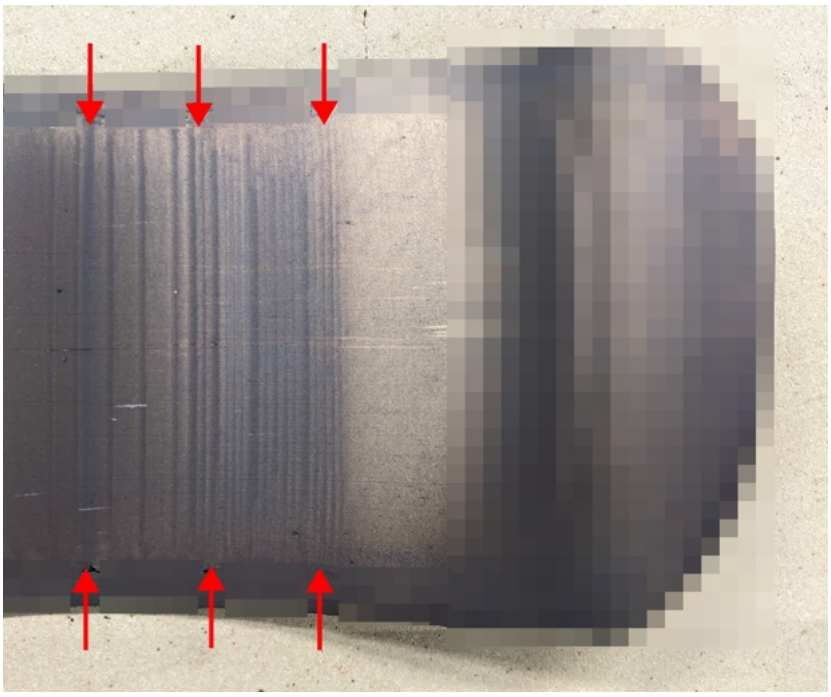

Figure 11.16: *Skidding impact (red arrows) on U-10Mo hot rolled assembly*

Finally, the skidding during the rolling process also impacts the final foil produced and could lead to cracks and assembly delamination. Skidding for flat rolling is defined as a non-negligible speed differential between the entrance and exit speed of the rolled sample. This differential value occurs due to different surface properties and tribology between rolls and samples, which affect thickness deformation. This variation affects the deformation speed locally: the local area on the top and the bottom of the assembly will deform at different speeds, which conducts to foil defects and, in this case, assembly delamination. This defect is visible in Figure 11.16 with straight vertical lines, illustrating different deformation fronts. They conduct here to severe curvature and, in the worst case, to the assembly delamination. The control of the skidding, in addition to the U-10Mo ingot adjusting to avoid necking and cracks, allows the success of the rolling process.

Inspection of extracted U-10Mo bare foils

After visual inspection of the rolled assemblies, U-10Mo bare foils are extracted by laser cutting and characterised for future improvements. The bare foils are similarly investigated with visual aspects as rolled assemblies before into a glovebox with a controlled atmosphere. These investigations are performed for both bare foil categories, i.e., with thickness target achieved and non-achieved. As a reminder, U-10Mo bare foils with non-achieved thickness are still usable: this term means that the thickness needed for PVD coating is too high, so these foils must be cold-rolled to obtain the required thickness, usually less than 0.06 thickness ratio. Two batches were realised with different welding schemes to avoid assembly delamination before the thickness target, which explains the different bare foil thicknesses.

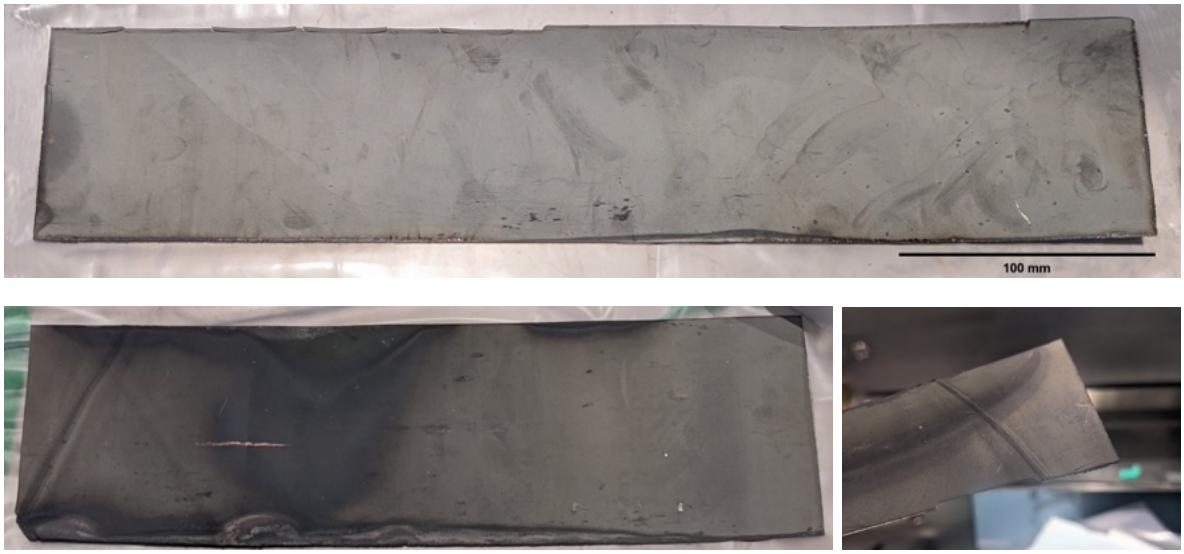

Figure 11.17: *U-10Mo bare foils extracted with thickness target non-achieved*

Figure 11.17 shows U-10Mo bare foils with a non-achieved thickness target removed from the canister by LBC. Dissimilar surface aspects with a black-to-grey scale gradient are visible with additional edge burns on extracted foils. These different surface aspects can be explained by oxide layer formation combined with dissimilar contacts of uranium ingot with the canister during the rolling process. High-temperature gradients during the process could also affect the surface condition with oxide formation and potential high carbon content from the initial casted ingot. Many scratches are also randomly distributed on the bare foils, mainly on the edges, with one exacerbated on the bottom foil. These are due to frictional contact with the canister and wrong manipulations during manufacturing, especially during laser cutting with scratches caused by friction with the laser cutting table. Over-thickness of bare foils is measured on some random spot, as shown on the right of the bottom U-10Mo bare foil. Corners could be lost during the laser cutting and extraction, as shown in the bottom foil on the left from Figure 11.17. This does not represent an issue with LBC to resize the foil.

Moving on now to consider U-10Mo bare foils with thickness target achieved by hot rolling process. Figure 11.18 depicts bare foil samples cut by LBC extracted from stainless steel canister and resized for future plate manufacturing process. These bare foils are ready to send for PVD coating, with holes made on both edges for fixation during the PVD process.

(a) Top surface of U-10Mo bare foil

(b) Bottom surface of U-10Mo bare foil

Figure 11.18: *Global aspect of U-10Mo bare foil with thickness target achieved*

The surface gradient aspect of U-10Mo bare foil looks differently compared to the previous bare foil from Figure 11.17. Mainly three areas are visible: shiny, dark mat and golden. The gold represents the oxide layer formed on U-10Mo alloys during the process. Shiny and dark areas are also randomly located along the foil, with a higher tendency to be visible on the bottom foil, which is in contact with the canister housing. These differences in surface colour can be explained in the same way as bare foils from Figure 11.17 with a variation of surface contact during rolling with the canister. Compared to bare foils with non-achieved thickness targets, shiny surfaces could be at this process stage due to prolonged contact at high temperature and pressure with stainless steel canister, with differential chemical compositions.

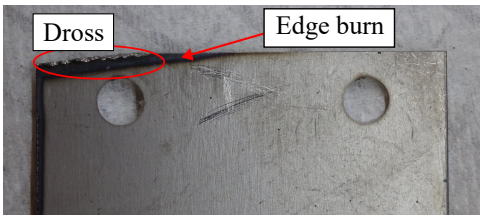

(a) Edge burns and dross

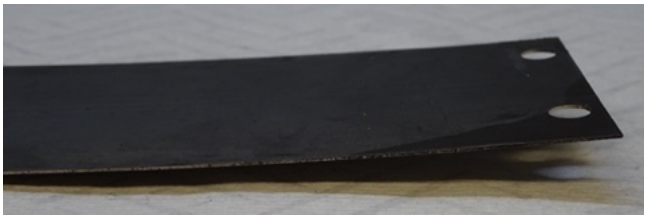

(b) Bare foil curvature

Figure 11.19: *U-10Mo bare foil defects after canister removing*

Defects, burns and cracks are still visible, similar to previous U-10Mo bare foils in Figure 11.19, with less quantity of them alongside the bare foil. In addition, the waviness tends to increase slightly due to a lower thickness on the bottom edge part, as shown on 11.19 - (b), with slight waves in the middle of the foil. Then, dross sticking is visible on the top left of the foil edge in Figure 11.19 - (a).

11.3.2 Experimental measurements of thickness and foil waviness

Both thickness and waviness measurements have an essential role in addressing the issue of mandatory requirements for other manufacturing processes and neutronic behaviour in the reactor. As U-10Mo bare foil inside the canister is not measurable during the rolling, final measurements are needed to modify the process if needed.

Thickness measurements

Thickness measurements were performed on five U-10Mo bare foils ready for the zirconium coating by PVD process. One of these foils was measured with 37 points using a micrometre in length direction alongside three rows A, B and C. Foils length measured here is set to an average of 720 mm with an average thickness of 0.43 mm. These rows are constantly separated from the top to the bottom in the width direction. Five measurement points were taken alongside the other foils. Figure 11.20 plots the measured data.

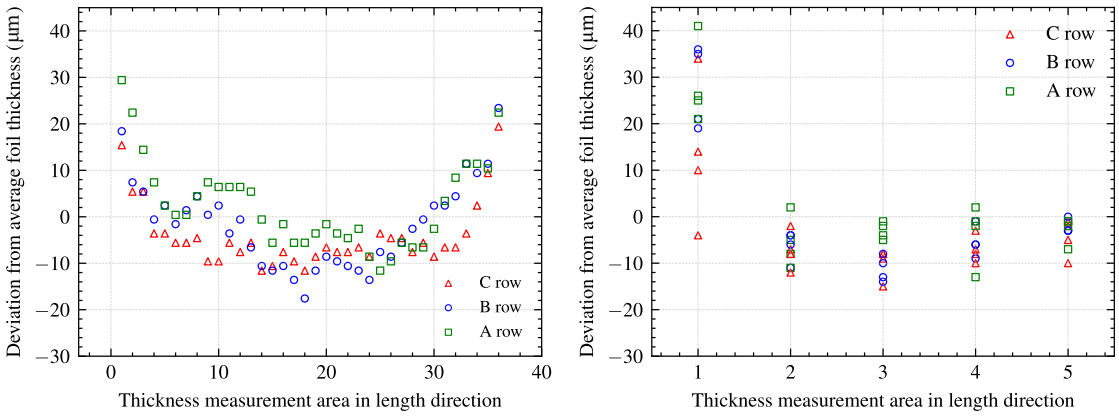

(a) U-10Mo bare foil with 111 values

(b) U-10Mo bare foil with 15 values each

Figure 11.20: *Thickness measurements from U-10Mo bare foil ready for PVD coating*

These plots do not provide raw measurements but deviation from the average thickness measured with raw values. The first interesting aspect is the deviations from -15 to 30 µm along the foil. Two areas are distinguishable, with a strong positive deviation on the right and left sides of the bare foil, while the thickness in the middle remains almost constant. Values over zero are scattered on the U-10Mo bare foil edges, i.e., respectively, from measurement points 1 to 10 and from points 30 to 37 in Figure 11.20. The increase in thickness at the edges is of interest here compared to the bare foil centre thickness. This behaviour is characteristic of rolling, which is called dog-boning. Then, from points 10 to 30, the thickness measured is constant alongside the bare foil before growing up to the rest of the measured points. The same phenomenon happens for the bare foil with 15 values, with a thicker area from points 1 to 2 to reach a deviation of 40 µm. Other measurement points remain constant to -10 µm.

Waviness profile

Foil waviness appears during the hot rolling process due to variations in stress applied, specific handling or different local thickness. Waviness measurements were realised with a conductivity sensor. The area of measurements was taken in the same way as the previous thickness measurement, i.e., alongside the bare foil with additional left and right edges and the foil centre was taken as the reference point. During measurements, the sensor in the z-axis is decreased to touch the foil surface until it receives a signal: the difference between the start position and z-axis value when the sensor receives the signal corresponds to the waviness value. A positive value means the wave is on the top and negative on the bottom. Measurements were realised on two U-10Mo foil removed from the canister with an average length of 350 mm and only hot rolled. The results are presented in Figure 11.21.

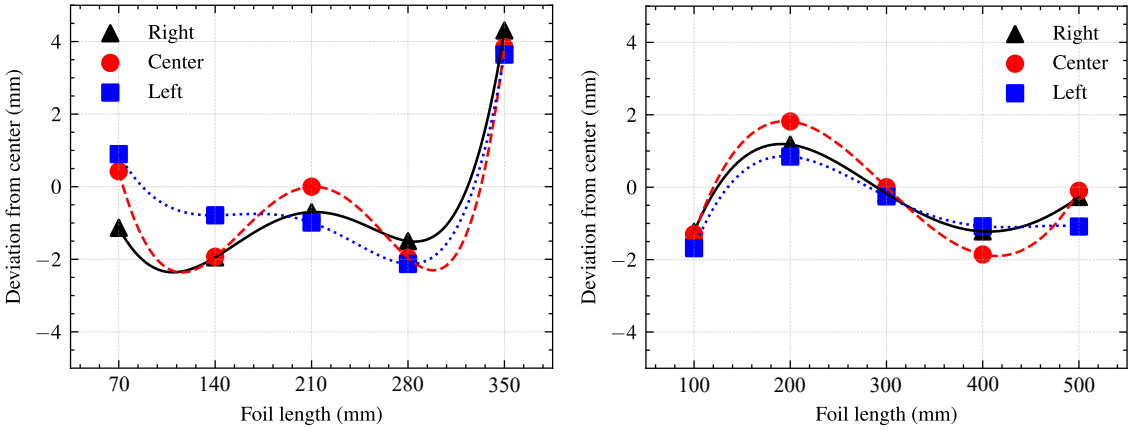

(a) Thickness ratio : 0.135

(b) Thickness ratio : 0.105

Figure 11.21: *Waviness profiles of two U-10Mo foils with different thickness ratios*

Both waviness profiles share several key features. Profile for both U-10Mo bare foils do not stay constant and vary around 2 mm up and down, except for point 5 from Figure 11.21 - (a) with a measured peak to 4 mm. Interestingly, an interaction of waviness and thickness reduction could be observed. The waviness of the foil decreases when the foil thickness decrease. In addition, for each measurement, the right and left parts are more wavy than the rest of the foil. Extremum values are located on both sides of U-10Mo bare foils, with mostly constant variation from the reference centre between the right, middle and left sides. A potential cold rolling process substep can resolve these issues of waviness to improve flatness, with additional heat treatment under loads or laser cutting of both sides to remove wavy parts.

11.3.3 Experimental measurements during hot rolling process

Load measurements

The load applied to the rolled sample was measured and plotted on the user interface to control the process after each pass. Investigating load applied for different thickness ratios is a continuing concern within the improvement of foil manufacturing as these data are relevant to reduce unexpected defects. The load measured is summarised in Figure 11.22 for respectively total and individual load applied on each sensor, i.e., the top and the bottom part of rolled foil in the width direction.

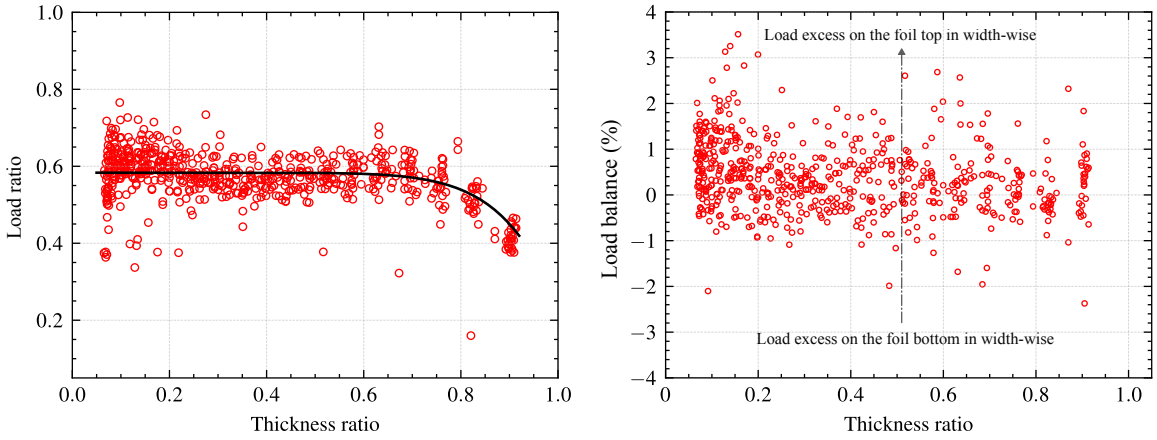

(a) Total load applied

(b) Load balance from total load applied

Figure 11.22: *Load ratio measured according to* $t_{\%}$ *during the rolling process of U-10Mo assemblies with similar temperature and reduction ratios during each pass*

The correlation between the total load applied with the thickness ratio plotted in Figure 11.22 - (a) highlights two interesting areas. Results highlight no variation in the total load ratio from 0.6 to the lowest thickness ratio value. It stabilises around 0.6. Then, for the second area, the load applied increases from 0.6 to the rolling scheme start thickness from 0.4 to 0.6 in load ratio. These results suggest that a low work hardening of the material is depicted, despite the potential presence of carbides inside the material, which tends to harden the sample. The working temperature selected for the rolling scheme allows performing the process until the thin foil is rolled without increasing the load applied.

On the other hand, optimisation in load applied to the material should be performed to increase assembly reduction and decrease manufacturing time for bare foil rolling, especially after a thickness ratio of 0.6. Regarding Figure 11.22 - (b), the results indicate that the stress applied mainly deviates from 0.5 to 1 % on average to the front sensor. This deviation is insignificant for foil produced, especially for hot rolling, and no visual deviation as curvature shape was visible for the U-10Mo assemblies rolled.

Thermal measurements

Rolled assemblies lose heat by convection with the external atmosphere, conduction contact with rolls, and support from the rolling mill machine during the process. As the rolling mainly depends on working temperature for the load applied and thickness reduction, adequate control and knowledge of heat loss tendency represent essential input data for further rolling improvement and U-Mo bare foil industrialisation.

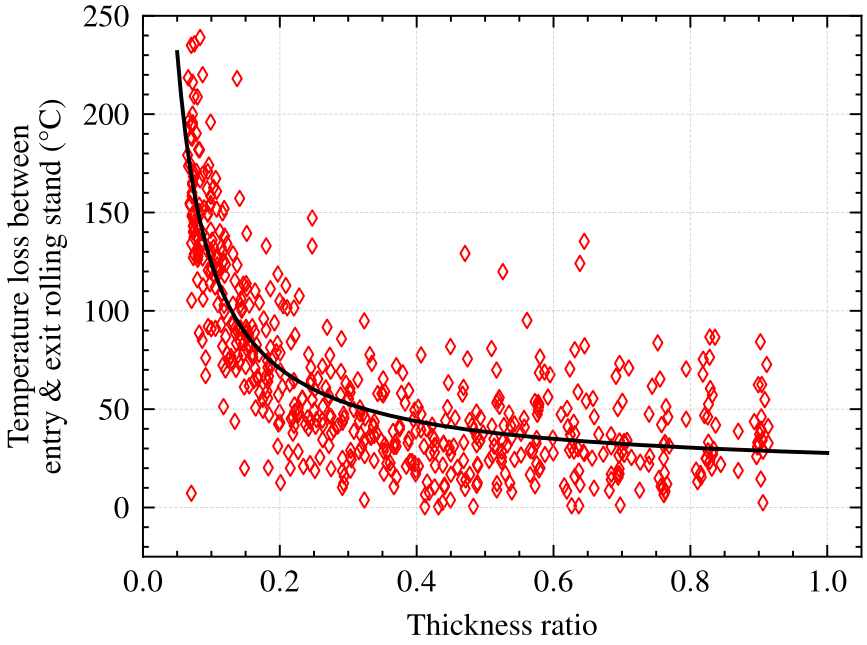

Figure 11.23: *Temperature loss between the entry and the exit of the rolling stand according to* $t_{\%}$ *for U-10Mo assemblies with similar temperature and rolling schedule*

Temperature loss occurred with successive decreasing of the thickness ratio, i.e., decreasing thickness achieved by the rolling process. The fitting curve shows a linear heat loss from 1.0 to 0.6 thickness ratio, with a low slope coefficient, in a range of temperature loss per pass between 30 to 40 °C. What can be seen in Figure 11.23 is the rapid increase of temperature loss starting from 0.4 thickness ratio for a temperature loss per pass of 200 °C. As the assembly is reduced in thickness, the time spent under the roll for the sample increases with the length increase. This increase in time with increased surface allows a higher exchange contact between rolled assembly and rolls and a longer contact time between both elements. This explains this phenomenal growth of temperature loss. Nevertheless, the fitting curves with temperature measurements do not represent the actual heat loss of the U-10Mo ingot but the heat loss of the assembly at its surface. In addition, the surface condition of the sample changes after numerous passes, which affects sensor detection as they are surface sensitive.

11.3.4 Microstructure, hardness and diffusion characterisation

Microstructure comparison between U-10Mo ingot and hot-rolled foil

The microstructure of the ingot is first investigated and compared to U-10Mo bare foil produced to give an overview of structural composition, carbide distribution and potential inclusions or casting defects. From the U-10Mo ingot, four samples were cut with the sawing machine at 1 cm depth on each corner according to Figure 11.24. After raw observations, samples are etched to exacerbate the microstructure. The composition of the etching solution consisted of a mix of 5 mL HF (65 %), 20 mL concentrated HNO_3 and 20 mL Glycerin (85 %). All samples were covered with the solution for 10 seconds and then rinsed with water to end the etching process. The structural characterisation of specimens is carried out with an optical microscope and SEM. When chemical compositions were provided, EDX was used for the analysis.

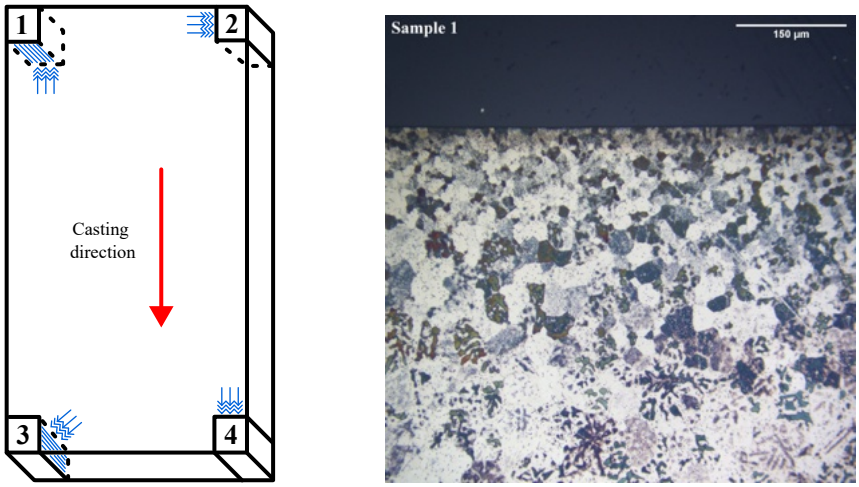

Figure 11.24: *Ingot cutting scheme for microstructure analysis with a SEM picture from sample 1. Red arrow: casting direction - Blue: investigated area*

Sample 1 from Figure 11.24 highlights strong evidence of different microstructures between the centre and the border of the ingot. The sample border has a finer grain structure than the most central part of the sample showing an increase in dendritic cast structures, with arms up to 100 µm length as shown in Figure 11.24. Table 11.1 summarises the length of these transition areas. Values measured are similar for samples 1, 2 and 4, with a lower transition area for sample 3, possibly due to different casting cooling.

Samples	1	2	3	4
Transition length	263 µm ± 48	318 µm ± 30	168 µm ± 12	285 µm ± 27

Table 11.1: *Values of fine-grain structure area in U-10Mo ingot*

Strong anisotropy is so revealed by region extends of fine-grain microstructure. It could affect both final thermal and mechanical properties. Regarding differences in the chemical compositions sample, Figure 11.25 shows different greyscale levels for different proportions in uranium and molybdenum, with in comparison pictures taken before etching.

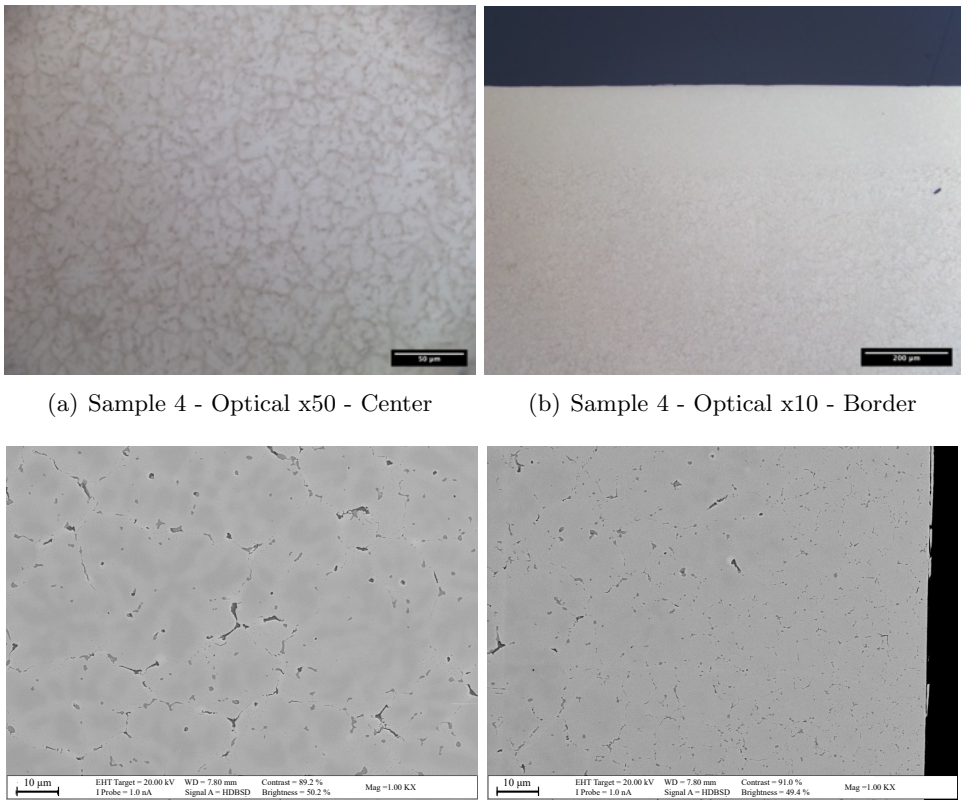

(a) Sample 4 - Optical x50 - Center

(b) Sample 4 - Optical x10 - Border

(c) Sample 4 - SEM x1000 - Center

(d) Sample 4 - SEM x1000 - Border

Figure 11.25: *SEM and light pictures comparison on centre and border of U-10Mo ingot*

SEM pictures from Figure 11.25 illustrate that the middle region exhibits precipitations of lower uranium content than the matrix at the border of the dendrites, which can be identified as uranium carbides. Few larger structures with the darkest greyscale were found to be highly Mo-rich, a synonym of molybdenum segregation due to the casting process. Indeed, molybdenum-rich melt crystallises first, leaving uranium-rich melt to crystalise in the outer regions of the dendrite. EDX analysis shows a delta in molybdenum concentration of 9 wt.-% between the grain centre and dendrite extremities. For the border regions, the contrast in greyscale is lower than in the centre, indicating no segregation in this region. Precipitates still appear, but they are more scattered, and the distance between them is smaller compared to the middle region.

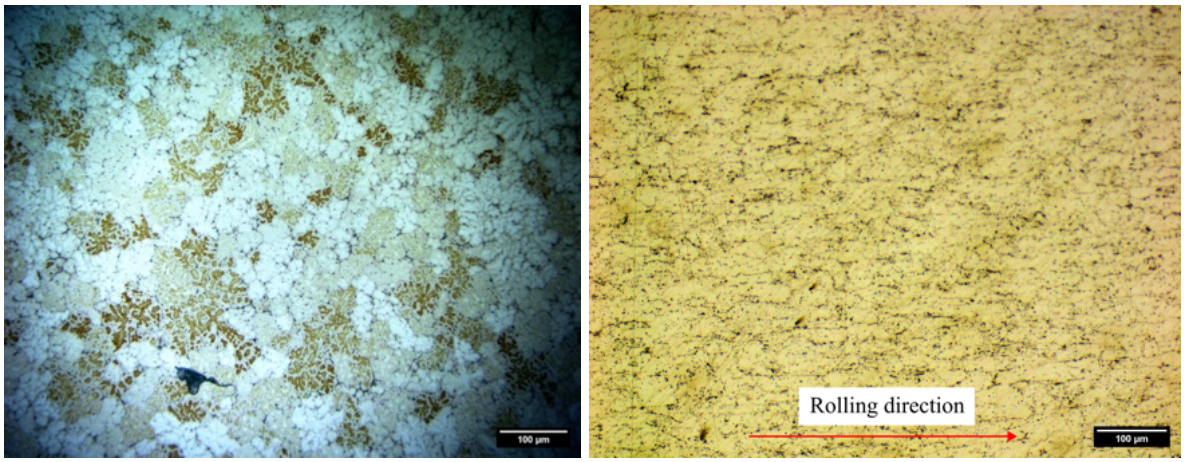

(a) Ingot microstructure under optical microscope (b) Foil microstructure under optical microscope

Figure 11.26: *Analysis of microstructure of U-10Mo ingot and hot rolled bare foil*

It can be seen by comparing the two results of ingot and foil microstructure from Figure 11.26 that grains are mainly deformed in the rolling direction, i.e. from left to right, for foil microstructure compared to initial ingot. In addition, uranium carbides localised around grains are still randomly distributed around grains for foil microstructure. Contrary to the ingot, no inclusion is visible on the foil, where one is visible in the bottom left of the picture. This inclusion could indicate the possibility of some also in the foil, in small quantity, due to casting defects.

Hardness

Hardness measurements of U-10Mo in ingot and bare foil according to different manufacturing schemes were performed to characterise the mechanical properties of U-10Mo material and potential differences between the casted ingot and bare foil produced. Measurements were realised on different sections of the sample, both cross and flat. Figure 11.27 illustrates how hardness measurements on different samples look from an optical microscope. Mechanical polishing was performed with a polishing load value as low as possible to avoid surface mechanical tension and achieve reproducible hardness values. The experimental procedure for hardness measurements is depicted in material and sections 10.4.

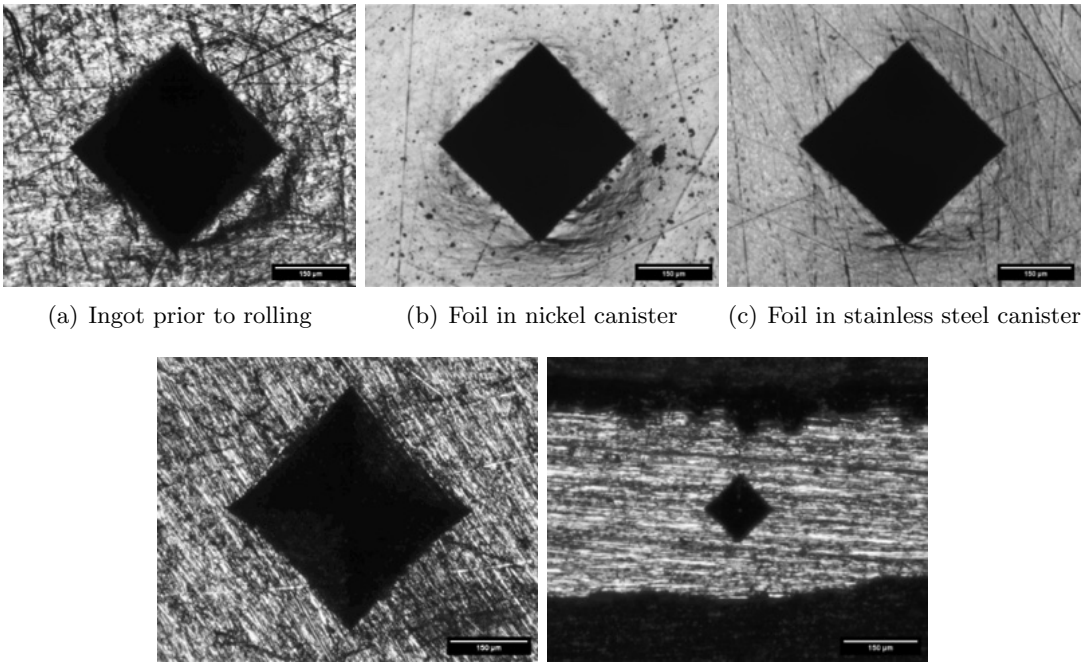

(a) Ingot prior to rolling (b) Foil in nickel canister (c) Foil in stainless steel canister

(d) Extracted foil flat surface (e) Extracted foil cross-section

Figure 11.27: *Hardness mark samples performed on different U-10Mo samples*

Figure 11.27 illustrates hardness test marks realised on each sample type, with U-10Mo ingot encapsulated into nickel alloy and stainless steel canister, and both cross and flat sections from a successful bare foil extracted. U-10Mo ingot mark shows a darker area with visible scratches provided by mechanical polishing. The same aspects are visible for the other samples. Uranium carbides are visible in the nickel alloy picture. However, these artefacts will not influence the results because the carbides are not big enough compared to the hardness mark performed. U-10Mo alloy with a higher quantity of impurities and more prominent inclusions would provide different results in hardness measurement. Hardness marks are square enough with similar diagonal lengths, which is essential to validate the hardness values obtained.

Sample (Marks)	**Thickness ratio**	**Section measured**	**Load** (kgf)	**HV**
DU-MO (20)	1	Cross	30	272 ± 4
DU-SS-1 (10)	0.421	Cross	30	286 ± 5
DU-NI-1 (6)	0.329	Cross	30	308 ± 3
DU-SS-2 (15)	0.147	Flat	30	277 ± 4
DU-SS-3 (9)	0.141	Cross	30	272 ± 14
DU-SS-4 (8)	0.070	Cross	3	261 ± 14
DU-SS-4 (18)	0.070	Flat	30	240 ± 4

Table 11.2: *Hardness measurements of U-10Mo samples with different characteristics*

Hardness reference of the casted U-10Mo ingot is provided by the first line of Table 11.2 with the labelled sample DU-MO. This reference value is set to 272 HV, which is lower than reports about U-10Mo hardness performed on as-cast samples, in a range of 282 to 331 HV [52, 132]. About U-10Mo bare foil encapsulated into stainless steel canister DU-SS-1, measurements highlight a hardness increase of 5 % compared to the as-cast reference. For U-10Mo bare foils DU-SS-2, 3 and 4, the thickness ratio decrease until 0.07 seems to slowly decrease the hardness value compared to the reference in the cross-section, to reach 261 HV, i.e., a decrease of 9.58 % from the as-cast reference. Consequently, from 0.421 to 0.070, the hardness of U-10Mo decreases when the thickness ratio of the assembly is reduced. The work hardening seems to have a lower influence on the required stress to roll U-10Mo. This is probably due to the high working temperature T_1 and time spent in the oven. They contribute to refining the microstructure by annealing.

Interestingly, a hardness measurement difference between flat and cross-section is depicted for sample DU-SS-4. The first surface section exhibits a lower hardness result than the second, with a drop of 8.75 % to reach 240 HV. This difference in hardness from flat and cross sections could highlight an anisotropy tendency for bare foil deformation in the thickness direction compared to the longitudinal one. This tendency seems exacerbated by the low thickness ratio, as DU-SS-2 and 3 samples share the same thickness ratio with similar hardness measured for both sections. Finally, the hardness measured for the nickel alloy canister exhibits a higher value than the reference as-cast and the conventional stainless steel canister, with respective increases of 13.2 % and 7.7 %. The material used for U-10Mo bare foil rolling could influence the final properties of the bare foil by mechanical stress imposed by the protective canister.

Diffusion and uranium-molybdenum homogeneity

The composition of the U-10Mo bare foil is crucial for the success of fuel manufacturing. As the ingot is permanently in contact with the canister, diffusion and chemical interactions could contaminate the produced bare foils, exacerbated by high temperature and high process pressure. EDX measurements were conducted on samples with different manufacturing schemes to depict homogeneity and potential foil contamination during the process. First, the U-10Mo casted sample is investigated for a reference baseline for Mo and U homogeneity. The U-10Mo was melted by induction furnace and cast in a cleaned mould with applying external lubricant for ingot removal. It was then cut with a sawing machine to remove the casted head. As shown in Figure 11.28, ten parts were analysed in a cross-section direction along the ingot. Table 11.3 shows the qualitative composition of U and Mo in the ingot.

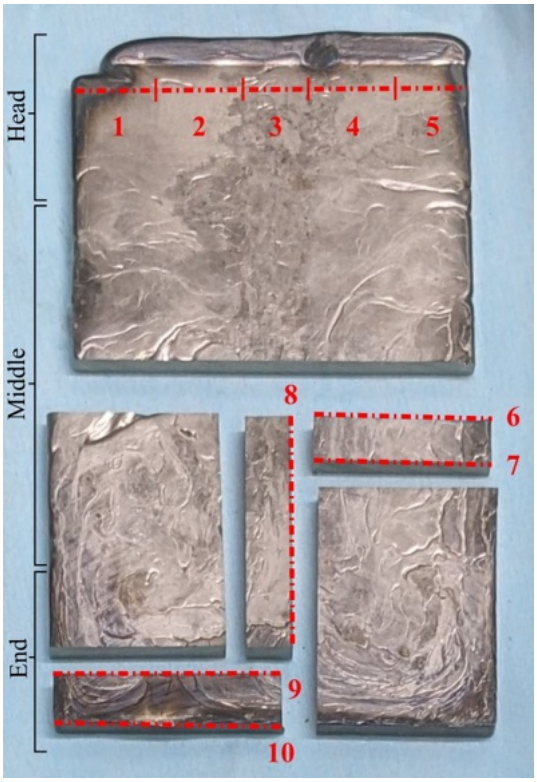

Figure 11.28: *U-10Mo ingot cutting*

	Elements	
Area (Points)	U (wt.-%)	Mo (wt.-%)
1 (Line)	91.21 ± n.a.	8.79 ± n.a.
2 (Line)	92.7 ± n.a.	7.30 ± n.a.
3 (Line)	92.98 ± n.a.	7.01 ± n.a.
4 (Line)	92.57 ± n.a.	7.44 ± n.a.
5 (Line)	92.67 ± n.a.	7.34 ± n.a.
Average	92.43 ± n.a.	7.58 ± n.a.
6 (12)	89.00 ± 2.51	11.00 ± 1.14
7 (12)	88.60 ± 2.49	11.40 ± 1.14
8 (11)	88.60 ± 2.65	11.40 ± 1.13
Average	88.80 ± 2.55	11.20 ± 1.14
9 (12)	89.20 ± n.a.	10.80 ± n.a.
10 (8)	89.50 ± 2.50	10.50 ± 1.13
Average	89.30 ± n.a.	10.70 ± n.a.

Table 11.3: *Qualitative ingot analysis*

The average concentration of U and Mo differs from the ingot head and the rest. While initial alloying is set to achieve 10 wt.-% in Mo and 90 wt.-% in U for casted ingot, a lack of up to 3 wt.-% in Mo concentration at the head section is observed. The highest concentration in Mo is detected from areas 6 to 8, in the middle of the ingot. The closest value from the initial target is localised in the ingot tail for areas 9 and 10. These differences in concentration could originate from the induction casting with heterogeneous Mo melting, which has a higher melting temperature than U, in addition to the placement of raw materials in the mould.

Diffusion between the stainless steel canister and the U-10Mo casted ingot

Investigation and analysis were performed on the stainless steel sample in contact with the U-10Mo ingot after the hot rolling process. Figure 11.29 shows sample preparation for EDX and SEM analysis, with a focus on three different surface aspects from, labelled **matt grey**, **shiny** and **dark**. Each is investigated with 5 EDX analysis points to depict concentration in uranium, molybdenum and stainless steel alloying elements, i.e., Fe, Cr, Ni, Mn and Si. The EDX machine provides uncertainty concerning the element content.

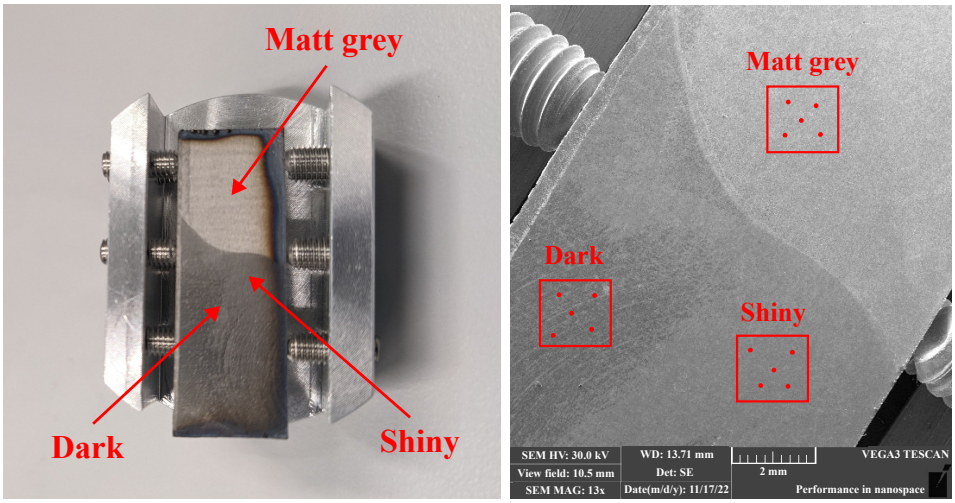

Figure 11.29: *Stainless steel canister sample preparation after the rolling process*

	Investigated area on the canister sample (Points)		
Element	Matt grey (5)	Shiny (5)	Dark (5)
U (wt.-%)	55.11 ± 1.40	63.32 ± 1.36	20.16 ± 0.97
Mo (wt.-%)	0.80 ± 0.26	0.64 ± 0.26	-
Fe (wt.-%)	31.20 ± 1.25	24.39 ± 1.05	52.51 ± 1.28
Cr/Ni (wt.-%)	11.10 ± 0.49	9.34 ± 0.49	24.83 ± 0.61
Mn/Si (wt.-%)	1.80 ± 0.31	1.10 ± 0.25	2.50 ± 0.21
Al/S (wt.-%)	-	1.21 ± 0.45	-

Table 11.4: *EDX measurement points with average results from the canister sample*

According to Table 11.4, the dark area has a composition closest to stainless steel. U represents a quarter in weight composition in this part, with no Mo diffusion. The most striking result is that matt grey and shiny areas comprise more than half of U, completed by Fe, further alloying elements and a small Mo concentration. Finally, the presence of Al and Si in the shiny areas is probably due to external contamination during sample preparation.

Diffusion in extracted U-10Mo bare foils

By involving high stress at high temperatures, the hot rolling of composite material involves chemical interactions between rolled materials. Diffusion could noticeably affect foils with diffusion depth and modify the composition, thereby affecting the rolled foil properties. Consequently, process manufacturing should be modified to match the composition criteria. Both stainless steel and U-10Mo bare foil samples, polished and unpolished with low and high thickness ratios, are studied by SEM and EDX to review the chemical composition and potential contamination.

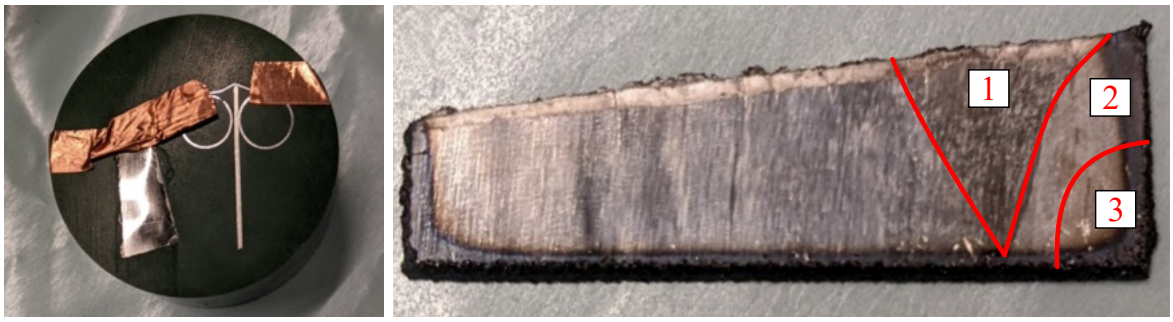

(a) Polished embedded foils (b) Unpolished foil sample with 3 different surface aspects

Figure 11.30: *U-10Mo bare foils samples preparation for EDX and SEM*

Mechanical polishing is performed on cross and flat sections for EDX investigation as shown in Figure 11.30 - (a). To depict chemical compositions, samples with dissimilar surfaces are also studied by EDX measurements, as shown in Figure 11.30 - (b). SEM and EDX results are summarised for the polished section in Figure 11.31 with surface concentrations noted in Table 11.5. Figure 11.32 - (a) with Table 11.6 does the same for a polished cross-cut section, Figure 11.32 - (b) with Table 11.7 give the result for an unpolished section.

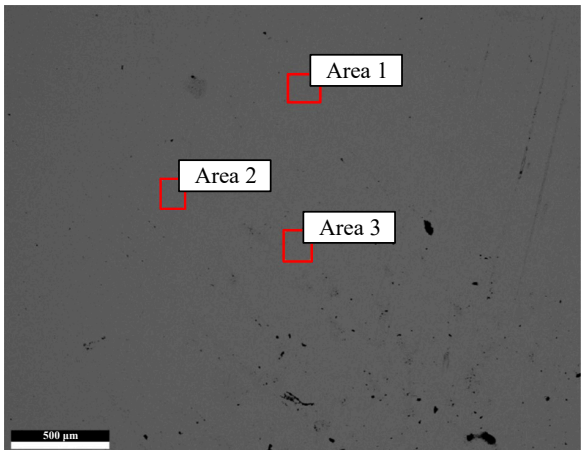

Figure 11.31: *U-10Mo flat section polished SEM picture with low* $t_{\%}$ *(0.065)*

	Elements	
Area	U (wt.-%)	Mo (wt.-%)
1	88.88 ± 1.89	11.12 ± 0.58
2	89.15 ± 1.88	10.85 ± 0.60
3	88.92 ± 1.90	11.08 ± 0.59
Average	88.92 ± 1.90	11.08 ± 0.59

Table 11.5: *U-10Mo flat section polished EDX area measurements*

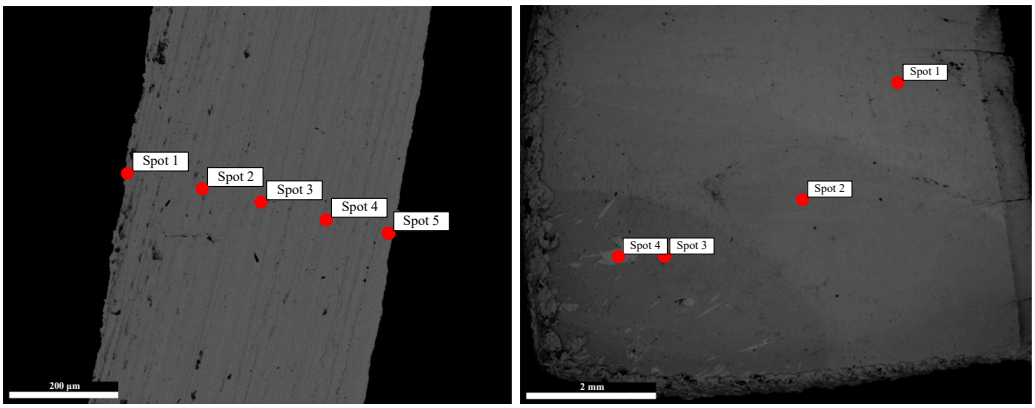

(a) SEM picture cross-section polished (b) SEM picture flat section unpolished

Figure 11.32: *EDX spots for U-10Mo polished and unpolished with low* $t_{\%}$ *(0.065)*

	Elements				
Spot	U (wt.-%)	Mo (wt.-%)	Fe (wt.-%)	Cr (wt.-%)	Ni (wt.-%)
1	84.26 ± 1.77	11.21 ± 0.60	3.54 ± 0.45	0.99 ± 0.24	-
2	72.91 ± 1.47	9.25 ± 0.49	13.48 ± 0.75	3.35 ± 0.34	1.02 ± 0.35
3	88.07 ± 1.88	11.11 ± 0.59	0.82 ± 0.32	-	-
4	88.66 ± 1.88	11.14 ± 0.58	0.2 ± 0.14	-	-
5	89.03 ± 1.90	10.97 ± 0.60	-	-	-

Table 11.6: *U-10Mo cross-section polished EDX results with low* $t_{\%}$ *(0.065)*

	Elements				
Spot	U (wt.-%)	Mo (wt.-%)	Fe (wt.-%)	Cr (wt.-%)	Ni (wt.-%)
1	68.41 ± 2.48	14.07 ± 0.72	0.76 ± 0.14	3.51 ± 0.39	13.25 ± 0.65
2	60.06 ± 2.08	21.27 ± 0.87	0.82 ± 0.32	3.31 ± 0.37	14.51 ± 0.87
3	60.97 ± 2.16	17.81 ± 0.82	2.51 ± 0.28	5.71 ± 0.57	12.99 ± 0.74
4	75.28 ± 2.60	9.17 ± 0.55	0.19 ± 0.08	3.65 ± 0.40	11.72 ± 0.47

Table 11.7: *U-10Mo flat section unpolished EDX results with low* $t_{\%}$ *(0.065)*

Table 11.5 depicts a good balance for U and Mo in the polished sample with low content in stainless steel elements. A few dark spots are visible in Figure 11.31, which are uranium carbides from the DU used and not investigated among the three areas analysed. The qualitative composition brings interesting results from the polished cross-section sample in Figure 11.32 - (a) with increased Fe and alloying elements detected with EDX.

The highest peak detected is in spot 2, followed by spot 1 in the left extremity. This contamination could be the first indication of diffusion between the canister and the uranium foil. Surprisingly, the other side of the foil is composed only of uranium and molybdenum. Finally, more dark spots are visible in the cross-section SEM picture on the side of spot 1 compared to the other spot 5.

Regarding the unpolished sample from Figure 11.32 - (b), EDX analysis shown in Table 11.7 exhibits different chemical compositions for each of the three surfaces of the U-10Mo bare foil. Each contains uranium and molybdenum in different proportions, affected by Fe, Cr and Ni pollution from stainless steel canisters. High Ni concentration appears for each area of the unpolished section with an average value of 13 wt.-%. The highest quantity of Fe with almost double Cr is detected in the shiny area in spot 2. The other spots seem less affected by Fe contamination, with a low quantity detected and still a high quantity of Ni. For Mo concentration, the result is somewhat counterintuitive. Spots 2 and 3 contain the highest Mo concentration, almost double the nominal target, while only spot 4 is located around the nominal value.

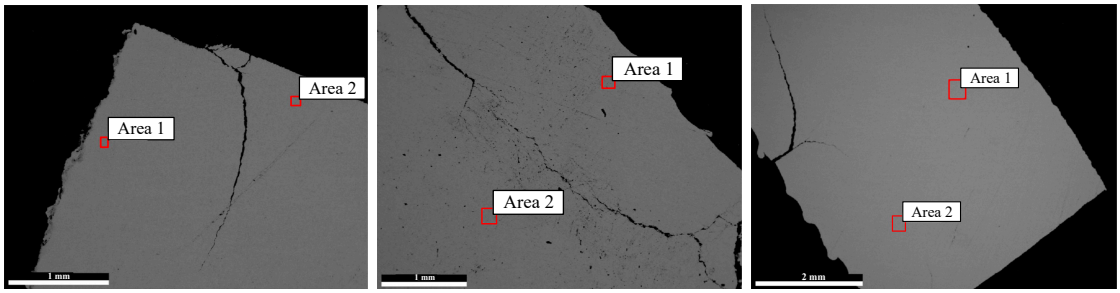

(a) (b) (c)

Figure 11.33: *U-10Mo foil samples EDX analysis with high* $t_{\%}$ *(0.147)*

	Elements				
Area	U (wt.-%)	Mo (wt.-%)	Fe (wt.-%)	O (wt.-%)	C (wt.-%)
1 - (a)	83.58 ± 1.54	8.27 ± 0.46	0.19 ± 0.14	8.038 ± 1.16	-
2 - (a)	73.14 ± 1.64	7.05 ± 0.37	0.20 ± 0.14	6.69 ± 0.69	12.92 ± 0.39
1 - (b)	73.21 ± 1.65	6.82 ± 0.37	0.08 ± 0.06	6.49 ± 0.67	13.4 ± 0.39
2 - (b)	73.15 ± 1.65	6.93 ± 0.34	0.06 ± 0.04	6.80 ± 0.69	13.07 ± 0.39
1 - (c)	72.02 ± 1.62	7.04 ± 0.35	0.19 ± 0.12	6.70 ± 0.68	13.05 ± 0.39
2 - (c)	72.37 ± 1.61	6.97 ± 0.34	0.07 ± 0.05	7.17 ± 0.73	13.41 ± 0.40

Table 11.8: *U-10Mo flat section polished EDX area measurements with high* $t_{\%}$ *(0.147)*

Further analysis of polished flat section from Figure 11.33, rolled at T_1, with the maximum rolling speed, shows the same tendency as U-10Mo polished cross-section samples with low thickness reduction from Figure 11.31, with a relatively good Mo homogeneity around 7 wt.-%, 3 wt.-% less than nominal target. U content is also lower than the composition target, with an average of 73 wt.-%. The high quantity of carbon could explain this lack in the used depleted uranium. It seems to have O content with an average of 8.23 wt.-%. These impurities are part of the raw U, and Mo used, which affect the final chemical composition.

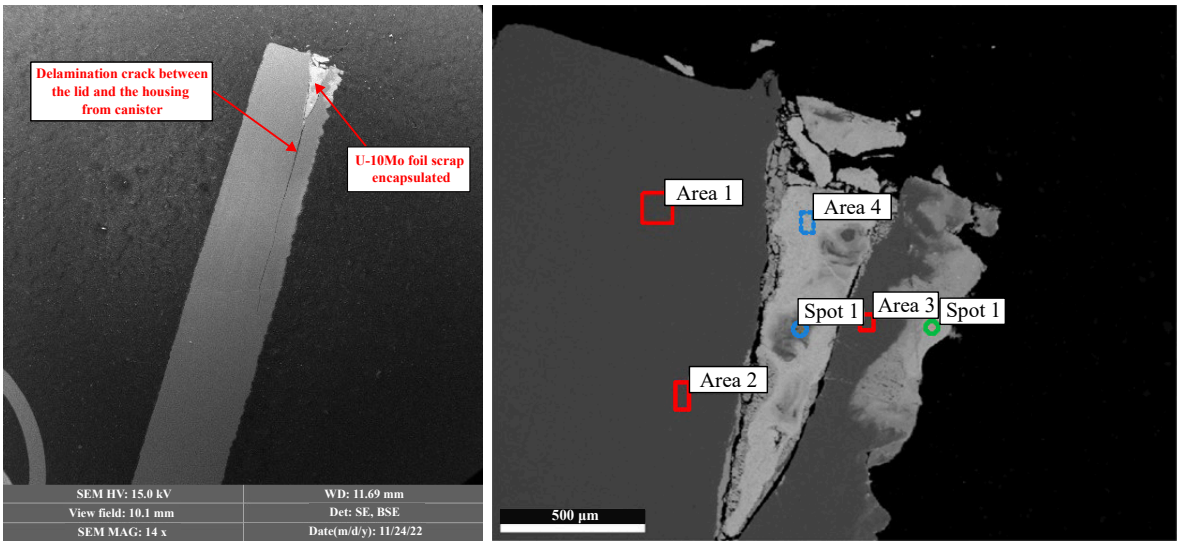

(a) U-10Mo bare foil scrap into canister (b) EDX measurements from U-10Mo bare foil in canister

Figure 11.34: *SEM and EDX measurements of U-10Mo foil from canister scrap after LBC*

	Elements				
Location	U (wt.-%)	Mo (wt.-%)	Fe/Cr/Ni/Si (wt.-%)	O (wt.-%)	C (wt.-%)
Area 1	-	0.80 ± 0.08	93.96 ± 1.99	1.87 ± 0.15	-
Area 2	-	0.77 ± 0.09	93.58 ± 1.96	0.85 ± 0.07	3.69 ± 0.40
Area 3	0.42 ± 0.13	0.77 ± 0.10	93.05 ± 1.95	1.86 ± 0.16	3.91 ± 0.42
Spot 1	62.28 ± 1.58	6.97 ± 0.36	13.34 ± 0.68	4.55 ± 0.51	12.84 ± 0.66
Spot 2	26.55 ± 0.97	2.70 ± 0.23	61.75 ± 1.52	-	8.99 ± 0.79
Area 4	71.65 ± 1.69	7.08 ± 0.37	0.98 ± 0.13	7.01 ± 0.73	13.28 ± 0.44

Table 11.9: *U-10Mo cross-section encapsulated into canister EDX measurements*

In the final section of the diffusion analysis, the U-10Mo bare foil part still encapsulated into the canister is studied and illustrated in Figure 11.34 with the chemical composition listed in Table 11.9. Areas 1 and 2 are investigated as the reference for the stainless steel canister.

The chemical composition reveals no diffusion of U or Mo to the stainless canister at a distance of 400 µm for area 1, 206 µm for area 2 and 92 µm for area 3. Two surface aspects are distinguishable in the ingot, with a dark and light area as shown in Figure 11.34 - (b). The light area depicts the initial ingot composition, with carbides and oxides but without alloying elements. On the black area characterised by spot 2, uranium concentration decreases by a factor of 3 compared to the light area. What stands out in this table is the high amount of stainless steel alloying elements in spot 2. Mo ratio also decreases in this spot. The most surprising aspect of this analysis is the presence of U and Mo on the spot 1, i.e., on the right of Figure 11.34 - (b), below the assembly. The proportion of both U and Mo is similar to the proportion depicted in area 4. This artefact seems to be uranium-molybdenum alloy from the ingot mixed with the stainless steel area cut to remove the foil.

11.3.5 Discussion & summary

Assembly & bare foil inspection with experimental measurements

U-10Mo assemblies and bare foils were visually inspected for different thickness ratios. About rolled assemblies, similarities with monolithic sample experiments are highlighted with oxidised surfaces and few edge cracks according to the rolling scheme performed. The measured load ratio highlights a low work hardening of the assembly from 0.6 thickness ratio until lower values, thanks to the high temperature used for the rolling process, with a short annealing time performed between each pass to heat the sample. In addition, individual loads in the width direction of assemblies stay homogeneous, as shown in Figure 11.22. These results encourage future industrialisation with no curvature shape and a potential range of load ratio to increase for future hot rolling optimisation.

Nevertheless, the main issue for U-10Mo assemblies is the cracks in width and length direction, which appear during the process. Mainly two reasons can explain these phenomena: a maladaptive manufacturing process with a high load applied by rolling on a weak laser-welded area and initial issues with the U-10Mo ingot before encapsulating. The first one was resolved by modifying the laser welding scheme with higher weld depth and width, in addition to an increase in the welded area. For the second, the ingot machining, as tight as possible to match with housing dimension, resolved the cracks issue investigated in Figure 11.15. Indeed, perfect machining of U-10Mo ingot avoids the formation of internal voids, which create parts with low tenacity against the load applied and lead to cracks and delamination of the canister top lid. U-10Mo bare foils with low and high thickness ratios share key features from visual inspections. Burns, cracks and scratches are observed, with higher burn areas for a high thickness ratio.

These gradient aspects of burns might be explained by dissimilar contact with the canister, which involves different surface conditions and modifications in heat exchanges, the load applied and local chemical composition. A solution would be to have an initial ingot thickness as tight as possible before encapsulating to ensure perfect contact with the canister. An adapted canister is needed to weld the lid perfectly to the housing. A better initial surface condition might also increase global bare foil quality by polishing the top and bottom surfaces. It will allow them a better flatness and contact surface with the canister.

Finally, bare foil waviness and thickness highlight interesting results. For a high thickness ratio, the waviness exhibits high values on both right and left edges, in a rolling direction, with a reduced waviness profile for a low thickness ratio. The same tendency appears in thickness measurements, where dog-boning is highlighted for a low thickness ratio compared to the foil centre. This defect is typical of the rolling process and reported in other manufacturing reports. This issue could be resolved by laser cutting these undesired edges, both local over thickness and high waviness parts. Heat treatments under loads, annealing, and stress relief would be a solution to reduce waviness issues. Indeed, fuel meat with too high variability in thickness and with a high waviness profile could influence the future manufacturing processes, especially for the aluminium cladding, but also for irradiation where waviness and variation in thickness have impacts on irradiation results [133, 134] within same time dissimilar volume in fissile uranium.

Microstructure and hardness measurements

Microstructure exhibited by both U-10Mo ingot and bare foil highlights interesting observations in terms of manufacturing. For the casted ingot, border grains were fully formed, in opposition to the central microstructure with a dendritic shape structure, with variable transition length measures as shown in Figure 11.1, mainly around 200 to 300 µm. The main hypothesis of dissimilar microstructure border might be a phenomenon close to quenching at the border of the copper mould. The interior and border of the ingot cool down in different ways, leading to these microstructure differences. In addition, dendrites exacerbate the necessity of additional heat treatments for the casted ingot before hot rolling. It will benefit for mechanical properties by homogenisation of grains and, consequently, better isotropy for the rolling process, in addition to improving global foil quality in terms of mechanical properties and irradiation performance. For the microstructure observed for bare foils, the morphology is similar to other uranium foils obtained by the hot rolling process, as shown by Joshi et al., with different characteristics of U-Mo bare foils after rolling [55]. Grain length increased on the foil compared to the ingot. Uranium carbides located initially at grain boundaries still follow this trend for rolled uranium foils.

Therefore, dynamic recrystallisation during the process can occur and transforms the dendritic structure to fully developed grains, especially for low thicknesses of the bare foil and high annealing times in the oven. Another solution to resolve different microstructures prior to hot rolling and reduce the heat treatment time would be designing a new mould for induction casting with optimised and reduced ingot dimensions for microstructure homogenisation.

The hardness measurement of rolled foils brings interesting data about mechanical behaviour and changes between U-10Mo casted ingots and rolled foils. Results from Table 11.2 suggest that U-10Mo bare foil has not a high work hardening during the process. The result is counterintuitive when work hardening would have to affect material properties by stress applied with hot rolling. Consequently, this work hardening would increase the stress needed to achieve plastic deformation, which is not the case in this work. In the same way as the load measured for the assembly before, the choice of high temperature combined with longer annealing time in the oven avoids work hardening. Cross-section hardness highlights lower values for rolled foils than as-cast samples, which is an encouraging result to optimise the rolling process and increase the yield and rolling parameters values.

Nevertheless, the U-10Mo hardness value from the nickel alloy canister suggests a link between the canister material and the final U-10Mo bare foil properties, with a higher hardness value for this material than stainless steel. In the same way, the working temperature would help to avoid work hardening. Removing uranium carbides before casting would help to increase global ductility and decrease hardness, which helps during foil manufacturing.

Diffusion

Results reported in section 11.3.4 suggest that diffusion occurs between the U-10Mo ingot and the stainless steel canister during the hot rolling process. With the high working temperature used, an unneglectable quantity of canister alloying elements was detected with EDX analysis on U-10Mo bare foil samples, as shown in Figure 11.31, 11.32 and 11.33 for different thickness ratios. This interdiffusion layer is probably U_6Fe or UFe_2 according to different reports about diffusion experiments conducted with U, Fe, Ni and Cr alloying elements [135, 136]. The highest content of these elements was detected for unpolished U-10Mo flat sections with a high quantity of Cr and Ni, with additional Fe, respectively, in an average of 13 wt.-%, 4 wt.-% and 1 wt.-%. When the samples are polished, the content of alloying elements from stainless steel decreases to have a total absence of Cr, Ni & Fe for the flat surface of U-10Mo bare foils and content in Fe of 0.13 wt.-% on average. For the polished cross-section, a similar quantity of alloying elements was detected. One exception with unexpected diffusion content was highlighted in Figure 11.32, where a peak of 13 wt.-% in Fe is detected on the left side of the cross-section. This spot corresponds to the exit laser kerf, which explains this anomalous amount of Fe.

The laser cutting melts both U-10Mo and the metallic canister locally during the process for bare foil removal. This melting pool is then ejected by the gas flow jet, but if the volume of liquid is too high, it solidifies and stays on the cut foil.

This artefact is then found by EDX with the mix of U-10Mo and alloying elements but not provided by chemical diffusion. Regarding the thickness ratio of the U-10Mo sample, this parameter might also lead to different diffusion behaviour. Low thickness ratio values might lead to a higher diffusion rate by increasing the stress levels involved in the rolling process and the contact surface between the U-10Mo bare foil and the canister. The different surface conditions of the rolled foil investigated illustrate this. The diffusion occurs at a few micrometres depth according to these differences between polished and unpolished and different thickness ratios. This potential surface contamination might be eliminated with electrochemical polishing, which brings the same shiny surface for all the foil, as shown in Figure 11.35. Future investigations should be performed to understand how diffusion occurs and how to change the manufacturing process to reduce its impact on bare foils.

(a) Before cleaning

(b) After cleaning

Figure 11.35: *U-10Mo bare foils before and after electrochemical cleaning for PVD coating*

Edges and borders would also be subject to increased diffusion due to the highest presence of stainless steel around the bare foil, i.e. on the top, bottom and edge, as shown in Figure 11.34. These areas have an increased contact surface between the canister and the foil, which enhances the diffusion of elements between the stainless steel and the U-10Mo bare foil. LBC should be used to cut borders around the U-10Mo bare foil to remove this contaminated part. Further work would be needed to develop a reliable diffusion area to know the diffusion length in U-10Mo bare foil. Regarding irradiation, even with a small amount of iron in the fuel meat, it leads to issues for radioactive products and potential nuclear waste [5]. Regarding plate manufacturing, the diffusion of alloying elements into the fuel meat will modify and affect thermomechanical properties for the following manufacturing processes. Different surface compositions on the foil lead to issues for PVD coating, as zirconium particles can not be deposited on the foil, as shown in Figure 11.36.

Figure 11.36: *Non-sticking of zirconium on the U-10Mo bare foil with surface contamination*

Finally, the overall diffusion investigated tends to be a surface diffusion which occurs from the U-10Mo foil to the metallic canister, as reported in Figure 11.29 and in Table 11.4 with the canister sample in contact with the uranium ingot during the hot rolling process. This preferential diffusion could explain the difference in uranium homogeneity from Table 11.7 where the Mo content reaches 20 wt.-%. Visual inspections of foils with shiny, dark and grey appearance might suggest differences in both chemical composition and surface roughness. Further analysis to study the difference in roughness between these areas should be performed to characterise these different surfaces.

Chapter 12

Conclusion and perspectives

The first European manufacturing pilot line implemented at Framatome-CERCA for the DU-10Mo monolithic fuel for the FRM II neutron source was described in this work with the success of the different manufacturing processes:

- **Laser beam welding** was successfully conducted for DU-10Mo ingot encapsulating into a metallic canister. Different material sets were tested with different parameter combinations to optimise welding and to ensure mechanical links. The feasibility of laser technology for foil manufacturing was demonstrated, an unconventional and innovative process for the nuclear sector. Canisters were also designed in different versions to match the ingot geometry and adapted for foil manufacturing and future industrialisation.

  Welding speed and laser power should be optimised according to industrial criteria to match the specific geometry of the manufactured canister. Other parameters should also be considered, such as gas type and wavelength. They can be studied to extract the best potential from this technology. Then, topological optimisation with numerical simulations would be necessary to remove unused canister parts and improve the weak areas for the hot rolling process. Finally, different adaptations have to be done for future industrialisation, such as an improved vision system for the welding automatisation or better manufacturing quality requirement for canisters, such as backlashes;

- **Hot rolling** as the primary manufacturing process was successfully performed to produce the first monolithic DU-10Mo bare foils from initial casted ingots in the Framatome research facility. Before uranium works, different experiments with inert materials allowed us to study the mechanical behaviour of composite assemblies under high pressure and working temperature. It involves complex changes in material properties and interaction between samples and the rolling machine. Adapting the rolling scheme with prior manufacturing substeps was essential for global foil quality.

Numerical simulations involving **F**inite **E**lement **M**ethod (FEM) should be performed to improve rolling passes and find weak areas or overexposed parts for a potential canister or ingot redesign to improve this critical manufacturing step. Adapting heating time also by numerical simulation will be essential to improve the process and industrialisation. Performing the same rolling process with heat-treated ingots, i.e. with a refined microstructure and then different mechanical properties, should also be interesting to highlight the influence and necessity of ingot homogenisation for manufacturing and then irradiation. Finally, additional tensile tests at room and high temperatures are essential to characterise the mechanical properties of bare foils produced in this manufacturing line;

- **Laser beam cutting** was realised for the first time on U-10Mo bare foils as a new technology to improve the accuracy and safety of this manufacturing line. As was the case for the hot rolling process, laser cutting was studied on inert material to reveal the impact of the parameters on it and then on the uranium foil produced.

  The improvement of global yield should be studied by reusing laser-cutting waste of uranium part encapsulated in the canister border or uranium powder provided by the process, similar to powder atomisation. This powder can be used for further fuel manufacturing processes, such as additive manufacturing or cold spray.

This new monolithic U-10Mo bare foil will be coated with zirconium coating by PVD and then aluminium-cladded with C2TWP by Framatome. It represents the best alternative to the FRM II to convert its fuel and continue to deliver neutrons for research in Germany and Europe. LEU foils will be produced by following the manufacturing process performed in this work for the first irradiation test in the first half of 2024 and to be fully used in the FRM II core in the following years after irradiation analysis and overall improvement in the manufacturing process. This fuel represents a new opportunity for other research reactors to readapt their fuel, but also for new types of fuel for nuclear power plants, such as **S**mall **M**odular **R**eactor (SMR) where it could be used as fuel. Some of those may need metallic fuel, in compact cores, with enrichment as high as 19.75 %.

List of Figures

List of Tables

Acronyms and Abbreviations

ANL Argonne National Laboratory

BMBF Bundes Ministerium für Bildung und Forschung

CEA Commissariat à l'Énergie Atomique et aux Énergies Alternatives

CERCA™ Compagnie pour l'Etude et la Realisation de Combustibles Atomiques

CRIL CERCA™ Research Innovation Laboratory

C2TWP CERCA™ CEA TUM welding process

D_2O Deuterium oxide

DU Depleted uranium

EDX Energy-dispersive X-ray spectroscopy

EMPIrE European Mini-Plate Irradiation Experiment

FEM Finite Element Model

FRM II Forschungs-Neutronenquelle Heinz Maier-Leibnitz

HAZ Heat Affected Zone

HCl Hydrogen chloride

HEU Highly enriched uranium

HF Hydrofluoric acid

HFIR High Flux Isotope Reactor

HV Vickers hardness

ILL Institut Laue-Langevin

INL Idaho National Laboratory

LASER Light Amplification by Stimulated Emission of Radiation

LBC Laser beam cutting

LBW Laser beam welding

LEU Low enriched uranium

NNSA National Nuclear Security Administration

ppm Parts per million

PVD Physical Vapor Deposition

R&D Research & Development

RD Rolling direction

RERTR Reduced Enrichment for Research and Test Reactors

SEM Scanning electron microscope

SCC Stress Crack Corrosion

SS Stainless steel

StMWK Bayerisches Staats Ministerium für Wissenschaft und Kunst

Ta6V4 Titanium Grade 5

TD Transverse direction

TIG Tungsten Inert Gas

TUM Technical University of Munich

^{235}U Uranium 235

UO_2 Uranium dioxide

wt.-% Weight percentage

U-Mo Uranium-molybdenum

U-10Mo Uranium alloyed with 10 wt.-% in molybdenum

USDOE US Department Of Energy

Symbols

E Young's modulus (GPa)

σ Stress (MPa)

$\sigma_{0.2}$ / σ_{YS} Yield stress (MPa)

σ_{TS} Tensile stress (MPa)

ϵ Strain (%)

ϵ_{e} Elastic strain (%)

ϵ_{p} Plastic strain (%)

$\dot{\epsilon}$ Strain rate (s^{-1})

h_0 Initial sample thickness (mm)

h_{e} Entry thickness (mm)

h_{f} Final thickness (mm)

h_{i} Measured thickness at the end of the current rolling pass (mm)

h_{s} Target thickness (mm)

$\mathrm{r}_{\%}$ Reduction ratio

R Radius (mm)

LD Load-deflection (mm)

$\mathrm{l}_{\%}$ Load ratio

l_{i} Applied load during the current rolling pass (t)

$\mathrm{l}_{\mathrm{max}}$ Maximal load admissible for the rolling machine (t)

P_{i} Laser power (W)

V_{i} Welding / cutting speed ($\mathrm{mm} \cdot \mathrm{min}^{-1}$)

H_{i} Heat input ($\mathrm{J} \cdot \mathrm{mm}^{-1}$)

PR_{i} Gas pressure (bar)

F_{i} Working distance (mm)

T_i Temperature (℃)

$t_{\%}$ Thickness ratio

T_M Melting temperature (℃)

λ Thermal conductivity ($J \cdot m^{-1} \cdot K^{-1}$)

c_p Specific heat ($J \cdot kg^{-1} \cdot K^{-1}$)

ε Emissivity

ρ Density ($g \cdot cm^{-3}$)

α**-U** Alpha-uranium phase

β**-U** Beta-uranium phase

γ**-U** Gamma-uranium phase

γ'**-**U_2Mo Gamma-prime uranium from gamma decomposition in UMo

Glossary

Rolling stand For the rolling process, the location where rolls are set to perform the process. The rolling stand entry corresponds to the area where the sample is entered, and the rolling stand exit is where the sample gets back to continue the rolling.

Load-deflection For the rolling process, the load parameter needed to compensate for the material springback of the rolled sample.

Thickness ratio For the rolling process, the ratio between the measured thickness at the end of a rolling pass and the initial sample thickness before the rolling process.

Load ratio For the rolling process, the ratio between the maximum measured load of the current rolling pass and the maximum load mechanically allowed by the rolling machine.

Heat input For the laser processes, the ratio between the laser power and the manufacturing process speed.

Delta thickness For the rolling process, the difference between the target thickness and the measured thickness at the end of a rolling pass.

Kerf For the laser cutting process, the cut produced by the laser through the cut sample.

Dross For the laser cutting process, the particles which are ejected from the kerf by the assisting gas pressure.

Overlapping For laser cutting process, a shared affected area by a laser pulse with the previous pulse.

Ingot Induction casted material used for hot rolling.

Bare foil Foil produced without a zirconium layer.

Fuel plate The final product that contains coated foil encapsulated into a cladding material.

Monolithic Term for the sample used for rolling process and which is formed by one alloy (ex: monolithic U-10Mo or monolithic stainless steel samples)

Assembly Element ready to be rolled and composed with the canister and the encapsulated ingot.

Canister Assembly of the housing and the lid without ingot.

Lid Top part of the canister to enclose the assembly.

Housing Bottom part of the canister where the ingot is set for the rolling process.

List of publications

K. Buducan, S. Lorand, B. Baumeister, T. Chemnitz, W. Petry B. Stepnik, C. Rontard, F. Gauche. DEVELOPMENT OF LASER PROCESSES ON U-10Mo MONOLITHIC FUEL FABRICATION PROCESS AT FRAMATOME (CERCA BUSINESS LINE), Proceeding for RRFM, Budapest, 2022.

K. Buducan, S. Lorand, B. Stepnik, C. Rontard, F. Gauche, B. Baumeister, C. Schwarz, T. Chemnitz, W. Petry. U-MO BARE FOIL ROLLING PROGRESS FOR FRM II CONVERSION, presented for RERTR, Vienna, 2022.

K. Buducan, B. Baumeister, S. Lorand, B. Stepnik, W. Petry. MANUFACTURING OF NEW URANUM FUEL FOR FRM II CONVERSION, presented for MEP Colloquium, Garching, 2022.

K. Buducan, B. Baumeister, W. Petry, S. Lorand, B. Stepnik, C. Rontard, F. Gauche. FIRST RESULTS OF THE EUROPEAN MANUFACTURING PROCESS FOR BARE U-MO FOILS, Poster for RRFM, Helsinki, 2021.

Bibliography

[1] History - TUM FRMII. https://www.frm2.tum.de/en/frm2/about-us/history/, 2023.

[2] Facts & Figures - TUM FRMII. https://www.frm2.tum.de/en/frm2/about-us/facts-figures/, 2023.

[3] Gérard Pépy. Les faisceaux de neutrons - Comprendre et caractériser la matière. *Technique de l'ingénieur*, January 2007.

[4] Alain Ballagny and Bruno Guigon. Réacteurs de recherche et d'irradiation de matériaux. *Technique de l'ingénieur*, January 2004.

[5] Weston M. Stacey. *Nuclear Reactor Physics*. Wiley-VCH, Weinheim, 2nd ed., completely rev. and enlarged edition, 2007.

[6] Yeon Soo Kim. Uranium Intermetallic Fuels (U–Al, U–Si, U–Mo). In *Comprehensive Nuclear Materials*, pages 391–422. Elsevier, 2012.

[7] Cheikh M'Backé Diop. Physique des réacteurs – Les réactions nucléaires. *Technique de l'ingénieur*, 2016.

[8] M R Finlay and M I Ripley. Research Reactor Fuel - an Update. *Materials and Engineering Science Australian Nuclear Science and Technology Organisation (ANSTO)*, 2003.

[9] The HERACLES Consortium: HORIZON 2020 projects. https://heracles-consortium.eu/horizon2020.php, 2023.

[10] NNSA USDOE. History of LEU fuel development and selection of USHPRR fuel system, 2015.

[11] B Rabin, M Meyer, J Cole, G Hofman, W Jones, D Keiser, Y Kim, C Miller, H Ozaltun, F Rice, J Smith, D Wachs, and N Woolstenhulme. Preliminary Report on U-Mo Monolithic Fuel for Research Reactors. *Idaho National Laboratory*, 2017.

[12] V.S. Yemel'yanov, V.S. and A.I. Yevstyukhin. *The metallurgy of nuclear fuel: Properties and Principles of Ihe Technology of Uranium, Thorium and Plutonium*. Pergamon Press, 1969.

[13] Michael F. L'Annunziata. Radioactivity and Our Well-Being. In *Radioactivity*, pages 1–66. Elsevier, 2016.

[14] Donna Strahan. Uranium in glass, glazes and enamels: History, identification and handling. *Studies in Conservation*, 46(3):181–195, September 2001.

[15] Gerhardt H. Wolfe, editor. *Uranium: Compounds, Isotopes and Applications*. Nova Science Publishers, New York, 2009.

[16] Jonathan S. Morrell and Mark J. Jackson, editors. *Uranium Processing and Properties*. Springer New York, New York, NY, 2013.

[17] Michel Alexandre and Jean-Pierre Quaegebeur. Enrichissement de l'uranium - Principes. *Technique de l'ingénieur*, January 2009.

[18] Gilles Bordier and Michel Alexandre. Séparation de l'uranium par laser. *Technique de l'ingénieur*, July 2003.

[19] Cars W Tucker. The Crystal Structure of the β-Phase of Uranium, 1951. *Acta Crystallographica*, 1951.

[20] Anubhav Jain, Shyue Ping Ong, Geoffroy Hautier, Wei Chen, William Davidson Richards, Stephen Dacek, Shreyas Cholia, Dan Gunter, David Skinner, Gerbrand Ceder, and Kristin A. Persson. Commentary: The Materials Project: A materials genome approach to accelerating materials innovation. *APL Materials*, 1(1):011002, July 2013.

[21] C. W. Jacob and B. E. Warren. The Crystalline Structure of Uranium. *Journal of the American Chemical Society*, 59(12):2588–2591, December 1937.

[22] Enrique E. Pasqualini. Gamma Uranium Molybdenum Alloy: Its Hydride and Performance. In Rehab O. Abdel Rahman and Hosam El-Din Mostafa Saleh, editors, *Nuclear Material Performance*. InTech, June 2016.

[23] A. S. Wilson and R. E. Rundle. The structures of uranium metal. *Acta Crystallographica*, 2(2):126–127, April 1949.

[24] J. J. Park and D. P. Fickle. Uranium-platinum system. *Journal of Research of the National Bureau of Standards Section A: Physics and Chemistry*, 64A(1):107, January 1960.

[25] Alexander Landa, Per Söderlind, and Amanda Wu. Phase Stability in U-6Nb Alloy Doped with Ti from the First Principles Theory. *Applied Sciences*, 10(10):3417, May 2020.

[26] G L Hofman. Design of high density gamma-phase uranium alloys for LEU dispersion fuel applications. October 1998.

[27] Christian Steyer. Plasma- und festkörperphysikalische Optimierung eines Beschichtungsverfahrens für monolithische UMo-Kernbrennstoffe, PhD Thesis TUM. June 2019.

[28] Saumyadeep Jana, Alan L. Schemer-Kohrn, Nicole R. Overman, Lucas E. Sweet, Elizabeth J. Kautz, Curt A. Lavender, and Vineet V. Joshi. Eutectoid Transformation in U10Mo Alloy: Effect of Deformation History and Homogenization Heat Treatment. Technical Report PNNL–28519, 1503687, January 2019.

[29] A.J. Clarke, K.D. Clarke, R.J. McCabe, C.T. Necker, P.A. Papin, R.D. Field, A.M. Kelly, T.J. Tucker, R.T. Forsyth, P.O. Dickerson, J.C. Foley, H. Swenson, R.M. Aikin, and D.E. Dombrowski. Microstructural evolution of a uranium-10 wt.% molybdenum alloy for nuclear reactor fuels. *Journal of Nuclear Materials*, 465:784–792, October 2015.

[30] François Cardarelli. *Materials Handbook*. Springer London, London, 2008.

[31] ANL. Properties and Applications of Heat-Treated Uranium Alloys (Ref. 1). https://web.evs.anl.gov/uranium/guide/ucompound/propertiesu/table.cfm, 2023.

[32] V.P. Sinha, P.V. Hegde, G.J. Prasad, G.K. Dey, and H.S. Kamath. Phase transformation of metastable cubic γ-phase in U–Mo alloys. *Journal of Alloys and Compounds*, 506(1):253–262, September 2010.

[33] V.P. Sinha, P.V. Hegde, G.J. Prasad, G.K. Dey, and H.S. Kamath. Effect of molybdenum addition on metastability of cubic γ-uranium. *Journal of Alloys and Compounds*, 491(1-2):753–760, February 2010.

[34] Battelle Memorial Institute. Mechanical properties of gamma-phase uranium-molybdenum alloys. 1958.

[35] G Beghi. Gamma phase uranium-molybdenum fuel alloys. *European Atomic Energy Community - Euratom*, page 90, 1968.

[36] Christoph Leyens and Manfred Peters, editors. *Titanium and Titanium Alloys: Fundamentals and Applications*. Wiley, first edition, July 2003.

[37] Yannick Robert. Simulation numérique du soudage du TA6V par laser YAG impulsionnel: caractérisation expérimentale et modélisation des aspects thermomécaniques associés à ce procédé. page 256, September 2007.

[38] AISI. High-temperature characteristics of stainless steels. Technical Report 9004, Nickel Development Institute.

[39] Aerojet General Nucleonics. Final Report on Conceptual Design and Initial Radiological Safety Study for a Pulsed Nuclear Reactor (AN-176). Technical report, April 1960.

[40] D. Frazer, D. Jadernas, N. Bolender, J. Madden, J. Giglio, and P. Hosemann. Elevated temperature microcantilever testing of fresh U-10Mo fuel. *Journal of Nuclear Materials*, 526:151746, December 2019.

[41] John E. Gates, Edward G. Bodine, J. Clarence Bell, Arthur A. Bauer, and George D. Calkins. Stress-strain properties of irradiated uranium-10 w/o molybdenum. Technical Report BMI-APDA-638, January 1958.

[42] C.A.W. Peterson and R.R. Vandervoort. Mechanical properties of some uranium alloys. *University of California*, 1964.

[43] Jason Schulthess, Randy Lloyd, Barry Rabin, Michael Heighes, Tammy Trowbridge, and Emmanuel Perez. Elevated temperature tensile tests on DU–10Mo rolled foils. *Journal of Nuclear Materials*, 510:282–296, November 2018.

[44] Jason Schulthess, Michael Heighes, Connor Michelich, Cynthia Adkins, M. Craig Marshall, Mitchell Plummer, Fidelma Di Lemma, Tammy Trowbridge, and James I.

Cole. Mechanical and Thermophysical properties of low enriched uranium-10wt% molybdenum rolled foils. *Journal of Nuclear Materials*, 563:153628, May 2022.

[45] V. V. Kalashnikov, V. V. Titova, G. Ia. Sergeev, and A. G. Samoilov. Uranium-molybdenum alloys in reactor construction. Technical report, 1959.

[46] J.L. Klein. *Uranium and Its Alloys - Nuclear Reactor Fuel Elements*. A. R. Kaufmann, 1962.

[47] J T Mihalczo. Reactivity calibrations and fission-rate distributions in an unmoderated, unreflected uranium-molybdenum alloy research reactor. *Oak Ridge National Laboratory*, page 24, May 1962.

[48] Vineet V. Joshi, Eric A. Nyberg, Curt A. Lavender, Dean Paxton, and Douglas E. Burkes. Thermomechanical process optimization of U-10wt% Mo – Part 2: The effect of homogenization on the mechanical properties and microstructure. *Journal of Nuclear Materials*, 465:710–718, October 2015.

[49] K. G. Hoge. Some Mechanical Properties of Uranium-10 Weight Percent Molybdenum Alloy Under Dynamic Tension Loads. *Journal of Basic Engineering*, 88(2):509–517, June 1966.

[50] B Boudouresques and M Englander. Strength and creep of uranium alloys. *Progress in Nuclear Energy, Series V, Vol.2 - Metallurgy and Fuels*, 1959.

[51] J. H. Gittus. *Uranium*. Metallurgy of the Rarer Metals. London Butterworths, butterwoths edition, 1963.

[52] M.B. Waldron, R.C. Burnett, and S.F. Pugh. The mechanical properties of uranium-molybdenum alloys. July 1958.

[53] R.F. Hills, B.R. Butcher, and B.W. Howlett. The mechanical properties of quenched uranium-molybdenum alloys. *Journal of Nuclear Materials*, 11(2):149–162, February 1964.

[54] B. McPherson. The determination of true stress-true strain curves and modulus of elasticity of uranium-10 w/o molybdenum alloy at elevated temperatures. Final Report to Atomic Power Development Associates. Technical Report AECU-3801, 4310800, March 1958.

[55] Vineet V. Joshi, Dean M. Paxton, Curt A. Lavender, and Douglas Burkes. The Effect of Rolling As-Cast and Homogenized U-10Mo Samples on the Microstructure Development and Recovery Curves. Technical Report PNNL–25781, 1339909, July 2016.

[56] Arun Devaraj, Libor Kovarik, Elizabeth Kautz, Bruce Arey, Saumyadeep Jana, Curt Lavender, and Vineet Joshi. Grain boundary engineering to control the discontinuous precipitation in multicomponent U10Mo alloy. *Acta Materialia*, 151:181–190, June 2018.

[57] Xiaohua Hu, Xiaowo Wang, Vineet V. Joshi, and Curt A. Lavender. The effect of thermomechanical processing on second phase particle redistribution in U-10 wt%Mo. *Journal of Nuclear Materials*, 500:270–279, March 2018.

[58] ISO 6892-2:2018 - Matériaux métalliques - Essais de traction - Partie 2 : Méthode d'essai à température élevée, 2018.

[59] ASM International, editor. *ASM Handbook*. ASM International, Materials Park, Ohio, 10th editon edition, 1990.

[60] P. D. Desai. Thermodynamic Properties of Manganese and Molybdenum. *Journal of Physical and Chemical Reference Data*, 16(1):91–108, January 1987.

[61] Aubert&Duval. Titanium Alloy TA6V, 2023.

[62] Thyssenkrupp Materials (UK) Ltd. Stainless Steel 1.4404 - Material Data Sheet, November 2017.

[63] Peter Pichler, Brian J. Simonds, Jeffrey W. Sowards, and Gernot Pottlacher. Measurements of thermophysical properties of solid and liquid NIST SRM 316L stainless steel. *Journal of Materials Science*, 55(9):4081–4093, March 2020.

[64] HighTempMetals. Inconel 600 Tech Data, 2023.

[65] Special Metals. INCONEL Alloy 600 - Material Data Sheet, 2008.

[66] Mikaél' A. Bramson. *Emissivity of Various Materials*, pages 533–552. Springer US, Boston, MA, 1968.

[67] Kim Choong S. Thermophysical properties of stainless steels. *Argonne National Laboratory*, 1975.

[68] Randy Shurtz. Total Hemispherical Emissivity of Metals Applicable to Radiant Heat Testing. Technical Report SAND2018-13271, 1483461, November 2018.

[69] Peter Johannes Felbinger. Investigation of dry chemical etching of different (precious) metals under thermal activation by laser heating. *Master Thesis, Philipps-University Marburg*, 2021.

[70] Douglas E. Burkes, Cynthia A. Papesch, Andrew P. Maddison, Thomas Hartmann, and Francine J. Rice. Thermo-physical properties of DU–10wt.% Mo alloys. *Journal of Nuclear Materials*, 403(1-3):160–166, August 2010.

[71] Douglas E. Burkes Amanda J. Casella Andrew M. Casella Stefan Elgeti Christian Reiter Adam. B. Robinson Frances. N. Smith Daniel. M. Wachs Winfried Petry Tanja K. Huber, Harald Breitkreutz. Thermal conductivity of fresh and irradiated u-mo fuels. *Journal of Nuclear Materials*, 503:304–313, 2018.

[72] Gilles Brassart, Jean-Louis Meyzonnette, and Jean-Paul Pocholle. Sources laser. *Optique Photonique*, September 1996.

[73] Karl F. Renk. *Basics of Laser Physics: For Students of Science and Engineering*. Graduate Texts in Physics. Springer Berlin Heidelberg, Berlin, Heidelberg, 2012.

[74] Jean-Pierre Prenel. Physique du laser - Historique et principes de base. *Optique Photonique*, January 1999.

[75] W. W. Duley. *Laser Processing and Analysis of Materials*. Springer US, Boston, MA, 1983.

[76] Bahaa E. A. Saleh and Malvin Carl Teich. *Fundamentals of Photonics*. Wiley Series in Pure and Applied Optics. Wiley Interscience, Hoboken, N.J, 2nd ed edition, 2007.

[77] Seiji Katayama. *Fundamentals and Details of Laser Welding*. Topics in Mining, Metallurgy and Materials Engineering. Springer Singapore, Singapore, 2020.

[78] Charles L Caristan. Laser Cutting Guide for Manufacturing. *Society of Manufacturing Engineers*, 2004.

[79] Ping Jiang, Chaochao Wang, Qi Zhou, Xinyu Shao, Leshi Shu, and Xiongbin Li. Optimization of laser welding process parameters of stainless steel 316L using FEM, Kriging and NSGA-II. *Advances in Engineering Software*, 99:147–160, September 2016.

[80] Yousuke Kawahito, Naoyuki Matsumoto, Youhei Abe, and Seiji Katayama. Relationship of laser absorption to keyhole behavior in high power fiber laser welding of stainless steel and aluminum alloy. *Journal of Materials Processing Technology*, 211(10):1563–1568, October 2011.

[81] W.J. Suder and S. Williams. Power factor model for selection of welding parameters in CW laser welding. *Optics & Laser Technology*, 56:223–229, March 2014.

[82] Delphine Mathilde Cosme. Choisir la soudure par laser. *Techniques de l'ingenieur*, September 2013.

[83] Lance R. Hubbard, Christina L. Arendt, Daniel F. Dye, Christopher K. Clayton, Megan E. Lerchen, Nicholas J. Lombardo, Curt A. Lavender, and Alan H. Zacher. U-10Mo Baseline Fuel Fabrication Process Description. Technical Report PNNL–26880, 1400351, September 2017.

[84] Jaime Lisboa, Jorge Marin, Mario Barrera, and Héctor Pesenti. Engineering of Fuel Plates on Uranium-Molybdenum Monolithic: Critical Issues. *World Journal of Nuclear Science and Technology*, 05(04):274–286, 2015.

[85] G. A. Moore, J-F Jue, B. H. Rabin, and M. J. Nilles. Full Size U-10Mo Monolithic Fuel Foil and Fuel Plate Fabrication- Technology Development. *Research Reactor Fuel Management (RRFM)*, 2010.

[86] Pierre-Jean Cunat. *The Welding of Stainless Steels*. Number 3 in Materials and Applications Series. Euro Inox, Brussels, 2. ed edition, 2006.

[87] La soudabilité des aciers. *Techniques de l'ingenieur*, 2004.

[88] A. S. Elmesalamy, L. Li, J. A. Francis, and H. K. Sezer. Understanding the process parameter interactions in multiple-pass ultra-narrow-gap laser welding of thick-section stainless steels. *The International Journal of Advanced Manufacturing Technology*, 68(1-4):1–17, September 2013.

[89] M Ragavendran and M Vasudevan. Laser and hybrid laser welding of type 316L(N) austenitic stainless steel plates. *Materials and Manufacturing Processes*, 35(8):922–934, June 2020.

[90] Mingjun Zhang, Genyu Chen, Yu Zhou, and Shenghui Liao. Optimization of deep penetration laser welding of thick stainless steel with a 10kW fiber laser. *Materials & Design*, 53:568–576, January 2014.

[91] X.C. Sha, D.Z. Li, Y.T. Zhang, X.G. Zhang, and Y.Y. Li. Modelling effect of hot rolling process variables on microstructure and mechanical properties of low carbon strip steels. *Ironmaking & Steelmaking*, 31(2):169–175, April 2004.

[92] Jun Yan, Ming Gao, and Xiaoyan Zeng. Study on microstructure and mechanical properties of 304 stainless steel joints by TIG, laser and laser-TIG hybrid welding. *Optics and Lasers in Engineering*, 48(4):512–517, April 2010.

[93] ISO 17639:2022 - Essais destructifs des soudures sur matériaux métalliques - Examens macroscopique et microscopique des assemblages soudés, 2022.

[94] Antonio Riveiro, Félix Quintero, Mohamed Boutinguiza, Jesús Del Val, Rafael Comesana, Fernando Lusquinos, and Juan Pou. Laser Cutting: A Review on the Influence of Assist Gas. *Materials*, 12(1):157, January 2019.

[95] V Senthilkumar. Laser cutting process - A Review. *International Journal of Darshan Institute of Engineering Research and Emerging Technologies*, 2014.

[96] P. Di Pietro and Y.L. Yao. An investigation into characterizing and optimizing laser cutting quality - A review. *International Journal of Machine Tools and Manufacture*, 34(2):225–243, February 1994.

[97] B S Yilbas and B J Abdul Aleem. Dross formation during laser cutting process. *Journal of Physics D: Applied Physics*, 39(7):1451–1461, April 2006.

[98] Julia Bach, André T. Zeuner, Thomas Wanski, Sarah C. L. Fischer, Patrick Herwig, and Martina Zimmermann. Influence of the Dross Formation of the Laser-Cut Edge on the Fatigue Strength of AISI 304. *Metals*, 13(3):624, March 2023.

[99] Shangwen Chang, Taihong Yan, Weifang Zheng, Gaoliang Li, Shuliang Zou, Xinlin Wang, Xiangjiang Wang, Dewen Tang, and Weiwei Xiao. Microstructure and dissolution of UO2 pellet after cutting by fiber laser. *Optics & Laser Technology*, 132:106493, December 2020.

[100] C Journeau, J Monerris, B Tormos, L Brissonneau, E Excoffier, V Testud, C Chagnot, and D Roulet. Fabricating Fukushima Daiichi in-vessel and ex-vessel fuel debris simulants for the development and qualification of laser cutting technique. *ERMSAR-2017, Varsovie, Poland*, 2017.

[101] A. F. M. Arif and Bekir Samir Yilbas. Thermal stress developed during the laser cutting process: Consideration of different materials. *The International Journal of Advanced Manufacturing Technology*, 37(7-8):698–704, June 2008.

[102] Sangwoo Seon, Jae Sung Shin, Seong Yong Oh, Hyunmin Park, Chin-Man Chung, Taek-Soo Kim, Lim Lee, and Jonghwan Lee. Improvement of cutting performance for thick stainless steel plates by step-like cutting speed increase in high-power fiber laser cutting. *Optics & Laser Technology*, 103:311–317, July 2018.

[103] Rémi Torres. Influence of Laser Beam Polarization on Laser Micro-Machining of Molybdenum. *Journal of Laser Micro/Nanoengineering*, 8(3):188–191, December 2013.

[104] Maziar Sharifi and Mohammad Akbari. Experimental investigation of the effect of process parameters on cutting region temperature and cutting edge quality in laser cutting of AL6061T6 alloy. *Optik*, 184:457–463, May 2019.

[105] K. Abdel Ghany and M. Newishy. Cutting of 1.2mm thick austenitic stainless steel sheet using pulsed and CW Nd:YAG laser. *Journal of Materials Processing Technology*, 168(3):438–447, October 2005.

[106] C. Dazon, E. Porcheron, C. Journeau, C. Suteau, C. Chagnot, I. Doyen, E. Excoffier, and D. Roulet. Characterization of chemical composition and particle size distribution of aerosols released during laser cutting of fuel debris simulants. *Journal of Environmental Chemical Engineering*, 8(4):103872, August 2020.

[107] E. D. Cabanillas, M. F. Creus, and R. C. Mercader. Microscopic spheroidal particles obtained by laser cutting. *Journal of Materials Science*, 40(2):519–522, January 2005.

[108] Izhak Etsion. State of the Art in Laser Surface Texturing. *Journal of Tribology*, 127(1):248–253, January 2005.

[109] EPCM - ArcelorMittalSteel Hot Strip Mill Plant in Lázaro Cárdenas - IDOM. https://www.idom.com/en/project/epcm-planta-de-laminacion-en-caliente-en-lazaro-cardenas-mexico-2023.

[110] Sendzimir Mill Features — 20-Hi Cold Rolling Mill- Hani Tech. https://www.hanrm.com/sendzimir-mill-features/, 2023.

[111] Pierre Montmitonnet. Laminage - Objectifs et enjeux de la modélisation. *Techniques de l'ingenieur*, page 21, 2016.

[112] Zygmunt Wusatowski. *Fundamentals of rolling*. Pergamon Press, Oxford, New York, 1969.

[113] John G. Lenard. *Modelling Hot Deformation of Steels: An Approach to Understanding and Behaviour*. Springer International Publishing, Cham, 1989.

[114] J Rest, Y.S. Kim, G.L. Holmes, M.K. Meyer, and S.L. Heyes. U-Mo Fuels Handbook. Technical Report ANL-09/31, USA, June 2006.

[115] EA Nyberg, Vineet V. Joshi, Curt Lavender, and DE Burkes. Summary of Compression Testing of U-10Mo. Technical Report PNNL-21932, USA, October 2012.

[116] Primm R. T. Sease, J. D. and J. H. Miller. Considerations in the Development of a Process to Manufacture Low-enriched Uranium Foil Fuel for the High Flux Isotope Reactor. *RERTR*, 2007.

[117] D.W. Brown, D.J. Alexander, K.D. Clarke, B. Clausen, M.A. Okuniewski, and T.A. Sisneros. Elastic properties of rolled uranium–10wt.% molybdenum nuclear fuel foils. *Scripta Materialia*, 69(9):666–669, November 2013.

[118] Ayoub Soulami, Douglas E. Burkes, Vineet V. Joshi, Curt A. Lavender, and Dean Paxton. Finite-element model to predict roll-separation force and defects during rolling of U-10Mo alloys. *Journal of Nuclear Materials*, 494:182–191, October 2017.

[119] LR Hubbard and CL Arendt. U-10Mo Baseline Fuel Fabrication Process Description, Pacific Northwest National Laboratory. Technical report, September 2017.

[120] Guilherme Fernandes Nielsen, Nathanael Wagner Sales Morais, and Nelson Batista de Lima. Crystallographic texture of hot rolled uranium-molybdenum alloys. *Brazilian Journal of Radiation Sciences*, 8(3A), February 2021.

[121] Tércio A Pedrosa, José Giovanni M Brina, João Bosco de Paula, Fernando S Lameiras, and Wilmar B Ferraz. Preliminary results for the co-rolling process fabrication of plate-type nuclear fuel based in U-10Mo monolithic meat and Zircaloy-4 cladding. *International Nuclear Atlantic Conference 2013*, 2013.

[122] Chao Wang, Ayoub Soulami, Zhijie Xu, Guang Cheng, Shenyang Hu, Douglas Burkes, William E. Frazier, Kyoo Sil Choi, Xiaowo Wang, Xiaohua Hu, Curt A. Lavender, and Vineet V. Joshi. Process Modeling of U-10wt% Mo Alloys Using Integrated Computational Materials Engineering. Technical Report PNNL–28640, 1518489, March 2019.

[123] William Frazier, Chao Wang, Zhijie Xu, Nicole Overman, Shenyang Hu, and Vineet V. Joshi. Recrystallization and Grain Growth Simulations for Multiple-Pass Rolling and Annealing of U-10Mo. *Metallurgical and Materials Transactions A*, 51(2):533–544, February 2020.

[124] Saumyadeep Jana, Nicole Overman, Tamas Varga, Curt Lavender, and Vineet V. Joshi. Phase transformation kinetics in rolled U-10 wt. % Mo foil: Effect of post-rolling heat treatment and prior γ-UMo grain size. *Journal of Nuclear Materials*, 496:215–226, December 2017.

[125] ISO 6507-1:2018 - Matériaux métalliques - Essai de dureté Vickers - Partie 1: Méthode d'essai, 2018.

[126] André Dubois, Emilie Luc, Mirentxu Dubar, Laurent Dubar, Céline Thibaut, and Jean-Michel Damasse. Initiation of Sticking during Hot Rolling of Stainless Steel Plate. *Procedia Engineering*, 81:1958–1963, 2014.

[127] A.A. Popoff. Simplified hot rolling load calculations incorporating material strain rates. *International Journal of Mechanical Sciences*, 18(11-12):529–532, November 1976.

[128] R. B. Sims. The Calculation of Roll Force and Torque in Hot Rolling Mills. *Proceedings of the Institution of Mechanical Engineers*, 168(1):191–200, June 1954.

[129] Hiroshi Yada, Nobuhiko Matsuzu, Koe Nakajima, Kazuo Watanabe, and Hidenori Tokita. Strength and structural changes under high strain-rate hot deformation of C steels. *Transactions of the Iron and Steel Institute of Japan*, 23(2):100–109, 1983.

[130] A. l. Chen, G. K. Yang, and Z. M. Wu. Production scheduling optimization algorithm for the hot rolling processes. *International Journal of Production Research*, 46(7):1955–1973, April 2008.

[131] Xiangzhe Kong, Hongyan Yang, Shurong Ding, and Xiaoming Peng. Effects of Rolling Speed and Reduction on Rolling Simulation Results of Monolithic Fuel Plates. *International Journal of Nonlinear Sciences and Numerical Simulation*, 19(6):605–619, September 2018.

[132] A Nomine, D Bedere, and D. Miannay. Grandeur, mecaniques associées à la corrosion sous contrainte de I'alliage U-10Mo. *Coloque sur la rupture des materiaux*, 1972.

[133] Hakan Ozaltun, Pavel G. Medvedev, and Barry H. Rabin. Effects of the Foil Flatness on Irradiation Performance of U10Mo Monolithic Mini-Plates. *Journal of Nuclear Engineering and Radiation Science*, 1(4):041003, October 2015.

[134] Hakan Ozaltun and Barry H. Rabin. Effects of Fuel Thickness on Thermo-Mechanical Performance of U10Mo Monolithic Fuel Plates. In *Volume 6: Energy*, page V006T08A081, Tampa, Florida, USA, November 2017. American Society of Mechanical Engineers.

[135] Ke Huang. *Diffusion And Reaction In Selected Uranium Alloy System.* PhD thesis, 2012.

[136] N. L. Peterson and S. J. Rothman. Diffusion in Gamma Uranium. *Physical Review*, 136(3A):A842–A848, November 1964.